QUANTIFYING INTERACTIONS OF BIOMOLECULES WITH INORGANIC SURFACES

ABHIJEET PATRA

(B.Tech., NATIONAL INSTITUTE OF TECHNOLOGY, TIRUCHIRAPPALLI, INDIA)

A THESIS SUBMITTED

FOR THE DEGREE OF DOCTOR OF PHILOSOPHY

NUS GRADUATE SCHOOL FOR INTEGRATIVE SCIENCES AND ENGINEERING

NATIONAL UNIVERSITY OF SINGAPORE

2015

Declaration

I hereby declare that the thesis is my original work and it has been written by me in its entirety. I have duly acknowledged all the sources of information which have been used in the thesis.

This thesis has also not been submitted for any degree in any university previously.

Abhijeet Patra

11 November 2015

Acknowledgement

I do not believe in providence, fate or destiny. I believe that our present efforts have repercussions and step by step, they set out ripples which construct our future. Every one of our past actions shape our present through these repercussions, some severe, some gentle. However, when I think of how I came to know of Venky (Prof T Venkatesan, as he is formally known) and decided to join his group to pursue my doctoral research, I am stumped. I can't think of anything I have done in the past which could result in my walking into his office on 3rd November, 2011. That is probably what has been known as chance or luck. What has happened thereafter is, in retrospect, simply amazing, even borderline magical.

An airplane is very safe in a hangar. But that is not what an airplane is for. Under Venky's guidance, I learnt how to fly. Without Venky's zeal for pushing the boundaries for knowledge and constant lobbing of challenges at me, my graduate life would have been boring, perhaps even frustrating. Venky dislikes mediocrity and he has trained me to be extremely uncomfortable with it. Here was a highly accomplished world-beating scientist, 65 years of age, asking questions with a curiosity of a first year undergraduate student. In equal parts, Venky has amazed and taught, in the process lighting an indomitable fire within me. I feel very proud to say that he has imbibed in me the true spirit of scientific enquiry. A very large part of the success I get in my life hereafter will have its roots in this time which I have spent under Venky's supervision. I can't thank you enough, Venky. But, I sure will make you very proud.

My parents and my elder brother have always been scared of the choices I have made in life so far. In spite of their fear, they have always let me choose what I wanted to do and supported me in my decisions. I owe everything I am today, to your love and support *Ma, Baba* and *Dadabhai.*

There is another person who I need to specially thank. Her name is Ritika "Motu" Borkar. She kept me on track when the going got tough. She never let my self-belief slide always telling me that I was going to do great, repeating it until I started believing it again. She went to all lengths to ensure that I was happy, excited and comfortable in life. For being who you are and for caring as much as you do, I do not have words but ineffable feelings. Thank you, Motu.

I would like to thank Dr Federico Tesio Torta for being my mentor and teaching me the ropes of lipidomics research. He has been extremely patient with me and immensely helpful. Working with him has been an extremely rewarding experience. Dr Pradeep Narayanaswamy has been a friend and has helped me with his mass spectrometry expertise. Thanks to Aveline for helping me in the initial days of lipidomics research. I also have to thank Prof Markus Wenk for his inputs on the development of a solid phase extraction resin. Dr Wang Yi has helped me a lot with surface plasmon resonance and really accelerated my learning. I need to thank Prof Bo Liedberg for his crucial insights and sharing his vast experience in the field with me. I am grateful to Dr Tao Ding for his role in getting protein-nanoparticle interactions off the ground. I am also thankful to Prof James Kah, Prof Chester Lee Drum and my friend, Gokce. I also have to thank Kingshuk for his pointers in the initial days of my research. I am grateful to Prof CT Lim and Prof Ding Jun for their inputs on my research in their role as members of the thesis advisory committee.

Life in graduate school would not have been memorable without friends. I have made a lot of lasting friendships during my four years at NUS. These friends have not only made the last leg of student life exactly as crazy as it should be, but also been tremendous pillars of support and inspiration. I can't begin to thank all of them enough. First, I have to thank Michal Dykas for introducing me to Venky. Then I have to thank him again for being one of the best friends I have made in life, introducing me to Polish culture and the extremely complicated Polish language. "Papa" Lokesh Dhakar has been my other friend in need. He has played various roles – friend, financial savior, startup advisor. From discussing general frustrations to intoxicated ponderings of the meaning of human life, Papa has been omnipresent. I have to thank Prerna for just being her entertaining self, Alok for all the musical inspiration and Arunabh for all the movies, food and entrepreneurial companionship.

I have to thank Dr Siddhartha for his words of wisdom in times of need and his stimulating discussions on economics, culture and politics. I have learnt a lot about general conduct from Dr Surajit, apart from his in-depth knowledge on spectroscopic techniques. Thanks to Dr Malli for taking out lots of time to teach me the operation of the extremely complicated Rutherford Backscattering setup at Centre for Ion Beam Applications.

I would like to thank my friends at NUSNNI Nanocore – Dr Abhimanyu, Dr Meenakshi, Changjian, Tarapada and Soumya. There are two friends who I need to acknowledge separately for their contribution to this work. They joined our group in the last year of my candidature but have become close friends in a very short time. One of them is Sreetosh "Gurudeb" Goswami. He is a genius and a true epitome of devotion to one's pursuit. I have learnt a lot from him, least of

which is to have single minded dedication to unravelling the mysteries of experimental data. Almost every discussion with him is enlightening because of the sheer knowledge he can impart. The other is Saurav Prakash. Working with Saurav has been a complete joy. His understanding of material sciences is fantastic and the clarity with which he can explain concepts is admirable. We have banged our heads against the wall over seemingly nonsensical data together and then had eureka moments nonetheless.

This one is for all the crazy times, the ecstasy and the despair. Here's to the mysteries of science.

Table of Contents

Acknowledgement ..... **i**

Summary ..... **xi**

List of Tables ..... **xiii**

List of Figures ..... **xiv**

List of Abbreviations ..... **xix**

List of Publications ..... **xxi**

1 Introduction **1**

2 Methods **12**

2.1 Pulsed Laser Deposition 12

2.2 Atomic Force Microscopy 14

2.3 Scanning Electron Microscopy 15

2.4 Contact Angle and Surface Energy Measurement 17

2.4.1 Contact angle and surface energy 17

2.4.2 Description of OWRK method 19

2.5 Surface Plasmon Resonance 21

2.5.1 Surface plasmons 21

2.5.2 Excitation of surface plasmons 24

2.5.3 Optical sensing with surface plasmon resonance 27

2.5.4 Working principle of SPR biosensors 27

2.6 Rutherford Backscattering Spectroscopy 31

2.7 Mass Spectrometry 33

2.7.1 Matrix Assisted Laser Desorption Ionization 35

2.7.2 Electrospray Ionization 36

2.8 Liquid Chromatography 39

2.8.1 Thin Layer Chromatography 39

2.8.2 High Performance Liquid Chromatography 40

2.9 References 42

3 Quantifying interactions between water and surfaces 44

3.1 Abstract 44

3.2 Introduction 45

3.2.1 Overview 45

3.2.2 Literature review and the need for a new technique 45

3.2.3 Motivation and rationale 46

3.3 Results and discussion 47

3.3.1 Measurement of contact angles on surfaces and calculation of surface energies 47

3.3.2 Force spectroscopy on surfaces with native water layer 52

3.3.3 Correlating nanoscale measurements with macroscale measurements 56

3.3.4 Breaking of hydrogen bonds on the surface as a possible reason for nanoscale-macroscale hydrophilicity correlation 58

3.4 Conclusion 62

3.5 Experimental details 64

3.5.1 Sample fabrication 64

3.5.2 Contact angle measurement setup 65

3.5.3 Atomic force microscopy and force spectroscopy 66

3.6 References 67

4 Quantifying interactions between lipids and surfaces 69

4.1 Abstract 69

4.2 Introduction 70

4.2.1 Metabolomics 70

4.2.2 Lipidomics 73

4.2.3 The need for sample preparation 76

4.3 Results and discussion 84

4.3.1 Metal oxide coated MALDI plates for selective phospholipid enrichment 84

4.3.2 Phospholipid enrichment using µcolumns 87

4.3.3 Phospholipid enrichment using batch processing 92

4.3.4 Surface Plasmon Resonance for quantifying phospholipid adhesion 95

4.3.5 Planar columns on MALDI plates for on target enrichment....102

4.4 Conclusion....105

4.5 Experimental details....107

4.5.1 Fabrication of modified MALDI plates....107

4.5.2 Lipid adhesion studies with modified MALDI plates....107

4.5.3 Lipid adhesion studies with μcolumn approach....108

4.5.4 Lipid adhesion studies in batch processing approach....109

4.5.5 Surface plasmon resonance....110

4.5.6 On target enrichment....111

4.6 References....113

5 Quantifying interactions between serum proteins and gold nanoparticles....116

5.1 Abstract....116

5.2 Introduction....117

5.2.1 Overview....117

5.2.2 Existing methods used to study corona formation and their limitations....118

5.2.3 Need for a new method and previously reported work....119

5.3 Results and discussion....120

5.3.1 Immobilization of gold NPs....120

5.3.2 Studying interactions of AuNPs with proteins....123

5.3.3 Effect of PEGylation observed through SPR 128

5.3.4 Effect of varying PEG chain length on resistance to corona ... 130

5.3.5 Observation of hybrid modifications effect on NP targeting design 133

5.4 Conclusion 137

5.5 Experimental details 139

5.5.1 Synthesis of AuNPs 139

5.5.2 Immobilization of AuNPs onto the chip surface 139

5.5.3 Studying interactions of serum components with immobilized AuNPs 140

5.5.4 Obtaining kinetic parameters from curve fitting and calculating surface coverage 140

5.5.5 Studying interactions of serum components with PEGylated AuNPs 144

5.5.6 Studying effect of PEG chain length on corona formation 145

5.5.7 Studying the interaction of serum and streptavidin with model hybrid NP systems 145

5.6 References 147

6 Conclusion 150

Appendix 155

A-1 Density Functional Theory Calculations 155

A-2 MALDI scans on TiO_2 strip used for on-target enrichment 160

A-3 SPR sensorgrams for interactions of 3 serum proteins with gold nanoparticles.....164

A-4 SPR sensorgrams for interactions of PEG with chemically active chip surface 167

Summary

Making precise and meaningful measurements of interactions in biological sciences have traditionally proven to be challenging. The complex nature of experiments, innumerable interferences and the sheer manual efforts required have made it a formidable, but extremely interesting problem to solve. In this thesis, we have tried to develop techniques which enable measurements where previously, none existed and make measurements more accurate or convenient or both, where there were erroneous or cumbersome or both.

The ability to quantify the interactions between biomolecules and synthetic surfaces are crucial to our knowledge of several key biochemical scientific domains. We begin by taking a closer look at the simplest biomolecule, water. Interactions of water with surfaces have been studied mostly through the century-old method of water contact angle and the subsequent derivation of surface energy. However, in today's age of nanotechnology, this method has been dealt a severe limitation because of its macroscopic nature. Measuring local surface energies over areas no larger than hundreds of nanometres is very important today in the context of solid-liquid interfaces, nanofluidics, photovoltaics, biologics and several other allied domains. We demonstrate a new method based on force spectroscopy, to locally probe contact angle and surface energies, in the nanometre scale. The results we have obtained correlate very well to the macroscopically measured values.

Subsequently, we studied interactions of phospholipids with metal oxide surfaces with a close view on fabricating better solid phase extraction (SPE) resins to improve lipid fraction enrichment. Sample preparation in lipidomics

remains, till date, a major bottleneck, in the way of discovering underrepresented lipid species within the lipidomes of organisms. The overwhelming presence of phospholipids suppress the ionization and consequently the discovery of all rare lipids. We evaluate the performance of metal oxides as SPE resins to remove phospholipids from lipid extracts. We also demonstrate a very sensitive method of quantifying phospholipid adhesion to metal oxide surfaces using the phenomenon of surface plasmon resonance. Thereafter, we use the knowledge gained to fabricate enrichment devices in various formats.

Finally, we study interactions of plasma proteins with the surface of modified and unmodified nanoparticles. Non-specific adsorption of serum proteins onto the high energy surface of a nanoparticle which hits the physiological environment has been the biggest problem in the way of understanding and designing nano drug delivery systems. This adsorbed layer of proteins, also called “protein corona” completely alters the identity of the nanoparticle and radically changes its pharmacodynamics and pharmacokinetics. Existing methods to study and monitor the protein corona have been found to be either rudimentary or cumbersome. We demonstrate a surface plasmon resonance based high-throughput screening protocol to study the protein corona formation on nanoparticles. This method enables the user to derive kinetic constants of interaction which in turn help model the *in vivo* assembly of proteins on the nanoparticle surface. Ultimately, we show that the technique can be used to screen through nanoparticle based drug delivery formulations on few key parameters such as resistance to biofouling and ability to find intended target, within 3-4 hours thereby saving significant amounts of time and money.

List of Tables

Table 2.1 Surface tensions of the test liquids.....21

Table 3.1 Contact angles on various surfaces obtained with three different liquids and calculations of surface energies with its two components 51

Table 4.1 Lipid distribution in the plasma (*from Quehenberger, Oswald et al, Journal of lipid research 51.11 (2010): 3299-3305.*).....79

Table 4.2 Selection of a SPE resin amongst 3d oxides evaluating all of them on parameters discussed in the motivation section 4.2.3.4. (Costs taken from Sigma-Aldrich, Singapore website).....100

Table 4.3 Comparison of various methods of evaluating phospholipid adhesion to SPE resins 106

Table 5.1 Kinetic rate constants and equilibrium dissociation constants for four chosen serum proteins as calculated from fitting curves to the experimentally obtained SPR responses 125

Table 5.2 Estimated surface coverage of individual proteins in protein corona 127

Table 5.3 Comparison of methods used to study corona formation on nanoparticles 137

List of Figures

Figure 2.1 A schematic layout of a simple PLD setup.....12

Figure 2.2 Schematic of an AFM setup *(Courtesy: Bruker)*.....15

Figure 2.3 Schematic of a scanning electron microscope *(Courtesy: Encyclopaedia Britannica)* 17

Figure 2.4 Schematic diagram of a liquid drop on a solid surface showing the interfacial tensions at three phase boundary. 18

Figure 2.5 Surface energy (polar and dispersive) calculation graph based on OWRK model for lubricated hard disk media 21

Figure 2.6 The dispersion relation of free photons in a dielectric (a), and in a coupling prism (b) with $\varepsilon_p > \varepsilon_d$, compared to the dispersion relation of non-radiative surface plasmons (c) at the metal/dielectric interface.....24

Figure 2.7 A schematic of how SPs are excited in the Kretschmann configuration 26

Figure 2.8 Angular spectrum of reflectivity showing a dip at 56°.....27

Figure 2.9 Simulation of angular spectrum of reflectivity of Sc2O3 (5 nm) film on a gold (50 nm) film in water. Resonance occurs at 59.9° 29

Figure 2.10 Working principle of SPR biosensor in angular mode of operation, used in chapter 4 to find amount of phospholipid bound to thin film of metal oxide.....31

Figure 2.11 Rutherford backscattering spectroscopy layout.....33

Figure 2.12 Simplified layout of a mass spectroscopy setup *(Courtesy: Francis Carey, McGraw Hill Higher Education)* 34

Figure 2.13 Schematic of a MALDI setup *(Courtesy: NPTEL, India)* 36

Figure 2.14 Schematic of a electrospray ionisation setup *(Courtesy: Lamond Lab)* 38

Figure 2.15 Schematic of a thin layer chromatography setup *(Courtesy: Waters)* 40

Figure 3.1 Water contact angle measurement (a) schematic of measurement (b-i) different surfaces having contact angle ranging from 0° to ~ 102° 48

Figure 3.2 Atomic force microscopy topographic images of different surfaces 50

Figure 3.3 Force spectroscopy (FS) measurements in ambient conditions, **(a)** schematic of measurement **(b-i)**. FS curve on different surfaces having contact angle ranging from 0° to ~ 102°, [**b** –mica, **c** – VO_2(B) grown on STO, **d** – VO_2(M) grown on STO, **e** – cover slip glass, **f** – hard disk media, **g** – STO substrate, **h** – Lu_2O_3 grown on YSZ, **i** – lubricated hard disk media.]**Inset:** the curves plotted at a scale to clearly show the behaviour near detachment point. Distances before detachment from the surface (d_1) and the distance travelled by the probe in contact with the liquid meniscus (d_2) are shown in (b). 54

Figure 3.4 Illustration depicting the various phases of tip interaction with the surface in the case of retraction (going away) from the sample. **(A)** Tip leaves the solid surface, **(B)** tip travels through the film of adsorbed water, **(C)** tip extends the neck of the meniscus formed by the water, **(D)** ultimately, the tip breaks free from the film of water 55

Figure 3.5 The maximum pulling force plotted versus different parameters obtained from macroscale contact angle measurements, the maximum pull-off force versus (a) water contact angle (b) total surface energy (c) polar component of surface energy (d) dispersive component of surface energy[1 –mica, 2 – VO_2(B) grown on STO, 3 – VO_2(M) grown on STO, 4 – cover slip glass, 5 – hard disk media, 6 – STO substrate, 7 – Lu_2O_3 grown on YSZ, 8 – lubricated hard disk media.] 58

Figure 3.6 (a) and **(b)** are the distances travelled up to a point before and after the maximum negative deflection is achieved respectively. ..... **(c-d)** schematic showing hydrogen molecule structure at the interface of highly hydrophilic surface and relatively less hydrophilic surface respectively 60

Figure 4.1 A medieval urine chart detailing conditions that can be diagnosed from change in apparent properties of urine. *(Courtesy: Scientific American)* 71

Figure 4.2 A schematic illustration of the concept of SPE applied to lipidomics 82

Figure 4.3 Schematic workflow of the experiment for testing metal oxide thin films as SPE resins in the MALDI format 85

Figure 4.4 Comparison between 6 chosen transition metal oxides with respect to their selectivity of enrichment of phospholipids DMPC and SM. Ideally, after a wash of MeCN and 0.1% TFA, the nonphospholipid fractions GluCer, Cer 534, Cer 574 should get removed from the plate leaving only DMPC and SM. 86

Figure 4.5 SEM images of powders showing the large difference in particle sizes. Scale bars are shown in green. 89

Figure 4.6 Comparison between 4 oxides with respect to selective phospholipid enrichment. (Brown denotes flowthrough component, which should ideally have only GluCer and Cer 17; green denotes the elution component which should have only DMPC and SM. Y Axis is in arbitrary signal strength units. 90

Figure 4.7 Evaluation of α used to compare between various metal oxides. x_0 is the number of molecules in the original mixture. αx_0 denotes the number of molecules captured by the column. $(1-\alpha)x_0$ molecules are not able to find capture sites on the SPE resin and are present in the flowthrough. D is obtained by dividing peak intensities of flowthrough and elution as obtained through ESI-MS. α will be 1 for a perfect SPE and 0 for a material which has no affinity for phospholipids. 93

Figure 4.8 α as obtained for all stable 3d transition metal oxides 94

Figure 4.9 The capture and release of the phospholipid DMPC from a 3 nm film of TiO2 observed through surface plasmon resonance. Various events have been marked on the plot 97

Figure 4.10 Angular spectrum showing shifts in resonant dips upon binding and unbinding DMPC. The actual and fitted data is shown. The estimation of mass on the TiO2 surface is derived and displayed in the inset. n is refractive index. Details of calculation can be found in section 4.5.5. 98

Figure 4.11 Angular spectrum showing the etching of CuO film when it comes in contact with the 0.1% TFA (acidic buffer) used to inject the phospholipid DMPC into the setup. 99

Figure 4.12 Differences in adhesion based on number of phosphate groups. Phosphate groups have been marked with black arrow. 102

Figure 4.13 Schematic illustration of the design of the experiment showing how the data is acquired. Green colour denotes stainless steel. Orange denoted the deposited film of TiO_2. 103

Figure 4.14 MALDI-MS data at a point 3 cm away from the spotting point. Only phospholipids LPC, SM and PC were found. Non-phospholipids were not found on the strip. 105

Figure 4.15 Schematic of fabrication of the planar TiO2 columns for on target enrichment 112

Figure 5.1 (A) SPR sensorgram of surface modification using a hetero-bifunctional linker and subsequently, the immobilization of AuNPs. (B) SEM image of the sensor surface after AuNP injection 121

Figure 5.2 (A) SEM image of the chip surface after immobilization of AuNP. (B) The same image, processed with ImageJ to enable counting of AuNPs. (C) Distribution of particles on the surface. It can be seen that there is almost no agglomeration and the AuNPs are well dispersed..... 123

Figure 5.3 The microfluidic channel setup allowing multiplexed data collection is shown. AuNPs are immobilized in 3 channels G1, G2 and G3 using EDC/S-NHS coupling as described. Two control channels (G4 and G5) are employed. G4 channel is modified with all the linker chemistry used to capture AuNPs (but AuNPs are not injected). G5 channel is in as received condition (alginate layer with inactive –COOH groups). Fibrinogen in three concentrations (3.750 μM, 1.775 μM and 0.938 μM) is injected along channels P1, P2 and P3 respectively. The three colored lines (blue, green, yellow) in each panel correspond to 3 different concentrations of fibrinogen used in the experiment (legend in white box in each panel) (A), (B) and (C) Sensorgrams showing the interaction of fibrinogen with bare AuNPs available in channels G1, G2 and G3. (D) Sensorgram resulting from the interaction of fibrinogen with the chemically active lane without the AuNPs. (E) Sensorgram showing the interaction of fibrinogen with the unmodified surface (alginate polymer layer). 124

Figure 5.4 Normalized SPR response for interaction of individual serum proteins [(A) HSA, (B) Fibrinogen, (C) IgG, (D) ApoA1] with AuNPs modified with PEG2K compared to unmodified AuNPs. The absolute response obtained due to adsorption of proteins to modified and unmodified AuNPs is divided by the absolute response caused by the immobilization of AuNPs on the sensor surface. This normalization, hence,

takes care of the minor differences in number of AuNPs captured in each lane. 130

Figure 5.5 Normalized SPR response for interaction of 20% (W/V) human serum (diluted with PBS buffer) with AuNPs modified with PEG2K, PEG5K, PEG10K, PEG20K and PEG30K compared to unmodified AuNPs. With the exception of PEG 2K and PEG 5K, all sets of data were statistically different from all other sets.(p-value <<0.05) 132

Figure 5.6 (A) Normalized SPR response for interaction of 20% human serum with AuNPs modified with PEG5K-biotin (referred to as "Biotin"), PEG2K and 1:1 mixture of Biotin:PEG2K (referred to as "Hybrid") compared to unmodified AuNPs. The inset illustrates the schematic of the experiment (B) Normalized SPR response showing the ability of AuNPs with previously described functionalizations to bind intended target streptavidin. The inset illustrates the schematic of the experiment. (p-value <<0.05) 136

Figure 5.7 Example of curve fitting on Origin software package on experimentally collected data to obtain kinetic parameters 142

List of Abbreviations

PLD	Pulsed Laser Deposition
AFM	Atomic Force Microscopy
SEM	Scanning Electron Microscope
RBS	Rutherford Backscattering Spectroscopy
WCA	Water Contact Angle
OWRK	Owens Wendt Rabel and Kaelbel
SPR	Surface Plasmon Resonance
MS	Mass Spectrometry
MALDI	Matrix Assisted Laser Desorption Ionization
ESI	Electrospray Ionization
LC	Liquid Chromatography
HPLC	High Performance Liquid Chromatography
RP-HPLC	Reverse Phase High Performance Liquid Chromatography
TLC	Thin Layer Chromatography
DFT	Density Functional Theory
RMS	Root Mean Square
STO	$SrTiO_3$
FS	Force Spectroscopy
SPE	Solid Phase Extraction
DMPC	1,2-dimyristoyl-sn-glycero-3-phosphocholine
SM	N-lauroyl-D-erythro-sphingosylphosphorylcholine
GluCer	D-glucosyl-ß-1,1'-N-octanoyl-D-erythro-sphingosine
Cer	Ceramide
LAO	$LaAlO_3$
TFA	Trifluoroacetic Acid
TEA	Triethylamine
PI	Phosphatidylinositol diC16
PIP	Phosphatidylinositol 3-phosphate diC16
PIP_2	Phosphatidylinositol 3,4-bisphosphate diC16
PIP_3	Phosphatidylinositol 3,4,5-trisphosphate diC16
RU	Response Units

AuNP	Gold Nanoparticle
k_{on}	On-Rate
k_{off}	Off-Rate
K_D	Dissociation constant
K_A	Association Constant
NHS	N-hydroxysulfosuccinimide
EDAC	1-ethyl-3-(3-dimethylaminopropyl) carbodiimide
HSA	Human Serum Albumin
ApoA1	ApolipoproteinA1
IgG	Immunoglobulin G
PEG	Polyethylene Glycol

List of Publications

1. Component specific analysis of plasma protein corona formation on gold nanoparticles using multiplexed surface plasmon resonance. *Abhijeet Patra[#], Tao Ding[#], Gokce Engudar, Yi Wang, Michal Marcin Dykas, Bo Liedberg, James Chen Yong Kah*, T Venkatesan*, Chester Lee Drum* (**Accepted, Small)***
2. Unexpected observation of spatially separated Kondo scattering and ferromagnetism in Ta alloyed anatase TiO_2 thin films
   *Tarapada Sarkar, Kalon Gopinadhan, Mallikarjuna Rao. Motapothula, Surajit Saha, Z. Huang, S. Dhar, Abhijeet Patra, Weiming Lu, Francesca Telesio, Ilaria Pallecchi, Ariando Ariando, Daniele Marré, and T. Venkatesan **(Accepted, Scientific Reports)***
3. Probing the nanoscale behavior of forces for macroscale surface wettability.
   *Abhimanyu Rana[#], Abhijeet Patra[#], Meenakshi Annamalai[#], Amar Srivastava, Siddhartha Ghosh, Kelsey Stoerzinger, Yueh-Lin Lee, Partho Pattader, Nalam Satyanarayana, Kalon Gopinadhan, Michal M. Dykas, Kingshuk Poddar, Surajit Saha, Tarapada Sarkar, Brijesh Kumar, Charanjit S. Bhatia, Livia Giordano, Yang Shao-Horn, T Venkatesan **(Submitted)***
4. Metal oxides as solid phase extraction resins: A comparative study.
   Abhijeet Patra, Federico Tesio Torta, Wang Yi, Michal Marcin Dykas, Kingshuk Poddar, Bo Liedberg, Markus Wenk, T Venkatesan (***Under preparation)***
5. Effect of headgroup on phospholipid adhesion to iron oxide: an application to phosphoinositol extraction
   Abhijeet Patra, Federico Tesio Torta, Wang Yi, Michal Marcin Dykas, Kingshuk Poddar, Bo Liedberg, Markus Wenk, T Venkatesan (***Under preparation)***
6. Wettability of oxide thin films: new insights
   *Abhijeet Patra[#], Saurav Prakash[#], Siddhartha Ghosh, Meenakshi Annamalai, Soumya Sarkar, T Venkatesan **(Under preparation)***
7. Elemental library for biological screening
   *Michal Marcin Dykas, Stuti Desai, Abhijeet Patra, Mallikarjuna Rao, Linda Kenny, T Venkatesan **(Under preparation)***
8. Engineering the surface energy of graphene
   *Abhijeet Patra[#], Sinu Matthew[#], Surajit Saha, Saurav Prakash, Soumya Sarkar, T Venkatesan **(Under preparation)***
9. Synthesis of new functional materials using the idea of super hydrogenic dopants in oxides - a new approach

Siddhartha Ghosh, Zhiqi Liu, Surajit Saha, Abhijeet Patra, Mallikarjuna Rao, Nikolai Yakovlev, A Ariando, T Venkatesan ***(Under preparation)***

10. The effect of oxygen vacancies on water wettability of 3d and 4f element based metal oxides
    Tarapada Sarkar[#], Meenakshi Annamalai[#], Siddhartha Ghosh, Abhijeet Patra, Kelsey Stoerzinger, Yueh-Lin Lee, Saurav Prakash, Mallikarjuna Rao Motapothula, Yang Shao-Horn, Livia Giordano, T. Venkatesan. ***(Under preparation)***

1 Introduction

"When you can measure what you are speaking about,

and express it in numbers, you know something about it"

- Lord Kelvin, Electrical Units of Measurement, Vol 1, 1883-05-03

Long before the 19th century, the importance of quantification to progress in science was obvious even to ancient Greek philosophers. A contemporary of Socrates, Philolaus of Croton (in today's southern Italy) remarked "actually, everything that can be known has a number; for it is impossible to grasp anything with the mind or to recognize it without this." Time after time, leading scientific minds across eras have expressed their views on the role measurement plays in pushing the boundaries of human knowledge. To quote Lord Kelvin once again, "if you cannot measure it, you cannot improve it."

We believe, the science and technology that facilitates and enables measurement of parameters are the cornerstones of scientific advancements. However, when proper quantification has been hard to accomplish, science has taken a detour through qualitative, empirical and quasi-quantitative approaches. More often than not, the field of biology and allied fields with a biological context have had to deal with this problem. Unlike domains in engineering and solid-state physics, measurements in biology have been traditionally very difficult. The sheer complexity of biological systems have made data collection and consequent analysis a challenge. The difficulty notwithstanding, forward-

thinking minds have made shocking advancements over the course of last few decades in making the field of biology more navigable with numbers to put on observations.

The motivation behind this thesis work is, as the title suggests, enable the quantification of interaction of biomolecules with inorganic surfaces. Biology, today, has spawned a whole array of fields of scientific research which draw on a host of other major sciences to ultimately advance and benefit the human race. They are all highly specialized domains linked by one common thread, understanding the state of human health better and seeking to restore it in times of disease through specifically engineered interventions. In all of these fields, as in general science, knowing one's numbers is of paramount importance. Through this work, we demonstrate techniques which enable accurate measurements of parameters of interest to scientists involved in the study of lipids and proteins. In some cases we have been able to measure quantities never measured before. In others, we have made measurements much more accurate and meaningful than reports in prior literature.

This thesis has been divided into 6 major chapters. The first chapter is an introduction to the thesis which describes the motivation behind taking up this work. We also discuss briefly the contents of the next chapters.

In chapter 2, we will discuss the methods used to accomplish this study. The description and discussion is brief where the original established method has been used without any significant modification. A detailed and more in depth discussion is provided where the prevalent and commonly used method has been significantly tweaked to serve the purpose needed. We would like to draw

special attention to the fabrication of the surface plasmon resonance chips as there are a number of issues which were taken care of and addressed in due course of this endeavor (please refer **section 2.5.4**). We would also like to point out the modification made to the typical matrix assisted laser desorption ionization method as is prevalent in the field of proteomics and lipidomics with a detailed description of the process in **section 4.5.6**.

For the sake of organization the experimental work has been split into three major chapters. The class of biomolecules studied will increase in their weight from chapter 3 to 4 through 5. In seeking to quantify the interactions of biomolecules with inorganic surfaces, we begin with, in chapter 3, the simplest and most common biomolecule, indispensable to the maintenance of life as we understand it, water. Thereafter, in chapter 4, we will move to a heavier class of biomolecules, namely lipids which weigh in hundreds of Daltons. Chapter 5 will deal with interactions of proteins, which weigh in tens of thousands of Daltons. Since the functions and implications of each study are quite diverse and also not completely convergent, we decided against an overall literature review. Instead we have provided a detailed literature review of each section of study in the respective chapter. However, for the purposes of introducing the motivation behind taking up this work, we will describe the problems we have worked on and their importance to science in this chapter. We hope this makes it easier to explain the gaps in knowledge which we are trying to address through this piece of work.

The interactions of water with surfaces has been studied over hundreds of years and lots of advancements have been made in the field of surface and interfacial science. Wetting angle[1] as measured through the sessile drop method has been

around for about a century. A slightly more complex measurement which enables inspection of hydrophilicity of a surface is inverse gas chromatography[2]. During the 1950s, scientists figured out how to use wetting angles to evaluate surface energies. These methods have been the only options for researchers looking to understand the interaction of water with the surfaces of interest. Of late, there has also been an explosion of interest in surfaces which would be intrinsically hydrophobic[3] for their applications in heat exchangers and high rise windows. The need to understand interaction of water with surfaces goes much further into fields of nanofluidics, photo-catalysis, solar energy conversion, self-assembled monolayers and many more. This brings us to the problem which existing methods mentioned above cannot solve. Almost all functional surfaces of today are nano-patterned (domains of different materials arranged on a surface). Contact angle measurement is a macroscopic measurement with droplet size usually in the range of μl. If we employ it in evaluating local wettability and consequently surface energies, the data obtained has inherent errors from chemical heterogeneity built into it. Engineers have tried to solve the issue by reducing the size of the droplet to nano and picolitres. However, making droplets that small introduces new problems - non-uniformity of sizes across successive droplets, quick evaporation from the surface, expensive equipment to dispense and manage such small droplets. Concurrently, groups around the world have tried to address the issue of wettability in the nanoscale by using simulation tools [4, 5]. However, upon extensive literature review (provided in detail in section 3.2.1 and 3.2.2) we found that understanding of nanoscale phenomenon as gained through simulations hasn't been used to further understanding of macroscale

interactions of water with surfaces, which is represented in contact angle. In chapter 3, we demonstrate the ability to measure local surface energies with no more than an atomic force microscopy (AFM) setup. We analyse the traditional force-distance curves and find a direct relation between the force required to break free from the native water layer on any solid surface and its hydrophilicity. In essence, we show a new technique of quantifying interaction of water with unreactive inorganic surfaces. The technique we employ is simple and can be carried out within the most basic AFM setups. In order to really relate experimental data that we acquire to the accepted principles of the domain, we have also shown that there is a direct correlation between the propensity of a given surface to get hydroxylated (simulated through density functional theory calculations) with its tendency to be more hydrophilic (actual data collected through force-distance curves)

Chapter 4 deals with the interaction of phospholipids and transition metal oxides. Sample preparation has been a troublesome bottleneck in the field of lipidomics[6]. The mass representation of lipids species in the human lipidome is extremely skewed[7]. Mass spectrometry is the only analytical tool that researchers have to quantify these lipid species. Under this constraint, the overbearing abundance of phospholipids in the lipidome suppresses the ionization and subsequently discovery of underrepresented non-phospholipid species. An ideal solution would be the complete separation of phospholipids from non-phospholipids in the post-collection, sample preparation step. The goal is to analyze samples in a manner where one can gather signals from ionization, ideally from all species present. This task however is herculean. Due to the chemical diversity of the lipidome, there can’t be one perfect strategy of

preparing samples. There needs to be synergy between subsequent steps of sample preparation so that the final analysis discovers all species, without any bias being induced by any of the sample preparation steps. The latter part has proven especially difficult. More often than not, sample preparation strategies have not been completely understood and this has introduced the terrifying possibility of wrong conclusions being drawn from a compromised experiment [8-10]. Traditionally, sample preparation in lipidomics has revolved around liquid-liquid extraction, wherein the differential solubilities of a chemical species in an aqueous and organic phase is used to separate the species from the rest. However, applying this to phospholipid extraction from a lipidome is futile because almost all phospholipids prefer to stay in the organic apolar phase rather than in water. Emulsions are a real problem with liquid-liquid extraction as well. It is clear that the way forward through this bottleneck is definitely not through liquid-liquid extraction. Thereby, our aim comes to be defined as designing what is known in the field of chromatography as solid phase extraction resins. Solid phase extraction resins are materials, obviously in solid phase (powders or surfaces), which have selective affinity towards a class of chemical species (in this case phospholipids). Upon passing a complex lipidome through these resins, we should be able to selectively capture phospholipids on the resin, thereby leaving the flowthrough rich in non-phospholipid species. We wanted to develop accurate comparative studies between transition oxides with respect to their promise in being successfully employed as resins to perform selective phospholipid capture. There are reports in literature of various oxides[11, 12] being tried but measurements to compare between them hasn't been controlled to be able to draw the correct conclusions. When dealing with columns packed

with powders of the intended resin, there are a few key parameters that one needs to keep in mind for gauging the performance of the column. Unless the particles of two resins being compared have the same size, the actual surface area in contact and the time spent by the separating species in contact will be different. Under, these circumstances, any choice made on the basis of such uncontrolled experiments, could prove to be dubious. Additionally, the resin material may corrode under the separation conditions being used, which might cause downstream effects in the workflow, especially when mass spectrometry systems are so sensitive to salts. We demonstrate a technique to precisely measure the amount of phospholipids captured per unit area of a thin film of transition metal oxide using surface plasmon resonance. The importance of being able to measure adhesion to atomically flat thin films is that in such a situation it is only chemistry of the surface that is influencing the binding. Such precise measurement would enable us to choose the best solid phase extraction resins for specific applications and optimize cost/performance. We also demonstrate a novel architecture of a separation device based on planar oxide columns for separating lipid species which is completely compatible with mass spectrometry systems being used currently.

In chapter 5, we seek to quantify interactions between plasma proteins and gold nanoparticles. Lot of scientific effort has been directed towards understanding and quantifying the "protein corona" [13-15] which forms around nanoparticles when they enter the physiological environment. The non-specific adsorption of serum proteins onto nanoparticles has been blamed for a lot of engineered nano drug delivery systems failing to accomplish their task[16]. The accepted wisdom in the field is that the "corona" causes complete fouling of the surface

thereby effectively covering all surface functionalization moieties which are intended to give it the ability to find and attach to specific cells, before releasing its cargo. The corona covered nanoparticle hence goes around the bloodstream or gets internalized by cells it is not intended for. Desirable clinical outcomes are completely diminished if not eliminated completely [17-20]. It is now known that silica nanoparticles[21], gold nanoparticles[22-25], carbon nanotubes[26, 27] all have different compositions of the corona that form on them. In a situation where engineered nanomaterials are being intensely investigated for their potential applications in healthcare, the study of protein corona formation is a very important yet very difficult problem. Upon review of literature (more details can be found in **section 5.2.2** and **5.2.3**), it is revealed that there are two broad kinds of techniques being employed today. One group contains methods such as dynamic light scattering, differential centrifugal sedimentation, size exclusion chromatography, etc which provide only the apparent change in radius when a nanoparticle binds to a protein creating a complex. In all these techniques, the data acquired varies greatly across runs and the information provided is just the apparent change in radius upon a binding event between the protein and the nanoparticle. If the unbound components are about the same size as the bound complexes, these techniques will fail to provide meaningful information. On the other hand lies the most comprehensive method which provides all information regarding the identification of bound proteins to nanoparticles. However, the throughput is low and a large number of steps are involved which take about 8-10 days[28] to complete the measurement. The large number of manual steps also introduce the possibility of user bias. In addition, importantly, no method being used

currently provides real time kinetics of the interaction between serum proteins and nanomaterials. We have addressed all these issues and designed a method which makes use of multiplexed surface plasmon resonance technique which provides kinetic information about protein adsorption onto nanoparticles in a matter of 3 hours. Since our technique is modular, it can be used for any nanoparticle formulation of any shape, size within 100 nm. It can efficiently evaluate the efficacy of anti-fouling measures employed by formulation scientists to prevent corona formation. We also demonstrate how we can use this approach to screen nanoparticle based drug delivery systems in an ex-vivo setup without having to do cell studies every time.

Once again, we wish to reiterate that a detailed survey of the related research landscape can be found at the beginning of each chapter which contains the actual experiments (chapter 3, 4 and 5).

Chapter 6 contains concluding remarks and an overview of the future work which can follow the results which we have been able to showcase in this thesis.

References

1. Mittal, K.L., *Advances in contact angle, wettability and adhesion*. 2013: John Wiley & Sons.
2. Das, S.C., et al., *Determination of the Polar and Total Surface Energy Distributions of Particulates by Inverse Gas Chromatography.* Langmuir, 2011. **27**(2): p. 521-523.
3. Azimi, G., et al., *Hydrophobicity of rare-earth oxide ceramics.* Nat Mater, 2013. **12**(4): p. 315-320.
4. Giovambattista, N., P.G. Debenedetti, and P.J. Rossky, *Effect of Surface Polarity on Water Contact Angle and Interfacial Hydration Structure.* The Journal of Physical Chemistry B, 2007. **111**(32): p. 9581-9587.
5. Giovambattista, N., P.G. Debenedetti, and P.J. Rossky, *Enhanced surface hydrophobicity by coupling of surface polarity and topography.* Proceedings of the National Academy of Sciences, 2009. **106**(36): p. 15181-15185.
6. Hu, C., et al., *Analytical strategies in lipidomics and applications in disease biomarker discovery.* Journal of Chromatography B, 2009. **877**(26): p. 2836-2846.
7. Quehenberger, O., et al., *Lipidomics reveals a remarkable diversity of lipids in human plasma.* Journal of lipid research, 2010. **51**(11): p. 3299-3305.
8. Bruce, S.J., et al., *Investigation of human blood plasma sample preparation for performing metabolomics using ultrahigh performance liquid chromatography/mass spectrometry.* Analytical Chemistry, 2009. **81**(9): p. 3285-3296.
9. Moco, S., et al., *Metabolomics technologies and metabolite identification.* TrAC Trends in Analytical Chemistry, 2007. **26**(9): p. 855-866.
10. Teahan, O., et al., *Impact of analytical bias in metabonomic studies of human blood serum and plasma.* Analytical chemistry, 2006. **78**(13): p. 4307-4318.
11. Gerdes, J.C., et al., *Kit comprising solid phase matrix made of aluminum oxide, titanium oxide (Ti2O3) and/or modified zirconium dioxide (ZrO2) for identifying and extracting viral nucleotide sequences*. 2006, Google Patents.
12. Wei, W., et al., *Elimination of the interference from nitrate ions on oxalic acid in RP-HPLC by solid-phase extraction with nanosized hydroxyapatite.* Journal of Liquid Chromatography & Related Technologies, 2008. **32**(1): p. 106-124.
13. Monopoli, M.P., et al., *Physical−Chemical Aspects of Protein Corona: Relevance to in Vitro and in Vivo Biological Impacts of Nanoparticles.* Journal of the American Chemical Society, 2011. **133**(8): p. 2525-2534.
14. Walczyk, D., et al., *What the Cell "Sees" in Bionanoscience.* Journal of the American Chemical Society, 2010. **132**(16): p. 5761-5768.
15. Lynch, I. and K.A. Dawson, *Protein-nanoparticle interactions.* Nano Today, 2008. **3**: p. 40-47.

16. Salvati, A., *Transferrin-functionalized nanoparticles lose their targeting capabilities when a biomolecule corona absorbs on the surface.* Nature Nanotech.
17. Bajaj, A., et al., *Stability, toxicity and differential cellular uptake of protein passivated-Fe3O4 nanoparticles.* J. Mater. Chem., 2009. **19**: p. 6328-6331.
18. Boraschi, D., L. Costantino, and P. Italiani, *Interaction of nanoparticles with immunocompetent cells: nanosafety considerations.* Nanomedicine, 2011. **7**: p. 121-131.
19. Brown, D.M., et al., *Interaction between nanoparticles and cytokine proteins: impact on protein and particle functionality.* Nanotechnology, 2010. **21**: p. 215104.
20. Fadeel, B. and A.E. Garcia-Bennett, *Better safe than sorry: understanding the toxicological properties of inorganic nanoparticles manufactured for biomedical applications.* Adv. Drug Deliv. Rev., 2010. **62**: p. 362-374.
21. Ang, J.C., et al., *Protein trapping of silica nanoparticles.* Soft Matter, 2010. **6**: p. 383-390.
22. Brewer, S.H., et al., *Probing BSA binding to citrate-coated gold nanoparticles and surfaces.* Langmuir, 2005. **21**: p. 9303-9307.
23. Dobrovolskaia, M.A., *Interaction of colloidal gold nanoparticles with human blood: effects on particle size and analysis of plasma protein binding profiles.* Nanomed. Nanotech. Biol. Med., 2009. **5**: p. 106-117.
24. Gagner, J.E., et al., *Effect of gold nanoparticle morphology on adsorbed protein structure and function.* Biomaterials, 2011. **32**: p. 7241-7252.
25. Schleh, C., *Size and surface charge of gold nanoparticles determine absorption across intestinal barriers and accumulation in secondary target organs after oral administration.* Nanotoxicology, 2012. **6**: p. 36-46.
26. Gasser, M., *The adsorption of biomolecules to multi-walled carbon nanotubes is influenced by both pulmonary surfactant lipids and surface chemistry.* J. Nanobiotechnol., 2010. **8**: p. 31.
27. Ge, C., *Binding of blood proteins to carbon nanotubes reduces cytotoxicity.* Proc. Natl Acad. Sci. USA, 2011. **108**: p. 16968-16973.
28. Docter, D., et al., *Quantitative profiling of the protein coronas that form around nanoparticles.* Nat. Protocols, 2014. **9**(9): p. 2030-2044.

2 Methods

2.1 Pulsed Laser Deposition

Pulsed laser deposition (PLD) is a highly controlled process to fabricate thin films with precise control over thickness and composition.[1] In a typical PLD setup, elementary or alloy targets are struck at an angle of 45° by a pulsed and highly focused laser beam. The atoms and ionic species ablated from the target(s) are deposited on a substrate placed parallel to the target surface at a target-to-substrate distance of typically 2–10 cm. A schematic of a simplified setup is shown in **figure 2.1.**

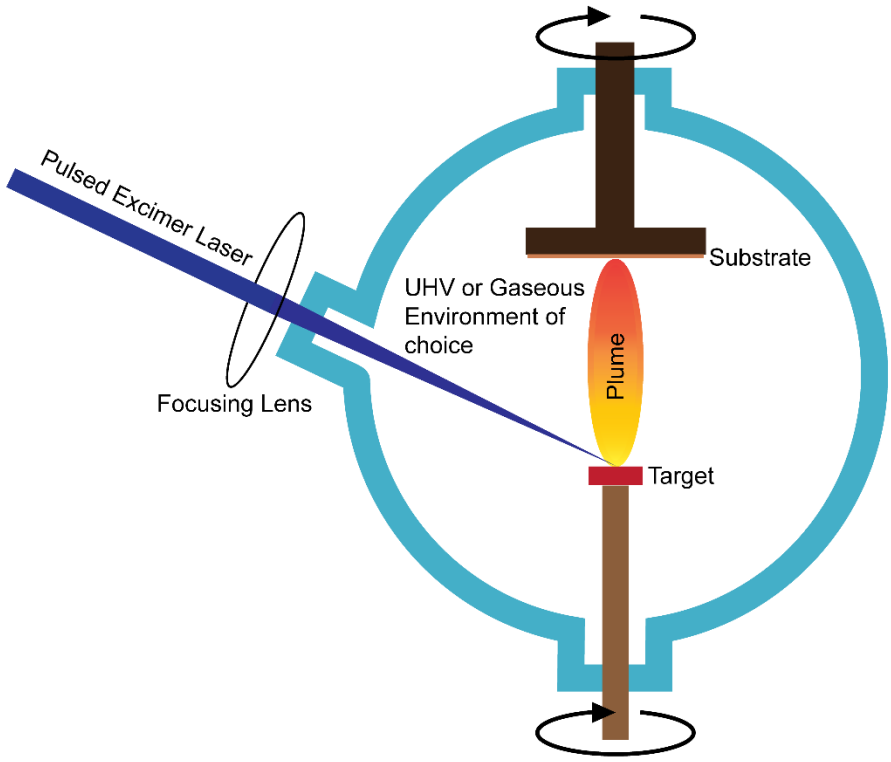

Figure 2.1 A schematic layout of a simple PLD setup

Since the energy source (laser) is outside the chamber, it is possible to maintain the chamber at ultra-high vacuum ($<10^{-6}$ Torr) or backfill it with a gas of choice (oxygen, nitrogen, argon). This control over the gaseous environment enables PLD to be used to fabricate thin films of a large class of compounds – oxides, nitrides, carbides. PLD has also been used for metallic[2] and polymer systems[3] in addition to Buckminister fullerenes[4].

But versatility is not PLD's only forte. The ability to reproduce the stoichiometry of the target (also referred to as "stoichiometry transfer") in the thin film is what made PLD popular. The superfast and intense heating of the target surface by the highly energetic laser beam (typically up to temperatures of more than 5000 K within a few nanoseconds, corresponding to a heating rate of about 10^{12} K/s) ensures that all target components, irrespective of their partial binding energies, evaporate at the same time.[5] When the ablation rate is sufficiently high (which normally is the case at laser fluences well above the ablation threshold), a so-called Knudsen layer is formed[6] and further heated (for instance by Inverse Bremsstrahlung) forming a high-temperature plasma[7], which then adiabatically swells in a direction perpendicular to the target surface. Therefore, during PLD, the material transfer between target and substrate occurs in a material package, where the separation of the species is small. Essentially, all complex structures like oxides and perovskites are built again at the substrate surface because all required components are transferred to the surface at almost the same time.

Furthermore, the laser fluence can be very easily adjusted. Polymers need a low 60 mJ/cm^2 to maintain stoichiometry in the thin film phase. However, metallic

thin films need about 5 J/cm^2. It is possible to fabricate composites and heterostructures within a single PLD setup.

By altering laser fluence on the target and gas pressure within the chamber, the kinetic energy of the ionic species leaving the target within the plume can be altered which can lead to a lot of interesting changes in texture and microstructure.

In this work, PLD has been used as the deposition technique for fabricating high quality thin films throughout chapter 3 and 4.

2.2 Atomic Force Microscopy

The atomic force microscope (AFM) is perhaps the most common kind of scanning probe microscopes (SPM). SPMs are designed to measure local properties, such as topography, height, friction, magnetism, with a probe.

AFM [8]works by scanning a very sharp (end radius ca. 10 nm) probe along the sample surface, precisely sustaining the force between the probe and surface at a user-set, low level. Usually, the probe is made of a silicon or silicon nitride cantilever with a sharp integrated tip. The forces acting on the tip when it interacts with a sample causes bending of the cantilever. This bending or deflection is picked up by a laser focused on the back of the cantilever. The laser is reflected by the cantilever onto a distant position-sensitive photodetector. This system magnifies the normal bending of the cantilever greatly, and is sensitive to Angstrom-level movements. This set-up is also known as an optical lever. The probe is moved over the sample by a piezoelectric scanner, which can make extremely precise movements. The amount by which the scanner has to move in the z axis to maintain the cantilever deflection is taken to be

equivalent to the sample topography. The combination of the sharp tip, the very sensitive optical lever, and the highly precise movements by the scanner, combined with the careful control of probe-sample forces allow the extremely high resolution of AFM.

AFM has been used to obtain images of the fabricated oxide surfaces and also to acquire fore-distance curves studied all through chapter 3.

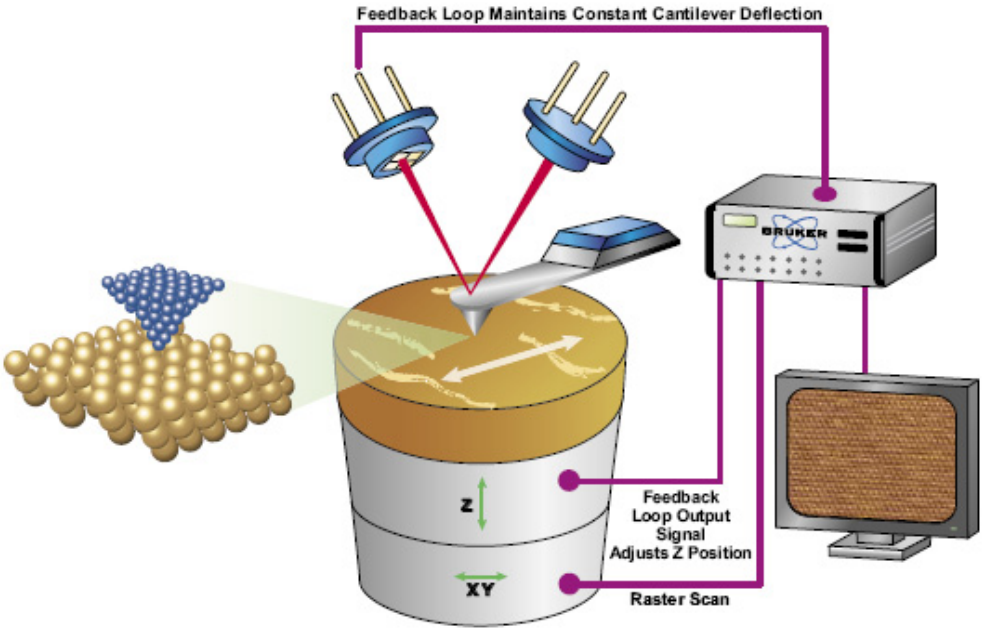

Figure 2.2 Schematic of an AFM setup *(Courtesy: Bruker)*

2.3 Scanning Electron Microscopy

Scanning electron microscopes (SEM) use an accelerated beam of electrons to generate a variety of signals which are then collected by their respective detectors. Accelerated electrons in an SEM carry significant amounts of kinetic energy. Electron sample interactions cause deceleration of the incident electrons. The energy is then lost through various processes which generate a

set of signals rich in information about the sample. These signals include secondary electrons (that produce SEM images), backscattered electrons (BSE), diffracted backscattered electrons (EBSD that are used to determine crystal structures and orientations of minerals), photons (characteristic X-rays that are used for elemental analysis and continuum X-rays), visible light (cathodoluminescence–CL), and heat.[9] While secondary electrons are most useful for generating morphological and topographical images of samples, backscattered electrons are used for acquiring contrasts in composition in multiphase or multicomponent samples. X-rays are generated by inelastic collisions of the incident electrons with electrons in discrete orbitals (shells) of atoms in the sample. When excited electrons in the sample return to lower energy states, they yield X-rays that possess a fixed wavelength (related to the difference in energy levels of electrons in different shells for a given element). Thus, characteristic X-rays are produced for each element in a sample that is hit by the incident electron beam.

SEM analysis is considered to be non-destructive. Electron interactions do not lead to volume loss of the sample, so it is possible to analyze the same samples repeatedly. SEM has been used in this work to find the particle size in metal oxide powders.

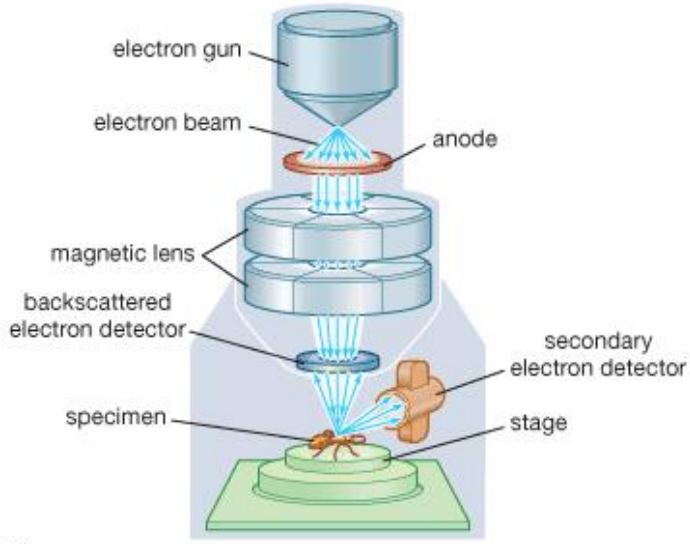

Figure 2.3 Schematic of a scanning electron microscope *(Courtesy: Encyclopaedia Britannica)*

2.4 Contact Angle and Surface Energy Measurement

2.4.1 Contact angle and surface energy

Wettability of surfaces by liquids is of great interest in a number of fields ranging from engineering to medicine. Wetting phenomena on a macroscopic scale can be illustrated using Young's equation [10]

$$\gamma_{lv}\cos\theta = \gamma_{sv} - \gamma_{sl} \qquad (2.4.1)$$

where θ is the contact angle, γ_{sl} is solid/liquid interfacial free energy, γ_{lv} is liquid/vapour interfacial tension (surface tension) and γ_{sv} solid surface free energy.

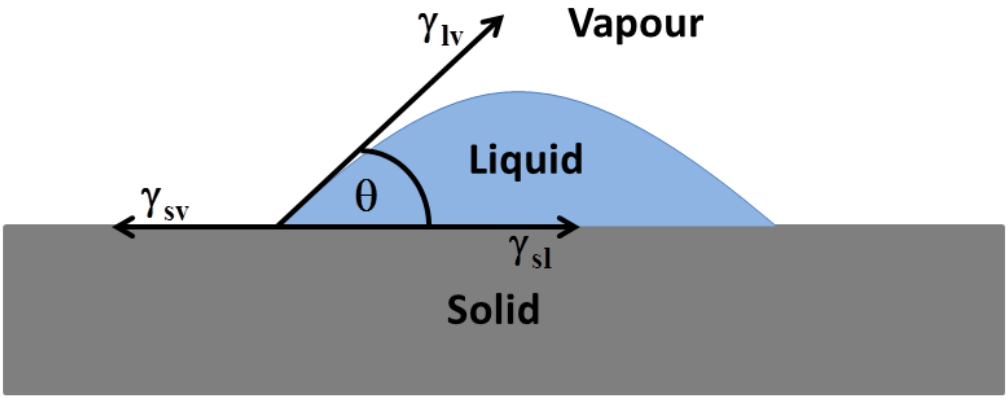

Figure 2.4 Schematic diagram of a liquid drop on a solid surface showing the interfacial tensions at three phase boundary.

The contact angle is estimated using the sessile drop technique by measuring the angle between the tangent lines along solid-liquid interface and liquid-vapour interface of the liquid contour as shown in **figure 2.4**. A contact angle of 0º and 180º correspond to complete wetting and non-wetting respectively. Surfaces exhibiting contact angles below 90º are called hydrophilic and those above 90º are called hydrophobic. In the past few decades many semi-empirical analytical models have been developed to compute surface free energy from measured contact angles such as Fowkes,[11] Owens Wendt Rabel and Kaelbel (OWRK),[12] Van Oss-Chaudhury Good/Lewis acid base theory,[13] Zisman[14] and Neumann, [15] to name a few. Each approach is targeted for measuring surface energies of either low surface energy materials or high surface materials or both. Also, the essence and physical interpretation of these approaches are different and therefore subsequently provide information on total surface energy or individual components (polar, dispersive, hydrogen bonding etc.) of surface energy or both. In our work, wide range of samples ranging from hydrophilic to hydrophobic have been presented and therefore the OWRK method has been adopted which is suitable for universal systems.

2.4.2 Description of OWRK method

Owens, Wendt, Rabel and Kaelble developed a two component model to separate the interfacial tension according to the underlying interactions between the molecules. These interactions are defined as polar and dispersive interactions. The total surface energy of the solid is the sum of the two parts. The polar interactions arise due to the permanent dipole – permanent dipole interactions or Keesom forces.[16] They are stronger and only exist in polar molecules. Dispersive component also known as London forces are weak and arise due to random fluctuations in the electron density in an electron cloud and hence lead to temporary/induced dipole interactions.[17]

In OWRK method, at least two liquids with known dispersive and polar parts of surface tensions are needed to compute the solid surface free energy as there are two unknowns (solid/liquid interfacial free energy and solid surface free energy). The combining rule proposed by OWRK model is indicated below.

$$\gamma_{sl} = \gamma_{sv} + \gamma_{lv} - 2\left(\sqrt{\gamma_{sv}^{D}\gamma_{lv}^{D}} + \sqrt{\gamma_{sv}^{P}\gamma_{lv}^{P}}\right) \qquad (2.4.2)$$

Where $\gamma_{sv}{}^{D}$ and $\gamma_{lv}{}^{D}$ are dispersive components and $\gamma_{sv}{}^{P}$ and $\gamma_{lv}{}^{P}$ are polar components of solid and liquid surface energies respectively.

Substituting for γ_{sl} from equation (1),

$$\sqrt{\gamma_{sv}^{D}\gamma_{lv}^{D}} + \sqrt{\gamma_{sv}^{P}\gamma_{lv}^{P}} = \frac{1}{2}[\gamma_{sv} + \gamma_{lv} - (\gamma_{sv} - \gamma_{lv}\cos\theta] \qquad (2.4.3)$$

$$\sqrt{\gamma_{sv}^{D}\gamma_{lv}^{D}} + \sqrt{\gamma_{sv}^{P}\gamma_{lv}^{P}} = \frac{1}{2}[\gamma_{lv}(1 + \cos\theta] \qquad (2.4.4)$$

By dividing $\sqrt{\gamma_{lv}^{D}}$ in equation (4), we get,

$$\sqrt{\gamma_{sv}^{D}} + \sqrt{\gamma_{sv}^{P}}\sqrt{\frac{\gamma_{lv}^{P}}{\gamma_{lv}^{D}}} = \frac{1}{2}\frac{[\gamma_{lv}(1+\cos\theta]}{\sqrt{\gamma_{lv}^{D}}} \qquad (2.4.5)$$

The above equation can be represented in the linear form,

$$c + mx = y \qquad (2.4.6)$$

where in, $c = \sqrt{\gamma_{sv}^{D}}$ $\quad m = \sqrt{\gamma_{sv}^{P}}$ $\quad x = \sqrt{\frac{\gamma_{lv}^{P}}{\gamma_{lv}^{D}}}$

A graphical representation of the OWRK method is shown in **figure 2.5** for lubricated hard disk media sample. The polar [SFTP(l)] and dispersive components [SFTD(l)] of total surface tension [SFT(l)] of the liquids used in this study are known (**Table 2.1**) and are substituted to compute the polar and dispersive components of the surface free energy of the solid. The slope of the graph gives the polar component and the vertical intercept gives the dispersive component of the solid surface free energy.

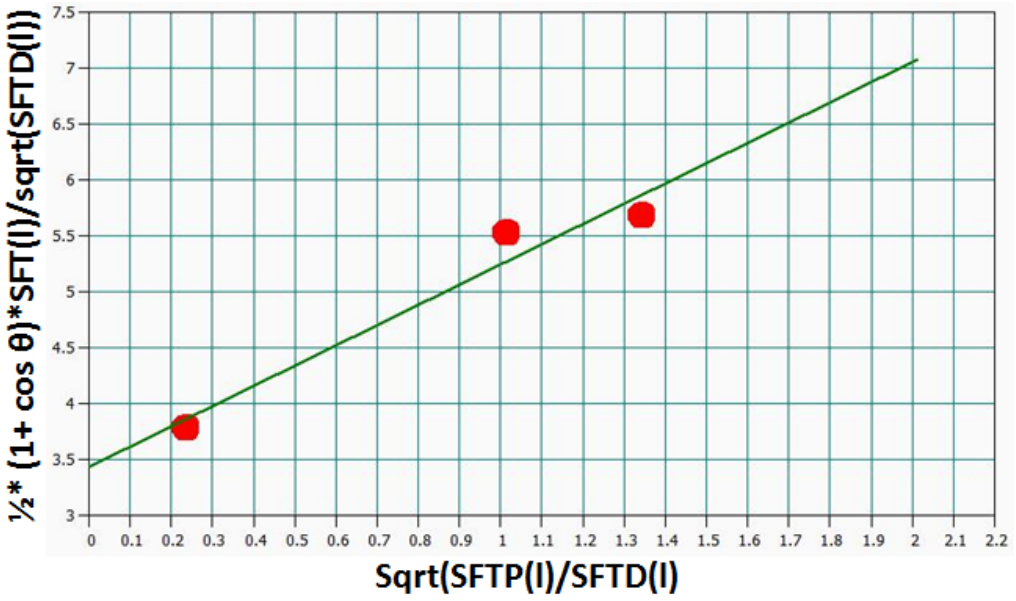

Figure 2.5 Surface energy (polar and dispersive) calculation graph based on OWRK model for lubricated hard disk media

Table 2.1 Surface tensions of the test liquids

Label	**SFT (Total) mN/m**	**SFT (Dispersive) mN/m**	**SFT (Polar) mN/m**	**Values Adapted From**
Water	72.80	26	46.80	Gebhardt et al.
Ethylene Glycol	47.70	26.40	21.30	Gebhardt et al.
Diiodomethane	50.00	47.40	2.60	Busscher et al.

2.5 Surface Plasmon Resonance

2.5.1 Surface plasmons

Surface plasmons (SPs), sometimes also called surface plasmon polaritons, are electromagnetic waves that propagate in a direction parallel to the metal/dielectric (or metal/vacuum) interface, along the surface of separation. In 1902, Wood[18] illuminated a metallic diffraction grating with polychromatic light and noticed narrow dark bands in the spectrum of the diffracted light. He almost dismissed them as unexplained anomalies. Fano followed up on Wood's report with theoretical work, diligently explaining these anomalies to be associated with the excitation of electromagnetic surface waves on the surface of the diffraction grating. Thereafter, Otto[19], Kretschmann and Raether, Agerwal[20], and Swalen[21] have performed exhaustive and comprehensive work which has not only successfully established an easy method but also a verifiable theory for the excitation of surface plasmons and their investigation, consequently opening up the domain of surface plasmons in modern optics.

Surface plasmons originate from collective oscillations of the quasi-free electron gas at the interface between a metal and a dielectric. From Maxwell's equations with standard boundary conditions, it is possible to show that an interface between a metal and a dielectric can support SP mode with the propagation constant β as:

$$\beta = k_0 \sqrt{\frac{\varepsilon_d \varepsilon_m}{\varepsilon_d + \varepsilon_m}} \qquad (2.5.1)$$

where $k_0 = \omega/c = 2\pi/\lambda$ is the wave number of light in vacuum with angular frequency ω, wavelength λ, and speed c. $\varepsilon_m = \varepsilon'_m + i\varepsilon''_m$ and ε_d are the permittivity of metal and the semi-infinite dielectric respectively and i is equal to $\sqrt{-1}$. Metals like gold, silver and aluminium which have a negative and real part of permittivity ($\varepsilon'_m < 0$) can support SPs.

Assuming $|\varepsilon'_m| >> \varepsilon''_m$ the propagation constant β of the surface plasmon can be written as

$$\beta = Re\{\beta\} + iIm\{\beta\}$$

Plugging in the values from equation

$$\beta = \frac{\omega}{c}\sqrt{\frac{\varepsilon_d \varepsilon'_m}{\varepsilon_d + \varepsilon'_m}} + i\frac{\varepsilon''_m}{2(\varepsilon'_m)^2}\frac{\omega}{c}\left(\frac{\varepsilon_d \varepsilon'_m}{\varepsilon_d + \varepsilon'_m}\right)^{\frac{3}{2}} \quad (2.5.2)$$

where Re{ } and Im{ } denote the real and imaginary part of a complex number, respectively. The imaginary part of the propagation constant is associated with the attenuation of the surface plasmon propagation.

At the metal dielectric interface, the amplitude of the SP electromagnetic field is at its maximum. Away from the interface, it decays, exponentially into both the metal and dielectric media, as shown in **figure 2.7**. L_p is used to represent the field decay in the direction perpendicular to the metal dielectric interface. It is defined as the distance from the interface at which the amplitude of the field decreases by a factor of 1/e.

For the metal, the penetration depth expressed as

$$L_{pm} = 1/Im\{k_{zm}\} = 1/Im\left(\frac{\omega}{c}\frac{\varepsilon_m}{\sqrt{\varepsilon_m + \varepsilon_d}}\right) \quad (2.5.3)$$

For the dielectric, similarly

$$L_{pm} = 1/Im\{k_{zd}\} = 1/Im\left(\frac{\omega}{c}\frac{\varepsilon_d}{\sqrt{\varepsilon_m + \varepsilon_d}}\right) \quad (2.5.4)$$

Z being the direction into the metal and dielectric (going into plane of paper in **figure 2.7**) Propagation losses in the metal cause damping of surface plasmons travelling along a metal/dielectric interface. The finite propagation length L_x of

SPs is defined as the distance in the x-direction where the energy of the surface plasmon has decreased by a factor of 1/e.

$$L_x = \frac{1}{2Im\{\beta\}} \tag{2.5.5}$$

2.5.2 Excitation of surface plasmons

Theoretically, surface plasmons can be excited by the bombarding the metal with electrons. However, due to the ease of experimental implementation optical excitation is more commonly used. The SP dispersion curve asymptotically approaches the light line at low energies as in **figure 2.6** whereas for higher energies it approaches the cutoff angular frequency ω_{max} that is proportional to the metal plasma frequency

$$\omega_{max} = \frac{\omega_p}{\sqrt{1+\varepsilon_d}} \tag{2.5.6}$$

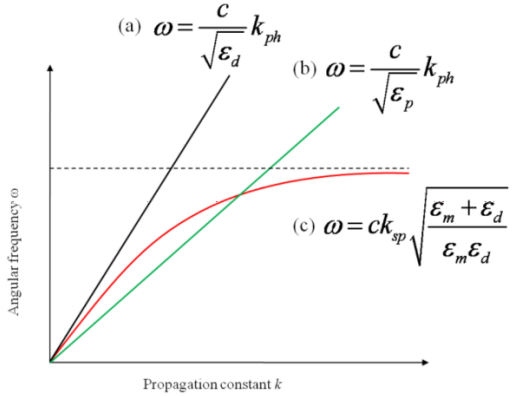

Figure 2.6 The dispersion relation of free photons in a dielectric (a), and in a coupling prism (b) with $\varepsilon_p > \varepsilon_d$, compared to the dispersion relation of non-radiative surface plasmons (c) at the metal/dielectric interface

Considering that the momentum of free photons travelling through a dielectric medium (2.6a) is always smaller than the propagation constant Re{β} of SPs (2.6c) at the dielectric/metal interface

$$k_{ph} = \frac{\omega}{c}\sqrt{\varepsilon_d} < Re\left\{\sqrt{\frac{\varepsilon_d \varepsilon_m}{\varepsilon_d + \varepsilon_m}}\right\} = Re\{\beta\} \qquad (2.5.7)$$

These two waves cannot be phase matched along the metal surface due to the insufficient k_{ph}. Therefore they cannot be directly coupled. To optically excite SPs, we have to employ a coupling enlargement. In this work, we use a prism coupler and use the attenuated total reflection method (ATR). In the Kretschmann geometry (used throughout chapter 4) a laser beam is incident on a 50 nm gold film through a prism of permittivity ε_p. If Re{β} of surface plasmon at the interface between the metal and the lower refractive index dielectric is matched to the one of the incident optical wave, surface plasmons are generated

$$\frac{\omega}{c}\sqrt{\varepsilon_p} sin\theta = Re\{\beta\} \qquad (2.5.8)$$

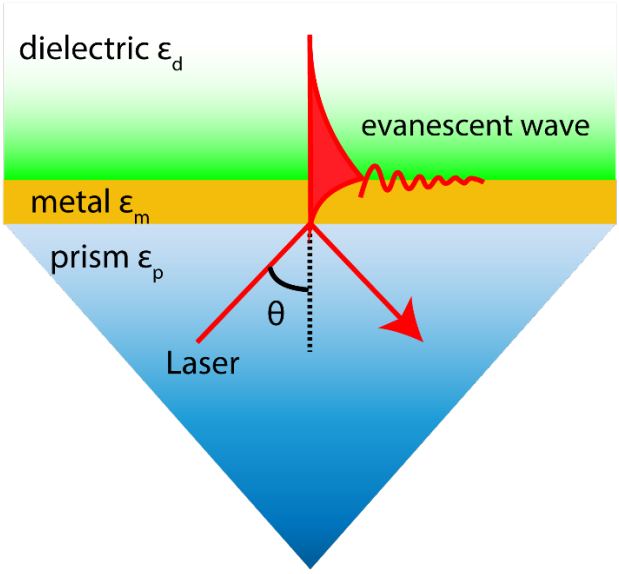

Figure 2.7 A schematic of how SPs are excited in the Kretschmann configuration

The strength of coupling between the incoming optical wave (laser) and the surface plasmons wave, therein excited, can be changed by altering the thickness of the metal layer. Excitation of SPs manifests itself as a narrow absorption dip in angular spectrum reflectivity as measured with a photodetector placed in the path of the reflected laser beam. The particular angle at this which occurs can be calculated from the formula

$$\theta = \arcsin Re\left\{\sqrt{\frac{\varepsilon_d \varepsilon_m}{(\varepsilon_d+\varepsilon_m)\varepsilon_p}}\right\} \qquad (2.5.9)$$

A typical angular spectrum of reflectivity is shown in **figure 2.8.**

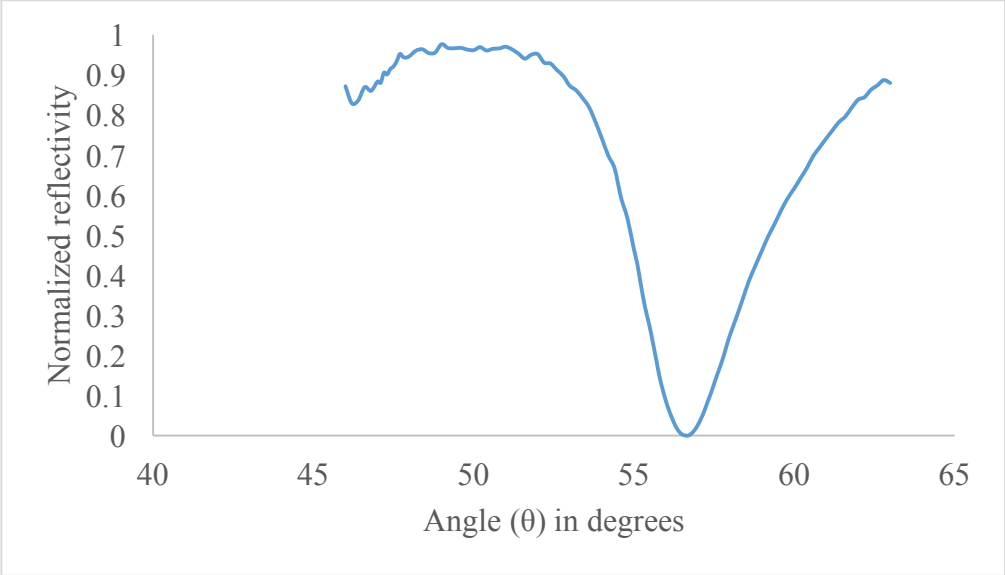

Figure 2.8 Angular spectrum of reflectivity showing a dip at 56°

2.5.3 Optical sensing with surface plasmon resonance

In the beginning, surface plasmons were used in the characterization of thin films and the study of processes at metal boundaries. Since then, however, surface plasmons have marked their entry in non-linear optics, lasers, optical data storage, photonic bandgap structures, sub-diffraction imaging and optical sensors. We will now discuss how SPR has been used for biosensing purposes.

2.5.4 Working principle of SPR biosensors

If we take the most reductionist view, SPR biosensors are thin-film refractometers that have the ability to measure extremely tiny changes in the refractive index occurring at the surface of a metallic films which support the excitation of SPs. SPR biosensors consist of two major components

a) The optical setup for the excitation and interrogation of SPs

b) Biomolecular recognition elements (BRE)

The BRE are typically immobilized on the sensor surface or in the sensitive layer (e.g. alginate matrix in chapter 5 of this study) probed by evanescent field of resonantly excited SPs. Whenever analyte molecule binds to BRE, the refractive index in the close proximity of the gold (or SP supporting metallic surface) changes by δn, which in turn causes a change of propagation constant $\delta\beta$. The $\delta\beta$ changes the coupling condition to SPs, as indicated in equations (2.5.1) and (2.5.8). So by measuring variations of the characteristics of the light wave coupled to the SP wave at the metal dielectric interface, we can investigate molecular binding events with the BRE.

In chapter 4, the BRE we are using is a thin layer of transition metal oxide which have certain affinity towards phospholipids. This is a departure from the normal use scenario where sensing elements are covalently bonded to the gold surface. When dealing with a thin film of metal oxide on the surface of gold, there are two issues which need to be tackled.

1. **Thickness** – The thickness of the film cannot be more than 3 nm. This is because at higher thicknesses, the angle at which resonance is observed becomes greater than 60°. The setup could not measure reflectivity at those angles because of geometrical constraints. It must be noted, most commercial setups will not measure binding events at such angles as well. Hence, by using equations shown above, we could simulate the angle which could be measured within our limitations and

get to know what thickness of films will work for us. A simulation for 5 nm film of Sc_2O_3 is shown in **figure 2.9**

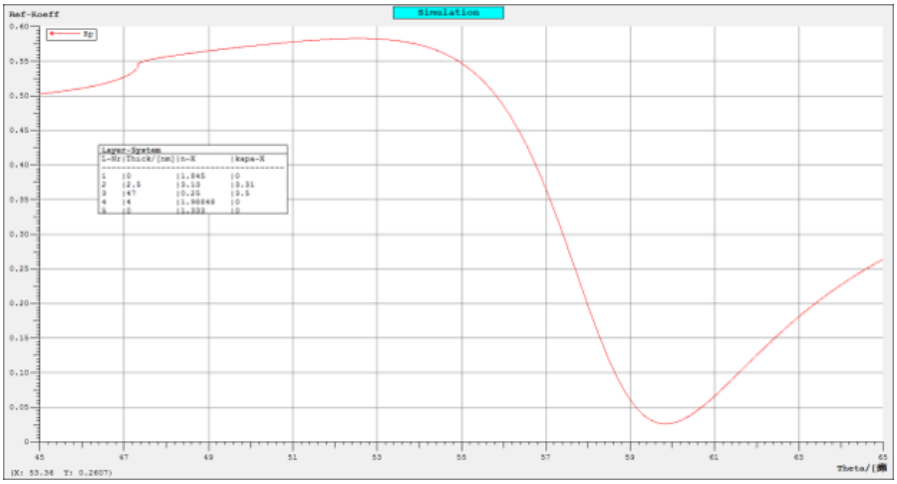

Figure 2.9 Simulation of angular spectrum of reflectivity of Sc2O3 (5 nm) film on a gold (50 nm) film in water. Resonance occurs at 59.9°

2. **Adhesion of oxide film to gold** - Usually, sensing elements are covalently bonded to the gold surface through some chemical linker molecules. These tend to be very stable on the surface. In the case of oxide thin films, this issue is non-trivial. We use the PLD process described in **section 2.1** to deposit the thin film onto the gold surface. However, as we learned through experiment, it is difficult to stabilize thin films grown at room temperature on the surface. Under flow of buffer solution, these films would simply delaminate and get washed away. We even had cases of chunks of films breaking off, which could be monitored by the SPR response. Usually, in the PLD process, by raising deposition temperatures above 500 °C, adhesion to substrate is improved. But, the gold would boil off under the high vacuum and 500 °C conditions inside the chamber. Through rigorous trials, we could optimize the deposition conditions under which we could obtain highly

stable metal oxide thin films on gold. Thereafter, we are able to monitor very precisely the amount of phospholipids which bind to the thin film of transition metal oxide.

In SPR biosensor with angular modulation (used in chapter 4), a monochromatic light wave (632.8 nm laser in this case) is used to excite an SP wave. There are two parameters that can be monitored to record molecular binding events taking place on the surface. One is the angular SPR reflectivity dip $\Delta\theta$ and the other is reflectivity change ΔR at an angle set very near to the resonance dip. The principle of operation of SPR biosensors measuring the binding-induced refractive index changes as a shift in the SPR resonant angle $\Delta\theta$, or the changes of reflectivity ΔR is shown in **figure 2.10**

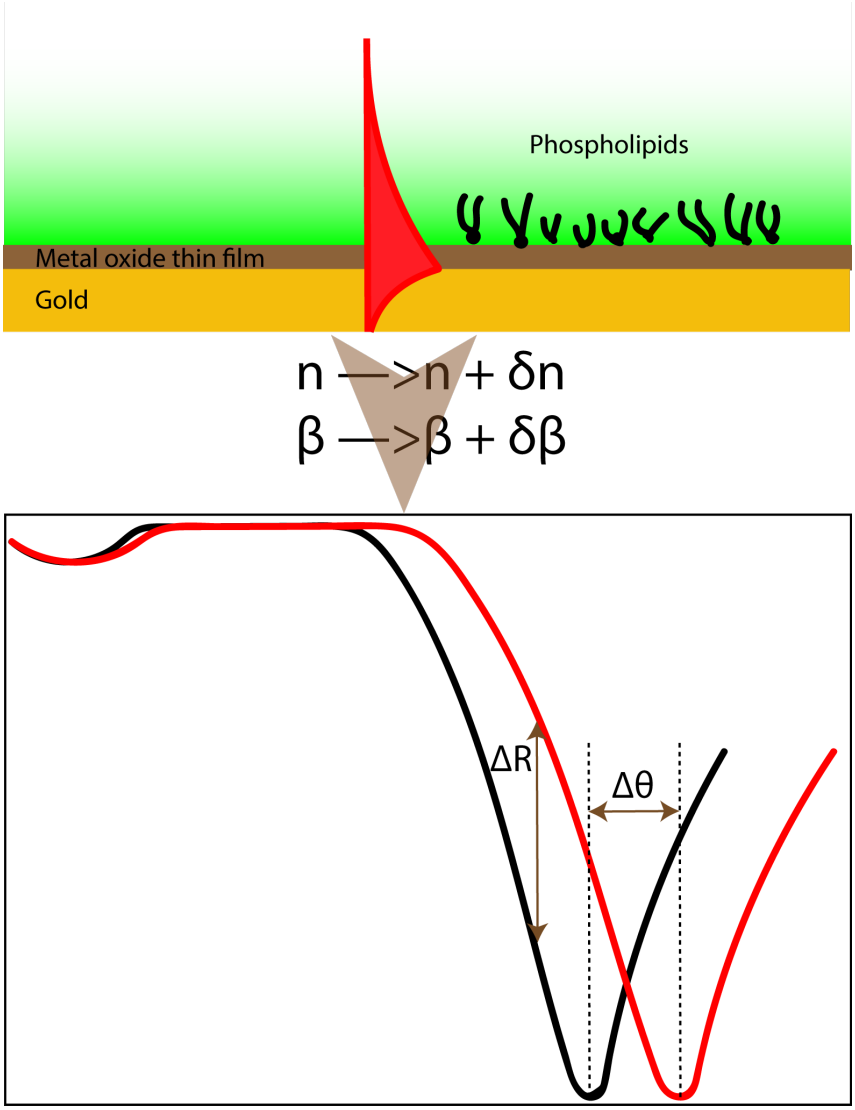

Figure 2.10 Working principle of SPR biosensor in angular mode of operation, used in chapter 4 to find amount of phospholipid bound to thin film of metal oxide

2.6 Rutherford Backscattering Spectroscopy

Rutherford Backscattering Spectroscopy (RBS) is named after Ernest Rutherford who discovered the atomic nucleus in the very famous experiment which involved the bombarding of a very thin gold foil by energetic alpha particles (He^{2+}) in the year 1911. S. Rubin et al. were the first scientists to use nuclear scattering for detection of elements up to a depth of several μm[22]. The

method gained popularity with the invention of solid state detectors in 1970. The interest fueled a lot of scientific efforts and investment which consequently made RBS a very powerful technique for structural and compositional characterization of thin films or single crystals.

An ion beam of energetic (typically few MeV) beam of a (He^{2+}) particles is produced by an electrostatic accelerator and is directed towards the sample by the use of magnets. Some part of the incident beam is backscattered due to collisions with nucleus of elements present in the sample. These collisions can be accurately modeled as an elastic collision using classical physics. The energy of the backscattered ion is a function of atomic mass of the element and it asymptotically approaches the energy of the incident particles as the mass of target atom increases. The number and energy of the backscattered ions from the sample is detected. The energy of the backscattered ions is used to identify elements and the count is used to get elemental concentration.[23]

Also energy of the ions which are backscattered by the same element at some depth in the film is lower than the one on the surface. This energy loss is dependent on sample composition and density. This is used for measurement of film thickness and depth profiling. The count of backscattered alpha particles as a function of energy gives a spectrum which is analyzed to get the chemical composition and thickness of the film.

In this thesis, RBS has been used only for checking elemental composition of thin films and obtaining their thickness.

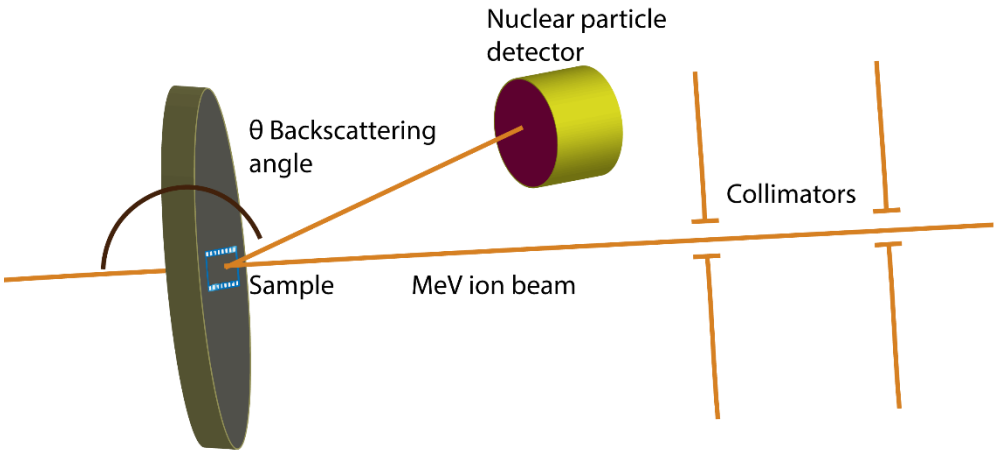

Figure 2.11 Rutherford backscattering spectroscopy layout

2.7 Mass Spectrometry

John B. Fenn, the inventor of electrospray ionization for biomolecules and the 2002 Nobel Laureate in Chemistry, described mass spectrometry as follows

"Mass spectrometry is the art of measuring atoms and molecules to determine their molecular weight. Such mass or weight information is sometimes sufficient, frequently necessary, and always useful in determining the identity of a species. To practice this art one puts charge on the molecules of interest, i.e., the analyte, then measures how the trajectories of the resulting ions respond in vacuum to various combinations of electric and magnetic fields.

Clearly, the sine qua non of such a method is the conversion of neutral analyte molecules into ions. For small and simple species the ionization is readily carried by gas-phase encounters between the neutral molecules and electrons, photons, or other ions. In recent years, the efforts of many investigators have led to new techniques for producing ions of species too large and complex to be vaporized without substantial, even catastrophic, decomposition."

There are four major components of a mass spectrometer

A. Sample inlet – to introduce the sample in a compatible format into the mass spectrometer
B. Ionization source – to generate ions from the sample
C. Mass analyzer – to sort ions according to mass and charge
D. Ion detector – to measure the separated ions

A schematic has been shown below

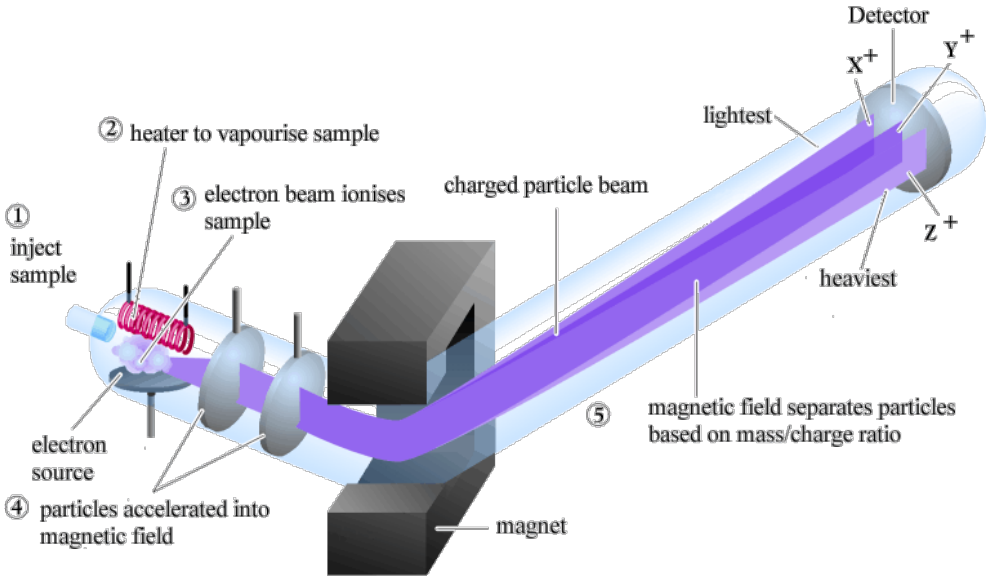

Figure 2.12 Simplified layout of a mass spectroscopy setup *(Courtesy: Francis Carey, McGraw Hill Higher Education)*

Two types of ionization sources have been used in this thesis, hence we would enter a short discussion about it.

2.7.1 Matrix Assisted Laser Desorption Ionization

Tanaka, Karas, and Hillenkamp introduced matrix-assisted laser desorption/ionization mass spectrometry (MALDI-MS) in 1988[24, 25]. MALDI is a soft ionization technique in which the energy from the laser is used to volatilize the matrix rather than degrading the sample. This technique is based upon an ultraviolet absorbing weak organic acid. The matrix and sample are dissolved in an appropriate solvent which also prevents aggregation of the sample. The sample–matrix mixture is placed under vacuum conditions; the solvent is removed, leaving behind co-crystallized sample molecules hopefully, homogenously dispersed within matrix molecules. The exact mechanism is not known but it is believed that when the pulsed UV laser is tuned to the appropriate frequency, it causes the ionization and transfer of a sample from the condensed phase to the gas phase via laser excitation and ablation of the sample. The co-crystallized sample molecules vaporize instantly without having to directly absorb energy from the laser. The directed energy transfer during a matrix-assisted laser-induced desorption event provides quite high ion yields of the intact sample, and allows for the measurement of compounds with sub-picomole sensitivity.

Once vaporized, the desorbed charged molecules are guided by an electric field from the MALDI ionization source into the mass analyzer. Most commonly, time-of-flight (TOF) mass analyzers are used to sort the ions according to their mass-to-charge ratio (m/z).

The popularity of MALDI for biomolecule analyses is due to its high sensitivity, suitability for application to complex mixtures, tolerance for salts in millimolar

concentrations in addition to the fact that it is a soft ionization method which causes little or no fragmentation of species.

In **section 4.3.1**, we have deposited thin films of metal oxides on the commercially obtained MALDI target plate for the purpose of testing efficacy of phospholipid capture by these thin films. In **section 4.3.5** we have fabricated a thin strip of oxide on the commercial target plate for the purposes of on target enrichment. The modifications are described in detail in the respective sections.

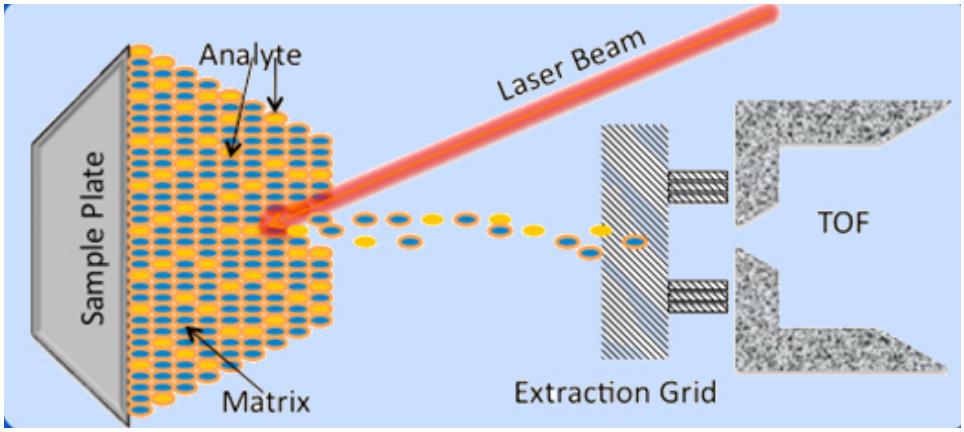

Figure 2.13 Schematic of a MALDI setup *(Courtesy: NPTEL, India)*

2.7.2 Electrospray Ionization

Dole carried out the practical development of electrospray ionization (ESI) though the first experiments were performed by Chapman in the 1930s. Subsequently, he also discovered the important phenomenon of multiple charging of molecules. However, it was truly Fenn's work[26] (for which he was awarded the Nobel Prize) that ultimately led to the modern day technique

of electrospray ionization mass spectrometry and its application to biological macromolecules.

Within the ESI setup, the voltage applied (700V to 5000V) to the needle produces an electrical gradient on the fluid flowing through. Either dry gas, heat, or both are applied to the droplets at atmospheric pressure thus causing the solvent to evaporate from each droplet. This electrical gradient separates the charges at the surface of the flowing fluid. Consequently, the fluid is forced to emerge from the needle as a Taylor cone. The tip of the Taylor cone, thus formed, keeps protruding as s fine filament until such a point where the fluid reaches the Rayleigh limit where the surface tension of the fluid equals the electrostatic repulsion. At this point, highly charged droplets leave the filament. The charged droplets that have emanated from the filament are attracted to the entrance of the mass spectrometer (through electrostatic lenses) due to the high opposite voltage at the mass analyzer's entrance. As these droplets now traverse the distance towards the mass analyzers, the Coulombic repulsion generated by the similar charges on the droplets' surface comes to exceed the surface tension holding the droplets together. When this happens, the droplets burst into much smaller droplets thereby also releasing the ions. Hence, the overall function of ESI is to produce gaseous ionized molecules directly from a liquid solution.

Electrospray ionization is regularly used for analyzing peptides, proteins, carbohydrates, small oligonucleotides, synthetic polymers, and lipids. Since ESI involves the continuous flow of solution, it is highly suitable for using as an interface with High Performance Liquid Chromatography (HPLC) or capillary electrophoresis.

NanoESI has become popular in recent years. This setup is a variant of the standard ESI, whereby advances in instrumentation has made it possible to have an extremely small spray needle which is placed exceedingly close to the mass analyzer. Such an arrangement ultimately results in an increase in efficiency which essentially means that smaller amounts of sample are required.

In this thesis, ESI-MS has been used to evaluate lipid fraction enrichment through metal oxide µcolumns.

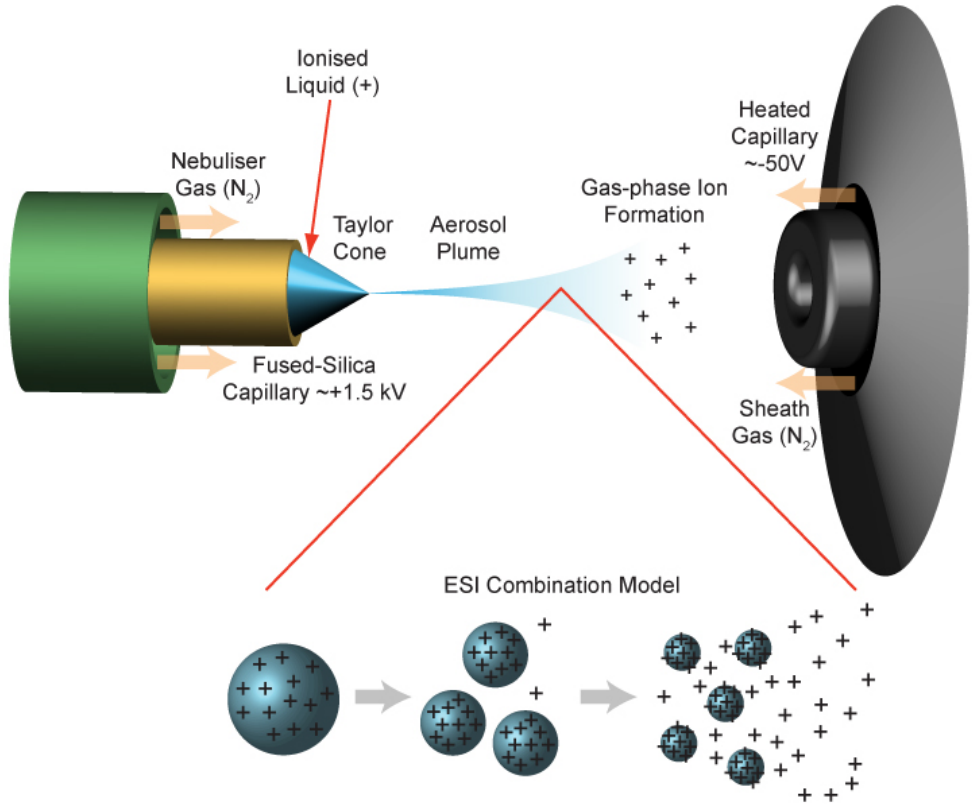

Figure 2.14 Schematic of a electrospray ionisation setup *(Courtesy: Lamond Lab)*

2.8 Liquid Chromatography

The earliest reports, perhaps pioneering, of liquid chromatography as we know it today are the work of Russian botanist, Mikhail S. Tswett[27]. The flash of brilliance he had was to separate leaf pigments (extracted from leaves using an organic solvent) by running them through a column packed with chalk (calcium carbonate) and alumina particles. He followed this with a run of pure solvent. As the force of gravity pulled the sample through the column, the various pigments separated into differently colored bands. Tsewett had thereby, succeeded to analytically separate different components in a complex mixture exploiting their inherent distinct partitioning ratio between the moving solvent (mobile phase) and the chalk or alumina particles (stationary phase).

We will take a look at two subtypes of liquid chromatography that has been used in this work.

2.8.1 Thin Layer Chromatography

Thin layer chromatography (TLC) is a planar version of column chromatography. The stationary phase is, in this case, a thin layer of silica or alumina, immobilized onto a metal or glass plate. The sample to be analyzed is spotted using a micropipette near the base of the plate. A volatile organic solvent is filled in the container as shown in the figure. The solvent level is so adjusted such that is just touches the spot. The container is then sealed of so that the environment inside the chamber is saturated with vapor of the organic solvent. The solvent carries the sample as it moves by capillary action through the dry

particle bed thereby partitioning the various components according to their relative affinities for the stationary phase and the mobile phase.

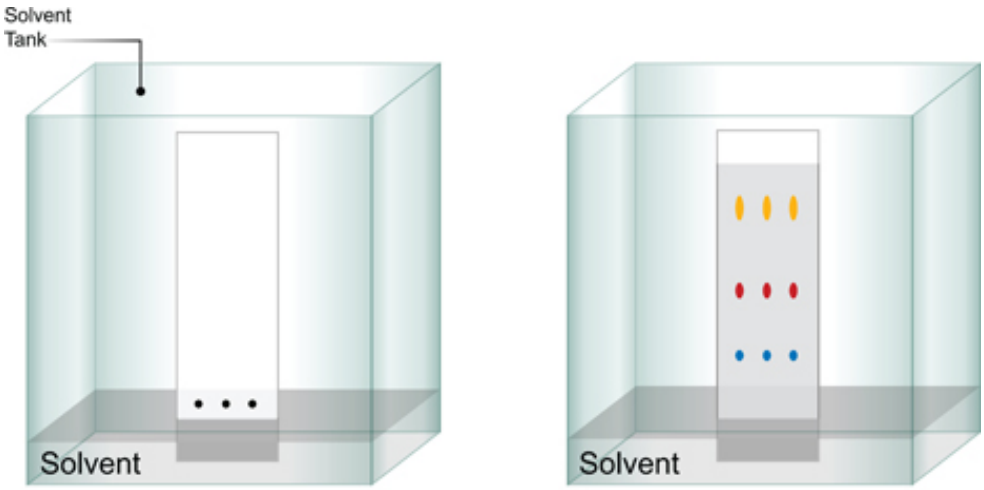

Figure 2.15 Schematic of a thin layer chromatography setup *(Courtesy: Waters)*

2.8.2 High Performance Liquid Chromatography

As its name aptly suggests, high performance liquid chromatography (HPLC) is a technological upgrade on liquid chromatography. Instead of using gravity as the driving force for dragging the sample through the column, HPLC uses a powerful pump which pushes the sample through the column at pressures exceeding 6,000 psi (400 bar).

The acronym HPLC was coined by late Prof. Csaba Horváth in 1970 when pumps had a maximum capability of 500 psi or 35 bar. He called it high pressure liquid chromatography[28]. However, advances in technology and instrumentation soon made it possible for pumps to generate 6000 psi. When this advancement was coupled with more advanced detectors, sample injectors and better columns, HPLC really began to establish itself as a very powerful

tool in analytical chemistry. Over time, the expansion of the acronym was changed to high performance liquid chromatography.

Today a lot of scientific effort is directed towards making very sensitive and durable columns which make it easy to separate compounds present even in parts per trillion concentrations. Due to these capabilities, HPLC has become indispensable to proteomics, lipidomics, pharmaceuticals, food, nutraceuticals, cosmetics, environmental matrices, forensic samples, and industrial chemicals domains.

2.8.2.1 Normal Phase HPLC

In his pioneering experiment, Tsewett had used a polar stationary phase (chalk and alumina) and a much less polar mobile phase to accomplish the segregation of the dyes in the leaf extract. This scheme came to be generically known as normal phase HPLC, where the stationary phase is much more polar than the mobile phase. Hence, due to polar-polar interactions, the polar components in the complex mixtures are retained much more strongly than the apolar components.

2.8.2.2 Reverse Phase HPLC

As is obvious from the nomenclature, this is the scheme where the conditions of the mobile and stationary phase are reverse of the normal phase. Hence, in reverse phase HPLC (RP-HPLC), the mobile phase is much more polar than the stationary phase. Consequently, apolar components are retained most strongly and polar components are eluted quicker.

2.9 References

1. Dijkkamp, D., et al., *Preparation of Y-Ba-Cu oxide superconductor thin films using pulsed laser evaporation from high Tc bulk material.* Applied Physics Letters, 1987. **51**(8): p. 619-621.
2. Krebs, H.U. and O. Bremert, *Pulsed laser deposition of thin metallic alloys.* Applied physics letters, 1993. **62**(19): p. 2341-2343.
3. Hansen, S. and T. Robitaille, *Formation of polymer films by pulsed laser evaporation.* Applied physics letters, 1988. **52**(1): p. 81-83.
4. Curl, R.F. and R.E. Smalley, *Fullerenes.* Scientific American, 1991. **265**: p. 54-63.
5. Fähler, S. and H.-U. Krebs, *Calculations and experiments of material removal and kinetic energy during pulsed laser ablation of metals.* Applied surface science, 1996. **96**: p. 61-65.
6. Kelly, R., et al., *Laser sputtering: Part I. On the existence of rapid laser sputtering at 193 nm.* Nuclear Instruments and Methods in Physics Research Section B: Beam Interactions with Materials and Atoms, 1985. **9**(3): p. 329-340.
7. Phipps Jr, C., et al., *Impulse coupling to targets in vacuum by KrF, HF, and CO2 single-pulse lasers.* Journal of Applied Physics, 1988. **64**(3): p. 1083-1096.
8. Binnig, G., C.F. Quate, and C. Gerber, *Atomic force microscope.* Physical review letters, 1986. **56**(9): p. 930.
9. Goldstein, J., et al., *Scanning electron microscopy and X-ray microanalysis: a text for biologists, materials scientists, and geologists*. 2012: Springer Science & Business Media.
10. Young, T., *An essay on the cohesion of fluids.* Philosophical Transactions of the Royal Society of London, 1805: p. 65-87.
11. Fowkes, F.M., *Calculation of work of adhesion by pair potential suummation.* Journal of Colloid and Interface Science, 1968. **28**(3–4): p. 493-505.
12. Owens, D.K. and R.C. Wendt, *Estimation of the surface free energy of polymers.* Journal of Applied Polymer Science, 1969. **13**(8): p. 1741-1747.
13. Van Oss, C.J., R.J. Good, and M.K. Chaudhury, *The role of van der Waals forces and hydrogen bonds in "hydrophobic interactions" between biopolymers and low energy surfaces.* Journal of Colloid and Interface Science, 1986. **111**(2): p. 378-390.
14. Fox, H. and W. Zisman, *The spreading of liquids on low-energy surfaces. II. Modified tetrafluoroethylene polymers.* Journal of colloid science, 1952. **7**(2): p. 109-121.
15. Zenkiewicz, M., *New method of analysis of the surface free energy of polymeric materials calculated with Owens-Wendt and Neumann methods.* Polimery, 2006. **51**(7-8): p. 584-587.
16. Keesom, W. *The second viral coefficient for rigid spherical molecules, whose mutual attraction is equivalent to that of a quadruplet placed at their centre*. in *Proc. R. Acad. Amsterdam*. 1915.
17. London, F., *The general theory of molecular forces.* Transactions of the Faraday Society, 1937. **33**(0): p. 8b-26.

18. Wood, R.W., *On a remarkable case of uneven distribution of light in a diffraction grating spectrum.* 1902.
19. Otto, A., *Excitation of nonradiative surface plasma waves in silver by the method of frustrated total reflection.* Zeitschrift für Physik, 1968. **216**(4): p. 398-410.
20. Agarwal, G., *New method in the theory of surface polaritons.* Physical Review B, 1973. **8**(10): p. 4768.
21. Swalen, J., *Optical properties of Langmuir-Blodgett films.* Journal of molecular electronics, 1986. **2**: p. 155-181.
22. Rubin, S., *Surface analysis by charged particle spectroscopy.* Nuclear Instruments and Methods, 1959. **5**(3): p. 177-183.
23. Chu, W.-K., *Backscattering spectrometry*. 2012: Elsevier.
24. Karas, M. and F. Hillenkamp, *Laser desorption ionization of proteins with molecular masses exceeding 10,000 daltons.* Analytical chemistry, 1988. **60**(20): p. 2299-2301.
25. Karas, M., et al., *Matrix-assisted ultraviolet laser desorption of non-volatile compounds.* International journal of mass spectrometry and ion processes, 1987. **78**: p. 53-68.
26. Yamashita, M. and J.B. Fenn, *Electrospray ion source. Another variation on the free-jet theme.* The Journal of Physical Chemistry, 1984. **88**(20): p. 4451-4459.
27. Tswett, M., *Physikalisch-chemische Studien über das chlorophyll. Die Adsorptionen.* Berichte der Deutschen botanischen Gesellschaft, 1906. **24**(316-323): p. 20.
28. Horvath, C. and S. Lipsky, *Column design in high pressure liquid chromatography.* Journal of Chromatographic Science, 1969. **7**(2): p. 109-116.

3 Quantifying interactions between water and surfaces

3.1 Abstract

In this chapter, we deploy an atomic force microscopy-based approach to locally probe surface wettability. The maximum pull-off force as calculated from force spectroscopy shows a remarkable correlation with the macroscale water contact angle, measured over a wide variety of surfaces starting from hydrophilic, all the way through to hydrophobic ones. This relationship, consequently, facilitates the establishment of a universal behavior. The adhesion and capillary forces scale with the polar component of surface energy. However, no such relation could be established with the dispersive component. Hence, we postulate that the force(s) which enable us to correlate the force spectroscopy data measured on the nano scale to the macroscopic contact angle are primarily arising from electrostatic-dipole-dipole interactions on the surface. London forces play less of a role. This effect in is line with density functional theory (DFT) calculations suggesting a higher degree of hydroxylation of hydrophilic surfaces. This result shows that molecular simulations and measurements on an atomic scale can be extrapolated to macroscopic surface wetting problems.

3.2 Introduction

3.2.1 Overview

In the context of the organization of this thesis work, we begin our studies by trying to understand how solid surfaces interact with perhaps the most common and indispensable liquid molecule – water. Solid-liquid interfaces have been of interest in photo-catalysis, water splitting and the design of novel super-hydrophilic/hydrophobic surfaces.[1, 2] The fundamental understanding of interfacial phenomenon has been crucial for various self-assembled monolayers (SAM),[3-5] biological processes[6-8] and technologies such as dip-pen lithography.[9, 10] Intrinsic wetting properties arising from inherent surface chemistry have attracted particular interest recently.[2] Wetting properties and surface free energies at macro-scale are ultimately governed by the intermolecular interactions and surfaces forces on the nanoscale. Conventional methods such as contact angle measurements[11] and inverse gas chromatography[12] are employed widely for measuring these wetting properties.

3.2.2 Literature review and the need for a new technique

With the development of nano and micro-scale devices e.g., fluidic devices wetting measurements on small dimensions become important. However, the above methods (like contact angle measurements[11] and inverse gas chromatography[12] techniques) do not work on the nanometer scale and there

is a need for the development of alternative approaches. Some efforts have been made recently to understand the solid-liquid interface of a hydrophilic surface using nano-ultrasonics.[13] Several numerical simulations have been performed to understand the intriguing phenomena that happen at nanoscale and how they go on to affect the macroscale wetting properties as measured through contact angle.[14, 15] The nature of adhesion forces responsible for these phenomena has been a topic of debate.[11] A significant amount of work has been reported on the study of adhesion properties using atomic force microscopy (AFM).[11, 16-18] At this point, it is important to note that the capillary forces between the AFM tip and the surfaces form a significant part of the overall adhesion forces.[11, 16, 18, 19] However, the capillary forces alone cannot explain the large adhesion observed on hydrophilic surfaces without assuming other strong liquid-solid interaction.[20, 21] Eastman et al reported that the adhesion force is significantly reduced when a hydrophobic tip is used[16]. The large reduction of adhesion cannot be explained by van der Waals interactions in Derjaguin-Muller-Toporov (DMT) and Johnson-Kendall-Roberts (JKR) methods. Hence, there is obviously another numerically dominant force, possibly originating from the intrinsic chemical nature of surfaces.

3.2.3 Motivation and rationale

To plug existing gaps in our knowledge of interfacial phenomenon, this force needs to be quantified and related to other measurable surface properties. With this aim, we combine macroscale contact angle measurements with force spectroscopy (FS) to ultimately demonstrate that the maximum pull-off force

(adhesion) is an exponential function of macroscale water contact angle and surface energy. We would like to point out that this force correlates well with the polar component of the surface energy while finding no such relation with the dispersive component. This is an unambiguous pointer to the nature of this force that we have measured. We can, therefore, say that the measured force arises from electrostatic-dipole-dipole interaction (hydrogen bonding) on the surface and London forces (induced-dipole-dipole interactions) do not play a significant role. Density functional theory (DFT) calculations indicate the tendency of hydrophilic surfaces to stabilize hydroxyl groups, providing the linkage to create interfacial hydrogen bonds with liquid water.

3.3 Results and discussion

3.3.1 Measurement of contact angles on surfaces and calculation of surface energies

Figure 3.1 shows the contact angle measurement results on different surfaces. **Figure 3.1 (a)** is a schematic of vapor-liquid-solid interfaces where Θ, λ_{lv}, λ_{sv}, λ_{sl}, are contact angle, interfacial free energies of liquid/vapor, solid/vapor, solid/liquid respectively. **Figure 3.1 (b-f)** shows samples of water contact angle ranging from 0° (superhydrophilic) to ~ 102° (hydrophobic). The contact angle is related to interfacial energies through Young's equation $\lambda_{sv} = \lambda_{sl} + \lambda_{lv} \cos(\Theta)$. The contact angles have an intrinsic component which originates from the specific chemical composition of the surface and unsaturated intramolecular bonds thereon, and an external component due to roughness or any periodic structures.

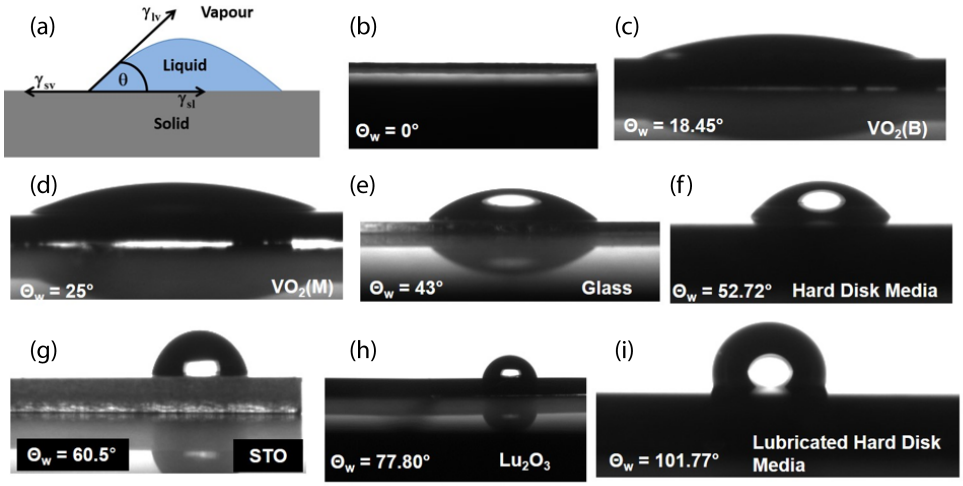

Figure 3.1 Water contact angle measurement **(a)** schematic of measurement **(b-i)** different surfaces having contact angle ranging from 0° to ~ 102°

In order to probe the local forces arising solely due to the intrinsic chemical nature, we chose smooth surfaces of comparable root mean square (RMS) roughness measured by AFM as shown in **figure 3.2**. There is a small variation in the amount of roughness between the films as can be observed (Figure 2) but it does not influence the intrinsic surface energy. It has been widely reported that roughness in any hydrophilic surface reduces the water contact angle [11]. However, Sun *et al* have shown that surface features below ~ 50 nm will not trap sufficient air to introduce Cassie-Baxter heterogeneity.[8] The observed roughness variations in our experiments (0.2 – 3 nm) are far too small to influence the contact angle. To further substantiate our point, we would raise the case of VO_2 (M phase) and VO_2 (B phase). The film of VO_2 (M phase) has a higher RMS roughness (~ 2 nm) than VO_2 (B phase) (RMS roughness ~ 0.6 nm) but their contact angles are ~ 25° and 18.5° respectively. If roughness was influencing the contact angle, VO_2 (M phase) should have had a lower contact angle as compared to VO_2 (B phase). With roughness out of the way, it is now

appropriate to claim that it is the surface chemistry and atomic structures which are contributing to the macroscale contact angle and surface energy in this study.

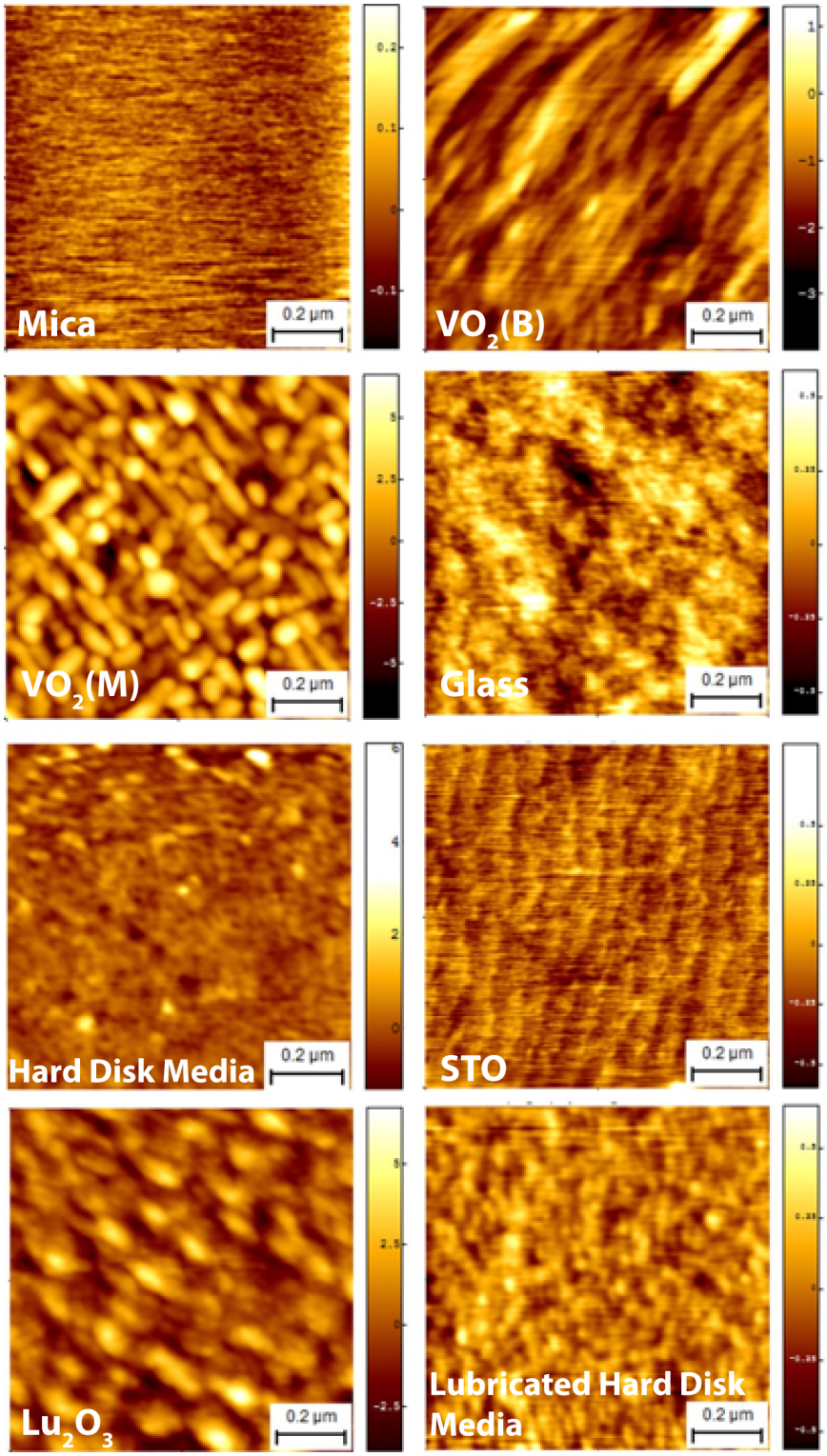

Figure 3.2 Atomic force microscopy topographic images of different surfaces

Table 3.1 Contact angles on various surfaces obtained with three different liquids and calculations of surface energies with its two components

	Contact Angle (degrees)			Surface Energy (T)	Surface Energy (D)	Surface Energy (P)	Convergence
	Water	Ethylene Glycol	Diiodomethane				
Mica	**0**	20.4	45.7	65.9	15.8	50.2	0.93
VO_2 (B)	**18.4**	16.0	27.3	61.6	24.0	37.6	0.90
VO_2 (M)	**25.0**	5.5	20.5	60.3	27.4	32.9	0.91
Glass	**43.0**	27.3	41.4	51.0	23.1	27.9	0.94
Hard Disk Media (CoCrPt Magnetic layer)	**52.7**	49.3	44.0	42.8	22.4	20.4	0.86
$SrTiO_3$ (STO)	**60.5**	15.7	31.7	47.4	34.8	12.6	0.99
Lu_2O_3	**77.8**	63.1	49.5	33.1	28.1	5.0	0.84
Lubricated Hard Disk Media	**101.8**	89.0	87.7	14.0	11.1	2.9	0.97

As per Fowkes method, these interactions can be interpreted as the geometric mean of a dispersive and polar component of surface tensions σ^D and σ^P respectively. The solid/liquid interfacial energy can be written as

$$\gamma_{sl} \approx \sigma^s + \sigma^l - 2\left(\sqrt{\sigma_s^D \cdot \sigma_l^D} + \sqrt{\sigma_s^P \cdot \sigma_l^P}\right)$$

Therefore, two or more liquids with known polar and dispersive components are used to find the solid surface free energy using OWRK model. The OWRK

method separates the interfacial surface tension according to the underlying interactions (polar and dispersive) between the molecules. Hence, the total surface energy of the solid is the sum of polar and dispersive components. The polar component originates from the permanent dipole-dipole interactions. They are stronger in polar molecules (having permanent dipole moment). On the other hand, the dispersive component arises due to random fluctuations in the electron density when brought together, leading to an induced dipole-dipole interaction (London forces). The detailed description of OWRK model and fitting results are shown in supplementary. Importantly, the convergence factor (indicated in **Table 3.1**) is very close to ~ 1, showing this model is very suitable to calculate surface energies with a high degree of accuracy.

3.3.2 Force spectroscopy on surfaces with native water layer

Figure 3.3 shows the force spectroscopy (FS) measurements on these samples in ambient conditions. **Figure 3.3 (a)** shows a schematic of the measurement. Very thin water layer [few atomic unit cells] is condensed between the AFM tip and the hydrophilic surfaces in ambient conditions.[10, 16, 17] The adsorbed water does not evaporate in capillary conditions between tip and sample at ambient conditions as per Kelvin's equation.[22] **Figure 3.3 (b)** is a typical curve obtained on hydrophilic surface. The probe is first brought from non-interaction regime (showing no deflection of cantilever on detector) and pushed towards the sample (bending of cantilever due to repulsive forces showing positive deflection), and then retracted back to original position.

A detailed schematic illustration of the events that occur during the retraction of the tip has been given in **figure 3.4**. The negative deflection represents the attractive forces that hold the tip to the surface during retraction. The sharp detachment occurs when the pulling force of cantilever exceeds the intrinsic attractive force **(figure 3.4 B)**. **Figure 3.2 (b-i)** shows the various force-distance curves obtained on a variety of samples with contact angle ranging from 0° to 102°. These figures show that the maximum pulling force reduces significantly as the contact angle increases. The maximum pulling force represents the tip-sample surfaces adhesive force occurring in **figure 3.4 (B)** just before the tip breaks free from the liquid meniscus.

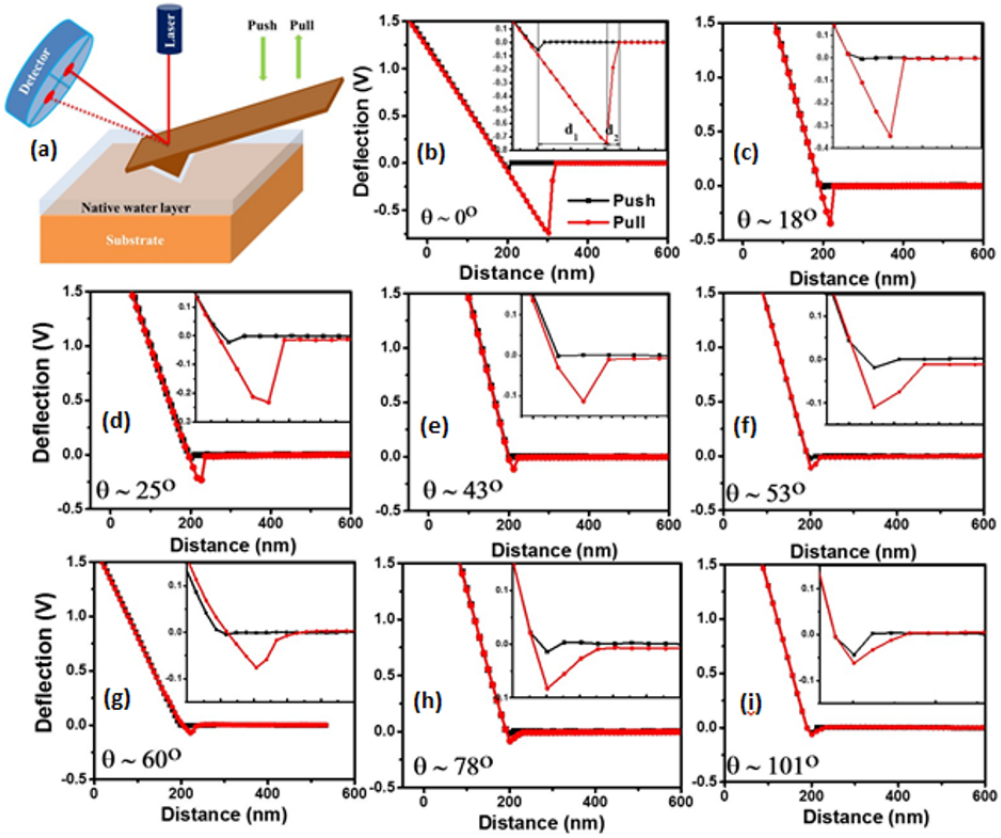

Figure 3.3 Force spectroscopy (FS) measurements in ambient conditions, **(a)** schematic of measurement **(b-i)**. FS curve on different surfaces having contact angle ranging from 0° to ~ 102°, [**b** –mica, **c** – VO_2(B) grown on STO, **d** – VO_2(M) grown on STO, **e** – cover slip glass, **f** – hard disk media, **g** – STO substrate, **h** – Lu_2O_3 grown on YSZ, **i** – lubricated hard disk media.]**Inset:** the curves plotted at a scale to clearly show the behaviour near detachment point. Distances before detachment from the surface (d_1) and the distance travelled by the probe in contact with the liquid meniscus (d_2) are shown in (b).

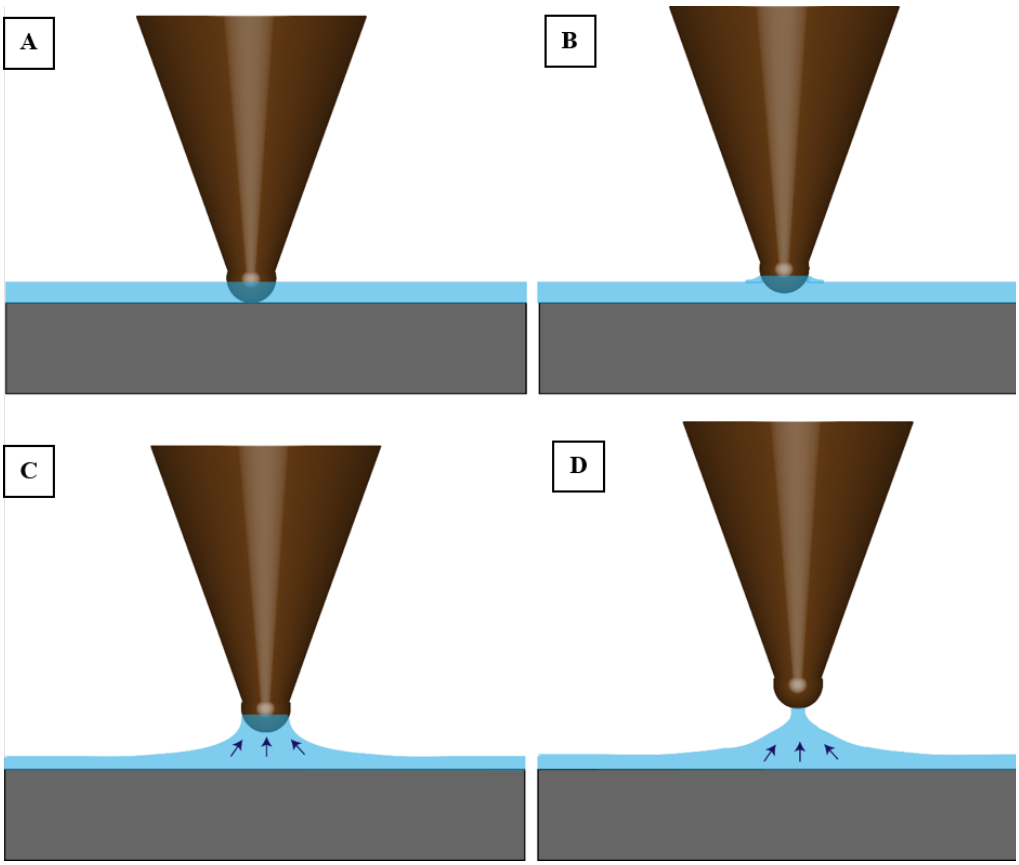

Figure 3.4 Illustration depicting the various phases of tip interaction with the surface in the case of retraction (going away) from the sample. **(A)** Tip leaves the solid surface, **(B)** tip travels through the film of adsorbed water, **(C)** tip extends the neck of the meniscus formed by the water, **(D)** ultimately, the tip breaks free from the film of water

Indeed, there have been numerous studies on the adhesive forces over a period of time.[11] The adhesion force has been reported to be a function of humidity[18, 19] and the hydrophilic nature of surfaces.[16] Under ambient conditions, a meniscus is formed between the tip and a hydrophilic surface. The resulting capillary forces have been used to account for the pull-off forces in prior literature. Capillary forces are found to be stronger in hydrophilic surfaces.[16-19] However, numerical simulations along with some experimental results on mica surfaces have shown that the pulling force was incommensurately high compared to the expected capillary forces.[16, 20, 21,

23] Some classical theories do exist for tip-sample interactions: Hertz method assumes a linearly elastic sphere indenting an elastic surface but neglects the surface force and adhesion; JKR method is generally suitable for samples with high adhesion but ignores the long-range interactions outside the contact area and DMT method takes in to account the forces outside the contact area and is usually suited for samples with low adhesion. These theories have been developed considering simple van der Waals interaction. Particularly, the popular JKR model relates surface energy $\Delta\gamma \approx -\frac{2}{3\pi}\frac{F_{\max}}{R}$,[11] where $\Delta\gamma$, F_{max}, and *R,* are surface energy, maximum pulling force and radius of tip respectively. However, capillary forces and pure van der Waal interactions have consistently failed to explain the inordinately high adhesion force observed in experimental results.[20, 21] Consequently, there is a gap in the understanding of the nature of adhesive and capillary forces intrinsic to hydrophilic surfaces. Indeed, there is insufficient experimental data on the correlation between adhesion forces and surface energy to validate the behavior of these models.

3.3.3 Correlating nanoscale measurements with macroscale measurements

Figure 3.5 (a-d) shows the maximum pulling force with different parameters of macroscale contact angle measurements. **Figure 3.5 (a)** shows that the maximum pulling force decreases exponentially with the contact angle. Most interestingly, it shows an exponential increase with the polar component of surface free energy **[figure 3.5 (b)]** but not the dispersive component **[figure 3.5 (c)]**.

As per JKR model, the maximum pulling force should increase linearly with the surface energy. We, however, observe an exponential trend. Here, we show a universal plot between pulling force versus the water contact angle and surface energy which is not only important for applications in probing these properties at nanoscale but also predicting the universal trend of adhesion forces with surface energy. Importantly, it is the polar component of surface energy that follows this relationship and not the dispersive component. The polar component of surface energy arises from the hydrogen bonding (which is due to electrostatic-dipole-dipole interaction) with the surface. In this case, the participating molecules and surfaces have a permanent dipole moment. On the other hand, the dispersive component of surface energy arises from "London forces" by inducing the instantaneous dipole moment, thereby giving a weak dipole-dipole interaction (van der Waals interaction). The scaling of the pull-off force with the polar component of surface energy and not the dispersive component provides clear evidence of electrostatic-dipole-dipole interaction being the key mechanism behind adhesive forces. Interestingly, in **figure 3.3** the detachment is not sharp enough after the contact angle ~ 25° and the total distance travelled in detachment process changes with contact angle of each surface.

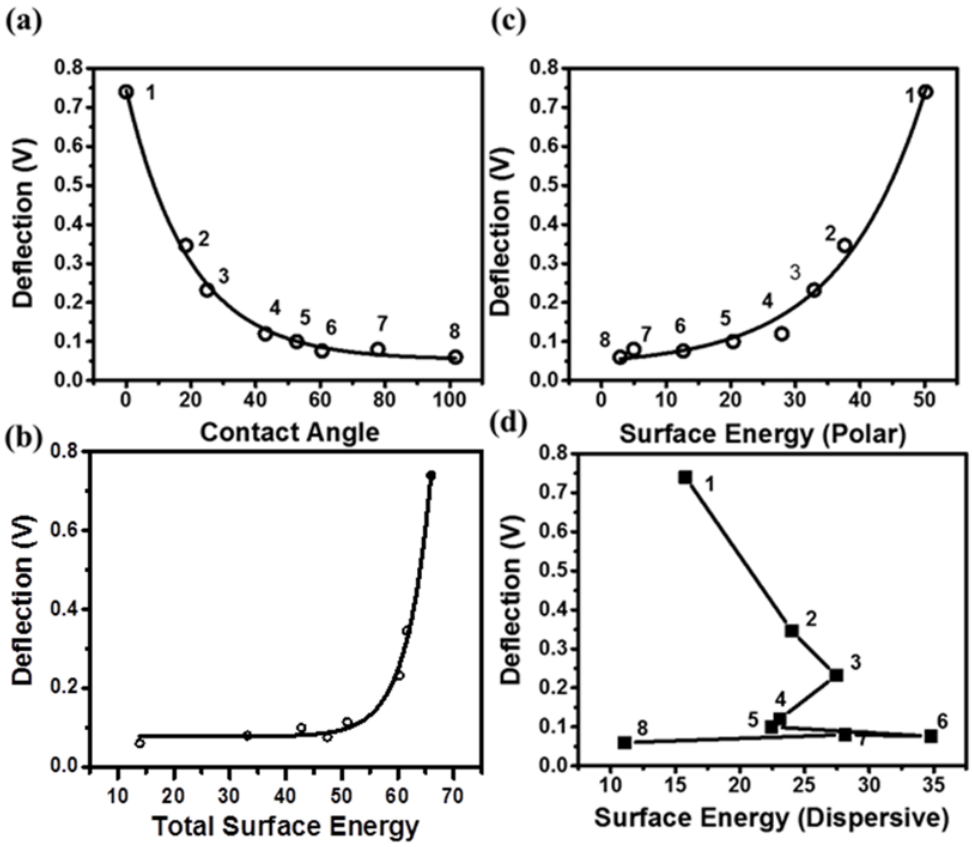

Figure 3.5 The maximum pulling force plotted versus different parameters obtained from macroscale contact angle measurements, the maximum pull-off force versus **(a)** water contact angle **(b)** total surface energy **(c)** polar component of surface energy **(d)** dispersive component of surface energy[**1** – mica, **2** – VO_2(B) grown on STO, **3** – VO_2(M) grown on STO, **4** – cover slip glass, **5** – hard disk media, **6** – STO substrate, **7** – Lu_2O_3 grown on YSZ, **8** – lubricated hard disk media.]

3.3.4 Breaking of hydrogen bonds on the surface as a possible reason for nanoscale-macroscale hydrophilicity correlation

Figure 3.6 (a) and **(b)** are the distances travelled up to a point before (d_1) and after (d_2) the maximum negative deflection is achieved (refer **figure 3.3 (b)** for graphical evaluation of d_1 and d_2) , which essentially represents the pulling distance prior to the probe just leaving the surface and its travel in contact with

liquid. The distance traveled by the probe (d_1) before detachment from the surface exponentially decreases with respect to water contact angle of the surface which is quite evident from the graph **(figure 3.6 (a))**. On the other hand, the distance travelled in contact with the liquid meniscus increases linearly **figure 3.6(b)**. Hydrogen bonding forces have been found to decay exponentially compared to van der Waals forces that follow the power law.[24] However, it is difficult to distinguish between the two possible scenarios around the breaking of the hydrogen bond – it may break either from the solid surface or from a few molecular layers above the surface. At least, in the case of mica, we think it is more likely to have the breakage of the hydrogen bond occur a few molecular layers above the solid surface. Both the surfaces in question (the AFM tip and mica) are highly hydrophilic and hence, a rather large meniscus will be formed. We would like to point out that the molecular orientation of water layer at the interface can play an important role in breaking the number of hydrogen bonds using the AFM tip in both cases (breaking from solid surface or few atomic layer above it). The number of hydrogen bonds at the surface is decided by surface atomic structure and chemical nature of different hydrophilic and hydrophobic surfaces.

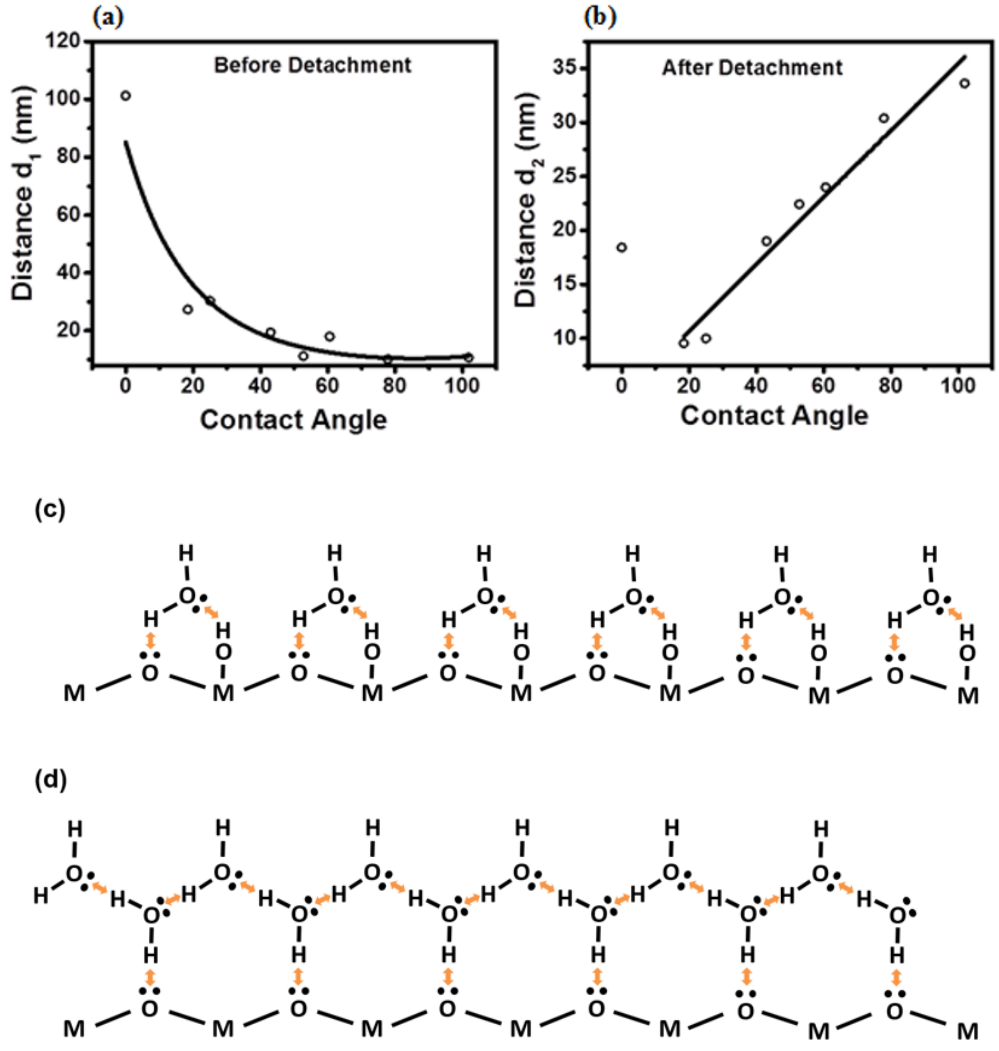

Figure 3.6 (a) and **(b)** are the distances travelled up to a point before and after the maximum negative deflection is achieved respectively. **(c-d)** schematic showing hydrogen molecule structure at the interface of highly hydrophilic surface and relatively less hydrophilic surface respectively

In order to elucidate the nature of water interaction with surfaces of varying degrees of hydrophilicity, we performed density functional theory (DFT) calculations on selected surfaces (**see appendix A-1**).

(Disclaimer: The simulation studies weren't performed by the candidate but are shown for completion. They were performed by Kelsey Stoerzinger, Yueh-Lin Lee, Livia Giordano and Yang Shao-Horn, Massachusetts Institute of Technology as part of our collaboration.)

On the clean surfaces of transition metal oxides, VO_2(M)(022) and $SrTiO_3$(001), it is favorable for water to dissociate and hydroxylate the surface. On the more ionic Lu_2O_3 water adsorbs molecularly intact at fully coordinated metal ions, while it dissociates in proximity of under-coordinated Lu^{3+} ions also present at the surface of unreconstructed (111) surface of cubic Lu_2O_3. These results indicate the crucial role of the chemical bonds inside the material, i.e. the covalency of the oxygen-metal bond in this case, and of the surface structure in the interaction with water. Further insight can be gained by comparing the stability of hydroxyl groups. On the VO_2 surface, the hydroxyl groups are found to be stable, while a less favorable adsorption is found on $SrTiO_3$(001). This difference can be attributed the different oxidation ability of the two oxides. On Lu_2O_3, the OH adsorption is unfavorable at fully coordinated sites while it readily occurs at more exposed low coordinated sites. The measured contact angle thus scales inversely with the adsorption free energy of hydroxyl groups computed at ¼ ML coverage (where 1ML is defined as 1 OH for surface metal): ΔG_{ads} = -0.57 eV for VO_2 (contact angle 18.45°) > ΔG_{ads} = -0.01 eV for $SrTiO_3$ –BO_2-terminated surface (60.5°) > ΔG_{ads} = +0.06 eV for Lu_2O_3 (77.8°). The presence of OH groups on the surface, expected to scale with adsorption energy,

introduces polar groups on the surface which can bind adsorbed water via electrostatic-dipole-dipole interactions[15] **(figure 3.6 (c))**. Thus, the correlation of nanoscopic forces with the macroscale contact angle and surface energy (f**igure 3.5)** can be explained by considering breakage of the number of hydrogen bonds specific to a molecular structure on each surface due to its inherent atomic structure and chemical composition. The detailed analysis of molecular structure can also explain **figure 3.6 (a)** and **(b)**. In the case of more hydrophilic surfaces, a greater number of hydrogen bonds are formed perpendicular to the surface **(figure 3.6 (c))**. On the other hand, there is a significant number of in-plane hydrogen bonds in the case of less hydrophilic surfaces **(figure 3.6 (d))**. Therefore, when the probe is removed perpendicular to the surface a sharp detachment occurs when the pulling force exceeds the hydrogen bonding. This characteristic interaction force should exponentially decrease with contact angle as is seen in f**igure 3.6 (a)**. In f**igure 3.6 (b)**, we plot the distance travelled after detachment from the surface against the contact angle observed. On close observation, we find that the superhydrophilic surface (mica) differs from the trend. This is because in the all other cases, the tip being more hydrophilic than the surfaces being probed, encourages water to climb along the tip when the probe is retracted from the surface. Expectedly, the after detachment distance increases as the contact angle increases in **figure 3.6 (b)**.

3.4 Conclusion

We have demonstrated that the adhesion forces are an exponential function of macroscale water contact angle and surface energy due to strong liquid-solid interaction involved in capillary forces. These forces are dominated by

electrostatic-dipole-dipole interaction (hydrogen bonding) on the surface and/or few atomic water layers above the surface but not by London forces (induced-dipole-dipole interactions). This work clearly shows that molecular simulations of wetting using a small number of atoms typical of the atomic force measurements, may enable us to predict macroscopic wetting properties of surfaces and opens new avenues for fundamental understanding of interfacial phenomenon in technologies such as dip-pen lithography and probing wetting properties on the nanoscale. For example, we can use such an approach to locally evaluate surface energies and probe contact angles for nano patterned surfaces. In such a scenario, using the conventional water droplet method would result in obtaining a value which is an average of all local values.

Hence in this chapter, we have looked at how we can use the traditional force-distance curves to explain how water, the simplest biomolecule, interacts with unreactive inorganic surfaces, in the process enabling wetting measurements to be made in the nanoscale. In the next chapter, we will move to studying a more complex class of biomolecules lipids, typically weighing around hundreds of daltons, interacting with inorganic metal oxide surfaces.

3.5 Experimental details

3.5.1 Sample fabrication

1. **Sample 1** (mica) & **Sample 4** (cover slip glass) were commercially procured.
2. **Sample 2 & 3**: Monoclinic VO_2(B) and VO_2(M) thin films on (100)$SrTiO_3$(STO) substrates were grown using PLD respectively. The target was laser ablated using a pulsed KrF Excimer laser having a wavelength of $\lambda = 248$ nm and pulse width of approximately 12 ns. The laser energy density was fixed at ~2 J/cm^2 during the optimization of film growth parameters. The substrate temperature was kept 500° C throughout the deposition. At low pressure (1×10^{-4} Torr) and 5 Hz laser rep rate, M phase is stabilized. At and above a pressure of 5×10^{-3} Torr and the laser rep rate to 2 Hz gave rise to a single phase VO_2(B) film.
3. **Sample 5**: Commercial hard disk media is Ar+ ion etched to remove the conventional carbon overcoat. Hence the top surface is the CoCrPt based magnetic layer. (Though the top carbon layer is removed, it may contain traces of carbon.)
4. **Sample 6**: STO substrate was procured commercially from Crystec GMBH. The substrates were sonicated in DI water for 15 mins. After that the substrates were kept in buffered HF solution for 30 secs. They were subsequently washed wih DI water and blow dried. The treated substrates were then annealed in the furnace at 950° C for 2 hours. The ramp up rate was 5 deg/min and the ramp down rate was 3 deg/min.

5. **Sample 7**: Lu_2O_3 film was grown using PLD technique. The target was laser ablated using a pulsed KrF excimer laser having a wavelength of λ = 248 nm and pulse width of approximately 12 ns. The laser energy density was fixed ~2 J/cm^2 during the optimization of film growth parameters. The substrate temperature was kept 750° C throughout the deposition. The pressure was 10^{-6} torr throughout the deposition.
6. **Sample 8**: Commercial hard disk media is Ar+ ion etched to remove the conventional carbon overcoat and treated with high energy carbon using FCVA (Filtered Cathodic Vacuum Arc). Then the surface was treated with PFPE (Per fluoro polyether) based lubricant (Zdol 4000).

3.5.2 Contact angle measurement setup

The macroscale contact angle and surface energy measurements were carried out using the video based fully automated Data Physics optical contact angle microlitre dosing system (OCA 40 Micro). Solvent drops (1µl/drop) of DI water (more polar), ethylene glycol (intermediate polar & dispersive) and diiodomethane (more dispersive) with known surface tensions (refer **Table 3.1**) were dispensed using a Teflon coated motor driven syringe. The contact angles were measured at ambient conditions and a video was recorded (72 frames/second) for every dispensed solvent droplet. Any dynamic changes to the droplet on the surface can be precisely observed through this method. The contact angles with three different test liquids and surface free energies (polar

and dispersive) were evaluated using the sessile drop technique and Owens, Wendt, Rabel and Kaelble (OWRK) model.

3.5.3 Atomic force microscopy and force spectroscopy

The atomic force microscopy and spectroscopy measurements were done in contact mode under ambient conditions using a commercial system by Agilent (Model 5500) and the commercial tips by NANOSENSORS (Type PPP-CONT-10) of force constant ~ .02-0.77 N/m. The results are presented after repeating several measurements using many similar tips.

3.6 References

1. He, Y., et al., *Local ordering and electronic signatures of submonolayer water on anatase TiO2(101).* Nat Mater, 2009. **8**(7): p. 585-589.
2. Azimi, G., et al., *Hydrophobicity of rare-earth oxide ceramics.* Nat Mater, 2013. **12**(4): p. 315-320.
3. Kuna, J.J., et al., *The effect of nanometre-scale structure on interfacial energy.* Nat Mater, 2009. **8**(10): p. 837-842.
4. Ostuni, E., et al., *Adsorption of Proteins to Hydrophobic Sites on Mixed Self-Assembled Monolayers†.* Langmuir, 2003. **19**(5): p. 1861-1872.
5. Vezenov, D.V., et al., *Chemical Force Spectroscopy in Heterogeneous Systems: Intermolecular Interactions Involving Epoxy Polymer, Mixed Monolayers, and Polar Solvents.* Journal of the American Chemical Society, 2002. **124**(35): p. 10578-10588.
6. Yao, X., Y. Song, and L. Jiang, *Applications of Bio-Inspired Special Wettable Surfaces.* Advanced Materials, 2011. **23**(6): p. 719-734.
7. Nishimoto, S. and B. Bhushan, *Bioinspired self-cleaning surfaces with superhydrophobicity, superoleophobicity, and superhydrophilicity.* RSC Advances, 2013. **3**(3): p. 671-690.
8. Sun, T., et al., *Bioinspired Surfaces with Special Wettability.* Accounts of Chemical Research, 2005. **38**(8): p. 644-652.
9. Piner, R.D., et al., *"Dip-Pen" Nanolithography.* Science, 1999. **283**(5402): p. 661-663.
10. Hong, S. and C.A. Mirkin, *A Nanoplotter with Both Parallel and Serial Writing Capabilities.* Science, 2000. **288**(5472): p. 1808-1811.
11. Mittal, K.L., *Advances in contact angle, wettability and adhesion*. 2013: John Wiley & Sons.
12. Das, S.C., et al., *Determination of the Polar and Total Surface Energy Distributions of Particulates by Inverse Gas Chromatography.* Langmuir, 2011. **27**(2): p. 521-523.
13. Mante, P.-A., et al., *Probing Hydrophilic Interface of Solid/Liquid-Water by Nanoultrasonics.* Sci. Rep., 2014. **4**.
14. Giovambattista, N., P.G. Debenedetti, and P.J. Rossky, *Enhanced surface hydrophobicity by coupling of surface polarity and topography.* Proceedings of the National Academy of Sciences, 2009. **106**(36): p. 15181-15185.
15. Giovambattista, N., P.G. Debenedetti, and P.J. Rossky, *Effect of Surface Polarity on Water Contact Angle and Interfacial Hydration Structure.* The Journal of Physical Chemistry B, 2007. **111**(32): p. 9581-9587.
16. Eastman, T. and D.-M. Zhu, *Adhesion Forces between Surface-Modified AFM Tips and a Mica Surface.* Langmuir, 1996. **12**(11): p. 2859-2862.
17. Sedin, D.L. and K.L. Rowlen, *Adhesion Forces Measured by Atomic Force Microscopy in Humid Air.* Analytical Chemistry, 2000. **72**(10): p. 2183-2189.
18. Xu, L., et al., *Wetting and Capillary Phenomena of Water on Mica.* The Journal of Physical Chemistry B, 1998. **102**(3): p. 540-548.
19. Xiao, X. and L. Qian, *Investigation of Humidity-Dependent Capillary Force.* Langmuir, 2000. **16**(21): p. 8153-8158.

20. Jang, J., G.C. Schatz, and M.A. Ratner, *Capillary Force on a Nanoscale Tip in Dip-Pen Nanolithography.* Physical Review Letters, 2003. **90**(15): p. 156104.
21. Jang, J., G.C. Schatz, and M.A. Ratner, *Capillary force in atomic force microscopy.* The Journal of Chemical Physics, 2004. **120**(3): p. 1157-1160.
22. Thomson, W., *4. On the Equilibrium of Vapour at a Curved Surface of Liquid.* Proceedings of the Royal Society of Edinburgh, 1872. **7**: p. 63-68.
23. Burnham, N.A., et al., *Probing the surface forces of monolayer films with an atomic-force microscope.* Physical Review Letters, 1990. **64**(16): p. 1931-1934.
24. Pashley, R., et al., *Attractive forces between uncharged hydrophobic surfaces: direct measurements in aqueous solution.* Science, 1985. **229**(4718): p. 1088-1089.

4 Quantifying interactions between lipids and surfaces

4.1 Abstract

Sample preparation techniques remain one of the most prominent bottlenecks in the field of lipidomics, where the extremely skewed distribution of lipids by their class prevents the discovery and characterization of new lipid species in the lipidome. In this chapter, we study the interactions of phospholipids with surfaces made of metal oxides. Knowledge of such interactions are key to the fabrication of efficient solid phase extraction resins which can resolve the conundrum in sample preparation strategies. We present comparisons between various metal oxides with respect to their phospholipid enrichment capacities in 3 formats, first by modifying MALDI plates, second by fabricating µcolumns packed with metal oxide powder and finally third by employing a batch sample processing technique incorporating metal oxide powder. Thereafter, owing to the scatter in acquisition of data in all the former approaches, we demonstrate an extremely sensitive technique based on surface plasmon resonance to quantify phospholipid adhesion to metal oxide surfaces with sub-nanogram level accuracy. We also show the effect of the headgroup in determining the affinity to metal oxide surfaces. Finally, we demonstrate a new technique based on thin planar TiO_2 columns deposited on MALDI target plates to perform on-target enrichment on phospholipid species, in a format easily integrated into existing commercial MALDI-MS systems.

4.2 Introduction

Having discussed the interactions of water with various surfaces, we now move to a heavier class of molecules, which are very important in the state of human health. We are now going to describe studies on interactions of lipids with inorganic oxide surfaces. Since the transition from studying water to lipids is seemingly abrupt, we will provide a very detailed introduction to the class of biomolecules known as lipids and why we intend to study their interactions with oxide surfaces quantitatively.

In the interest of completeness of discussion, however, we will have to start with a larger field of study called metabolomics of which, study of lipids (lipidomics) is a part.

4.2.1 Metabolomics

The scientists, then "philosophers" of ancient Greece had the notion that changes in biological fluids are indicators of disease. In fact, in the Middle Ages "urine charts" were used to map colors, smells and tastes of urine to various diseases. Since these changes are now known to be metabolic in nature, it is fair to say that these scientists were, in fact, practicing the earliest forms of metabolomics. A medieval chart is shown in **figure 4.1.**

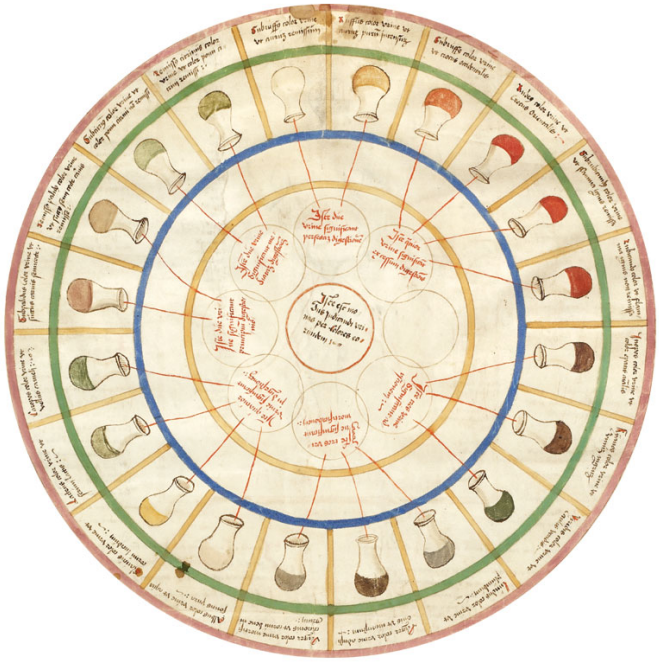

Figure 4.1 A medieval urine chart detailing conditions that can be diagnosed from change in apparent properties of urine. *(Courtesy: Scientific American)*

As is, probably, evident from the nomenclature, metabolomics is the system level study of metabolism. More specifically though, metabolomics seeks to determine and quantify, through exhaustive methods, the presence of thousands of small molecules of interest (metabolites) in cells, tissues and organisms at large. The whole field of study revolves around the governing idea – the metabolic state, at any given time, of a biological entity is the snapshot of the overall physiological state. Scientists in ancient China used ants to detect high levels of glucose in urine and thereby predicting diabetes. A thousand years later, metabolomic studies are able to capture global biochemical events by assaying thousands of small molecules in cells, tissues, organs, or biological fluids — followed by the application of informatics techniques to define metabolomic signatures. Metabolomic studies can lead to enhanced understanding of disease mechanisms and to new diagnostic markers as well as

enhanced understanding of mechanisms for drug or xenobiotic effect and increased ability to predict individual variation in drug response phenotypes (pharmacometabolomics). The identities and concentrations of these metabolites result from a complex interplay among gene expression, protein expression, and the environmental interaction. Metabolomics makes use of instruments and technologies that can simultaneously quantify thousands of small molecules in a biological sample. The data obtained from these measurements must then be processed with sophisticated mathematical tools that can look for a molecular signature among millions of sets of data. Since, it is widely accepted that disease disrupts metabolism and consequentially causes changes that are long lasting, we have an opportunity to capture the diseased state as abnormal metabolic signatures. In literature, metabolomic signatures have already been reported for several diseases, including motor neuron disease [1], depression[2], schizophrenia[3-5], Alzheimer's disease[6], cardiovascular and coronary artery disease[7, 8], hypertension[9], subarachnoid hemorrhage[10], preeclampsia[11], type 2 diabetes [12-14], liver cancer [15], ovarian cancer[16], breast cancer[17], and Huntington's disease[18]. It is important to clarify the meaning of these "signatures" at this point. The concentrations of metabolites are modified in the state of disease and after treatment with drugs – hence the new signatures. Hence, with analysis, these signatures can provide information relating to disease pathophysiology. It isn't a stretch to say that metabolomics is going to have deep implications for both basic biomedical research and medical practice because it can capture vital information pertaining to active mechanisms of disease and also of drug action,

thereby making it possible to correlate risk of disease and drug action to pathways of metabolism.

Metabolomics is an umbrella term because of the large number of metabolites in a typical organism. However, the sub-set which has captured the imagination of scientists in the last decade is lipidomics.

4.2.2 Lipidomics

The reaction of various fatty acids with backbone structures (such as, glycerol and sphingoid bases) give rise to a huge number of chemically distinct molecular species. It is believed that the lipidome of the eukaryotic cell contains more than 100,000 different lipid entities. Most remarkably, their function is as varied as their structure and chemical composition. Lipids regulate structure and chemical composition of cell membranes, store energy or become precursor to metabolites. [19, 20] Lipidomics is the systems-level study and analysis of lipids and factors that interact with lipids. It aims to analyze cellular pathways and networks by a comprehensive quantitative definition of lipidomes of biological entities – organelles to cells to organisms. In order to understand the interaction of lipids with biological factors in an organism, the first and foremost step is to extract the lipids from the tissue or cell. This complex lipid mixture is then "processed" to enable its analysis by various analytical techniques. This leads to the derivation of the 'lipid profile'. This so called lipid profile contains information pertaining to the lipid composition and abundance of lipid species in the extract. As is common in the field of proteomics and genomics, one tries to understand which lipids show variation in their levels of presence

(upregulation/downregulation) as and when we perturb the biological homeostasis of the system under investigation .

For a very long time, lipids have been viewed as building blocks of the cell membrane with absolutely no other function other than structural. It is a fact that the ultimate macromolecular architecture of lipid assemblies, are decided, at least in part, by the geometrical properties of individual lipid molecules. For clarity, it is prudent to discuss the case of phosphatidylcholine and phosphatidylethanolamine. The size and orientation of the choline headgroup of phosphatidylcholine forces the fatty acid chains to contort into a geometric shape resembling a cylinder. Hence, phosphatidylcholine molecules, when lined up next to each other, will adopt a bilayer arrangement. Phosphatidylethanolamine, however, tends to form a hexagonal shape by itself due to its reduced headgroup size and state of hydration. The shape and packing of lipid molecules in macromolecular assemblies are important factors having significant effects on the dynamics of membranes — for example, in intermediates of membrane fusion and in the formation of specialized microdomains. [21]

Precise determination of molecular lipid species becomes important not only in lieu of understanding their individual roles and functions but also to shed light on their distinct behavior in a lipid collective. Ultimately this will open up new avenues in cell biology, biochemistry and biophysics. The fact that lipidomics is going to answer questions relating to the complex lipid metabolism machinery and its relation to the construction of new cellular membranes is also going to be of paramount importance to our understanding of human diseases. It is already known that atherosclerosis, infectious diseases, Alzheimer’s disease and

cancer all have a lipid component in their epidemiology. As the mechanisms of action are understood, it will unravel the main culprits in the course of a disease affliction. This will lead to better targeted drugs aimed at the cause, rather than the symptoms.

Lipids are also biomarkers, which means that even before we start discussing treatment of diseases, it will be interesting to point out the potential of lipids to be diagnosis tools. Lipid levels are tightly regulated, spatially and temporally, in the various parts of the human body. It is not outlandish to expect that deregulation of this network contributes to the onset of a pathological condition. This idea is indeed supported by a wide variety of human diseases (as pointed out above) that are associated with abnormal lipid metabolism.

In the field of nutrition research, an understanding of lipids is going to enable innovation of healthier food formulas. Furthermore, it will be possible to engineer nutrition specific to people with particular needs.

The applications are practically endless.

This brings us to the motivation of this study. One of the technological bottlenecks in lipidomics revolves around sample preparation. Unfortunately, the improvements in instrumentation which have produced increasingly sensitive mass spectrometers has not been complemented by similar advances in separation science. In essence, what we are trying to do, thereby, is to better sample preparation for mass spectrometry.

4.2.3 The need for sample preparation

There are reports in literature about metabolomic profiling dating as far back as 1960-70. But technological advances in instrumentation combined with the need for multiple levels of profiling (in addition to proteomics and genomics) has renewed interest in the field. While far more sophisticated instrumentation has pushed the limits of detection by orders of magnitude, sample preparation and analytical procedures at large have remained the technological bottleneck in the domain. Consequently, it is an active area of research and a subject of many reviews in literature. The choice of sample preparation strategy is absolutely crucial to the success of the experiment. Surprisingly, it has also been one of the overlooked sections of the field. Obviously, the choice of the sample preparation strategy will influence the observed metabolite profile and quality of data obtained. If the capabilities and limitations of the method is not understood clearly, there is a definite possibility that the accuracy of the biological interpretations or conclusions drawn from the data is compromised. Considering the chemical diversity of the metabolome, there can be no one perfect strategy for sample preparation which ensures no bias in the processed sample towards certain groups in the metabolome. In this thesis, we will focus only on sample preparation for lipidomics in particular.

The ultimate goal of the sample preparation step is to reproducibly transform the sample of interest into a "format" which is compatible with the LC-MS analysis approach while keeping the original composition unaltered as much as possible. So if we were to describe the desired qualities of a sample preparation strategy, they would be

1. Simple and fast
2. Minimum number of steps
3. Compatible with automation
4. Reproducible
5. Cheap

There are two major types of strategies which are employed in the preparation step - Liquid-liquid extraction (LLE) and Solid Phase extraction (SPE). We will discuss LLE and its disadvantages which dictate the need for SPE. Thereafter we are going to describe SPE and its details.

4.2.3.1 Liquid-liquid extraction (LLE)

The working principle of LLE is that a sample is partitioned between two immiscible liquids (also called phases) in the ratio of its solubilities in the respective phases. Most commonly, one phase is aqueous and the other is organic. Hence the more polar hydrophilic compounds separate into the aqueous phase and the non-polar hydrophobic compounds separate into the organic phase.

The distribution coefficient K_{dist} describes the partition of a particular compound between two immiscible solvents. The process of separation of a sample X between an aqueous and an organic solvent can be written as

$$X(aq) \leftrightarrow X(org)$$

$$K_{dist} = \frac{[X_{org}]}{[X_{aq}]}$$

Where X_{org} and X_{aq} are the activities of X in the two solvents.

Ideally, K_{dist} needs to be as high as possible so that high degree of separation can be attained in a single run. However if K_{dist} is not high enough, we can use continuous LLE in which the sample is subject to multiple runs of the LLE as illustrated above with fresh organic solvent every time.

With a basic understanding of the process of LLE, we are now in a position to discuss its limitations which in turn are reasons to move to SPE.

1. **Limited selectivity** – LLE works on the basis of differences in solubilities of analytes and the unwanted contaminants in aqueous and organic solvents. Since most lipids are soluble in organic solvents, all lipids are co-eluted together in the organic phase. This means that the extract will have all non-polar interferences and will be less pure than we want it to be.
2. **Large amount of solvents required** – It is necessary to use an adequate amount of solvents to extract all the lipids of interest from the complex sample. It is desirable to use as less of these solvents as possible because more often than not, they are both expensive and not environment-friendly.
3. **Emulsions** – This occurs when the sample being purified has a large amount of surfactant like compounds (notably phospholipids). Having intermediate solubility in both phases, these compounds will form a milky mid-band between the two phases. This will prevent clean collection of either phase. Essentially, this renders LLE a less dependable method.
4. **Difficulty of automation** – Due to the large amount of solvents typically involved in successful runs of LLE, it is not easily compatible with

automated sample handlers. This implies that LLE procedures will have problems of user bias and low throughput.

4.2.3.2 The problem with phospholipids

In the context of lipidomics, it is important to discuss the limited selectivity of the LLE procedure in detail as this is perhaps the cause of the bottleneck in the sample preparation sub-domain. Before describing the problem in detail, it is necessary to take a look at the distribution of lipids in human serum

Table 4.1 Lipid distribution in the plasma (*from Quehenberger, Oswald et al, Journal of lipid research 51.11 (2010): 3299-3305.*)

Lipid Category	No. of species	Sum (mg/100 ml)
Fatty acyls		
Fatty Acids	31	5.82
Eicosanoids	76	0.002
Glycerolipids		
Triacylglycerols	18	90.6
1,2 – Diacylglycerols	28	2.36
1,3 – Diacylglycerols	27	0.805
Glycerophospholipids		
PE	38	32.7
PC	31	157
PS	20	0.559
PG	16	0.480
PA	15	0.173
PI	19	2.74
N – Acyl PS	2	0.001
Sphingolipids		
Sphingomyelins	101	22.817
Monohexosylceramides	56	0.180
Ceramides	41	0.732

Sphingoid Bases	6	0.02029
Sterol Lipids		
Free sterols	14	31.8
Esterified sterols	22	114
Prenol Lipids		
Dolichol	6	0.003
Coenzyme Q	2	0.394

It is hence clear that a massive chunk of the lipidome is made up of various subclasses of phospholipids. This heavily skewed distribution leads to prejudice in low molecular weight (LMW) metabolite coverage. Hence biological variations in the levels of these LMW metabolites get masked out by the overwhelming presence of phospholipids. In the absence of proper mobile phase, these phospholipids accumulate in the column, thereby accelerating its degradation. In addition, these accumulated species are slowly released in subsequent runs with other metabolites which leads to gradual increase in baseline noise levels, induction of matrix effects and alteration of separation characteristics. Phospholipids are also known to cause ion enhancement and suppression, which implies that the mass accuracy of co eluting metabolites are severely affected.

It is clear that LLE as a procedure will be of limited help in processing samples in such a way that selective lipid fractions are enriched and can be analyzed separately. All lipid species which are more soluble in organic solvents will be collected together and as described above, will cause a lot of problems both in experimental runs and in result analysis.

Due to these limitations imposed by the fundamental working principles of LLE, we will look at SPE as an alternative sample preparation strategy.

4.2.3.3 Solid Phase Extraction

Like LLE, SPE is also a sample preparation scheme for chromatography. The most common configuration is to have a solid-phase material (called solid phase extraction "resin") packed into a column between one or two frits. The liquid mixture which is desired to be purified is passed through this column. Due to chemical interactions between components in the mixture and SPE resin, some components will pass through and some will be retained. The bound components can be released or "eluted" by reversing the chemistry which led to their capture in the resin bed.

A pressure differential required to draw the liquid through the column can be generated by a small gas pressure on the top of the column or a vacuum at the base of it. Typically, a column would contain anywhere between 50 mg to 10 g of resin. Miniaturization is fairly straightforward with SPE. Due to this, SPE is particularly suited for situations where the volume of sample involved is very small.

4.2.3.4 Motivation

A number of materials have been explored for their possible application as an SPE. Hydrated silica[22], florisil[23], hydroxyapatite[24], hydrated metal oxides [25] (aluminum, magnesium, zirconium, titanium) as SPE resins for various domains have been reported in literature.[26-28]

Sample preparation is a bottleneck and unresolved problem in lipidomics research. The choice of sample preparation method is crucial to the observed

lipidomics profile and the quality of data collected.[29-31] In the absence of a well-defined and understood sample preparation protocol, accuracy of biological correlative interpretation of collected data can be irreversibly compromised. We want to separate the phospholipids which are over-represented by mass in the lipidome (the collection of all lipid species in the lipid extract) from the rest of the lipidome. The process of electron spray ionization (described in **section 2.7.2**) is a competitive phenomenon. The overwhelming presence of phospholipids in the lipid extract suppress the ionization of all other underrepresented lipid species. Hence, by removing the interfering class of lipids, phospholipids, it may be possible to discover more lipid species. The scheme is illustrated in the **figure 4.2.**

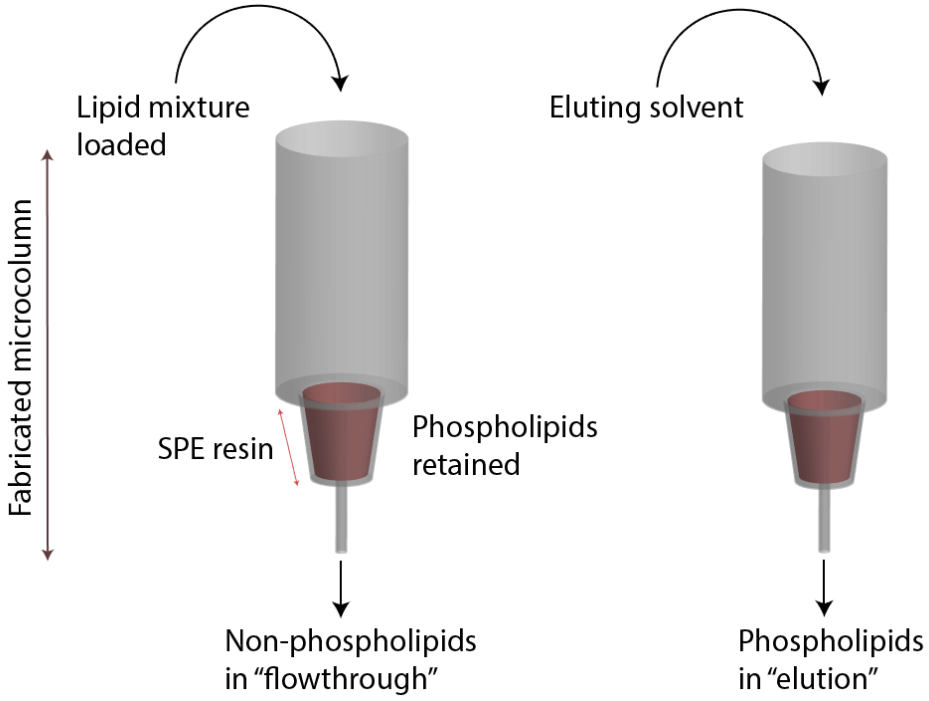

Figure 4.2 A schematic illustration of the concept of SPE applied to lipidomics

When the mixture of lipids is passed through such a column it separates the components into fractions. In other words, the two fractions are now "enriched"

because the interfering fraction has been removed. Hence, the name given to the process of separation is lipid fraction enrichment. Metal oxides are generally chemically resistant and abundant in the earth's crust which means there is a possibility of fabricating very cheap columns for lipid enrichment. We believe that there are 3 major criteria for a metal oxide to be chosen as an effective and commercially viable SPE resin.

1. **Stable and preferably non-toxic in ambient conditions** – some oxides like CoO and Cr_2O_3 are hygroscopic. On exposure to air, they will absorb moisture and make hydrated complexes. This renders them unusable in any column format. CrO_3 is carcinogenic making it a risky candidate to explore.
2. **High phospholipid capturing capacity** – The selected SPE resin must capture the highest amount of phospholipid per unit available surface area.
3. **Cheap** – If we can find such oxides which are abundant, there is a possibility of making extremely cheap, one time (or even multiple) use SPE cartridges packed with powders of said oxides.

The idea of selective phospholipid enrichment using TiO_2 was first proposed and demonstrated by Ikeguchi [32] and about 9 years later by Calvano [33]. Calvano actually demonstrated the possibility of removing phospholipids from dairy products and chocolate using TiO_2 columns. A more recent study [34] has shown the use of TiO_2 nanoparticles in analyzing the lipidome of olive oil and fruit.

To the best of our knowledge, there are no comparative studies in literature exploring the capturing capacities of different oxides under identical conditions so that chemistry of surface alone determines the capture amount. We seek to develop such protocols enabling accurate comparisons between various oxides so as to identify the best candidate for a cheap and specific SPE resin.

4.3 Results and discussion

The development of protocols and methods for accurately measuring phospholipid to transition metal oxides went through a few iterations before we could develop sensitive methods which enabled true quantification of adhesion to chosen surfaces.

4.3.1 Metal oxide coated MALDI plates for selective phospholipid enrichment

MALDI coupled to mass spectrometer (MALDI-MS) is a high throughput process for quickly testing the metal oxides we want to employ as SPE resins. We deposit stable thin films of metal oxides on commercially obtained MALDI target plates (made of stainless steel). The details of the deposition procedure can be found in the experimental **section 4.5.1**.

Previously, Calvano et al[33] have shown that TiO_2 films can capture phospholipids from lipid extract obtained from dairy products. We synthesized an artificial mixture of lipids using 2 phospholipids (DPMC and SM) and 3 non-phospholipids (GluCer, Cer 534, Cer 574) and tested the various oxide thin films for their performance in selectively capturing phospholipids. For clarity,

we have illustrated the workflow of the experiment in the **figure 4.3**. Experimental details have been provided in **section 4.5.2**.

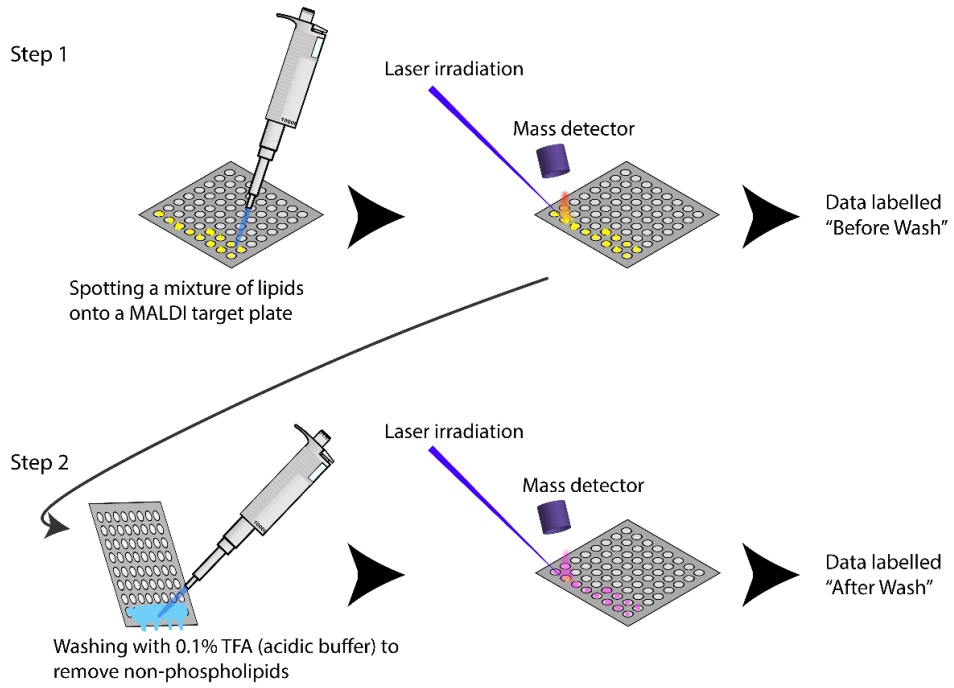

Figure 4.3 Schematic workflow of the experiment for testing metal oxide thin films as SPE resins in the MALDI format

The data depicting the comparison between various oxides is summarized in **figure 4.4**. In an ideal scenario, the before wash data should show all 5 lipid species which would reduce to 2 (only phospholipids) after being washed with a 0.1% TFA acidic buffer. In our experimental runs, we noticed that STO performed the best, selectively retaining the phospholipids while letting the ceramides be washed away. In some cases, such as LAO and Y_2O_3 the intensities of signal obtained before wash is actually smaller than the after wash signals. This is unexpected but can be explained by entering a short discussion about the intricacies of measuring lipid species through the MALDI-MS technique.

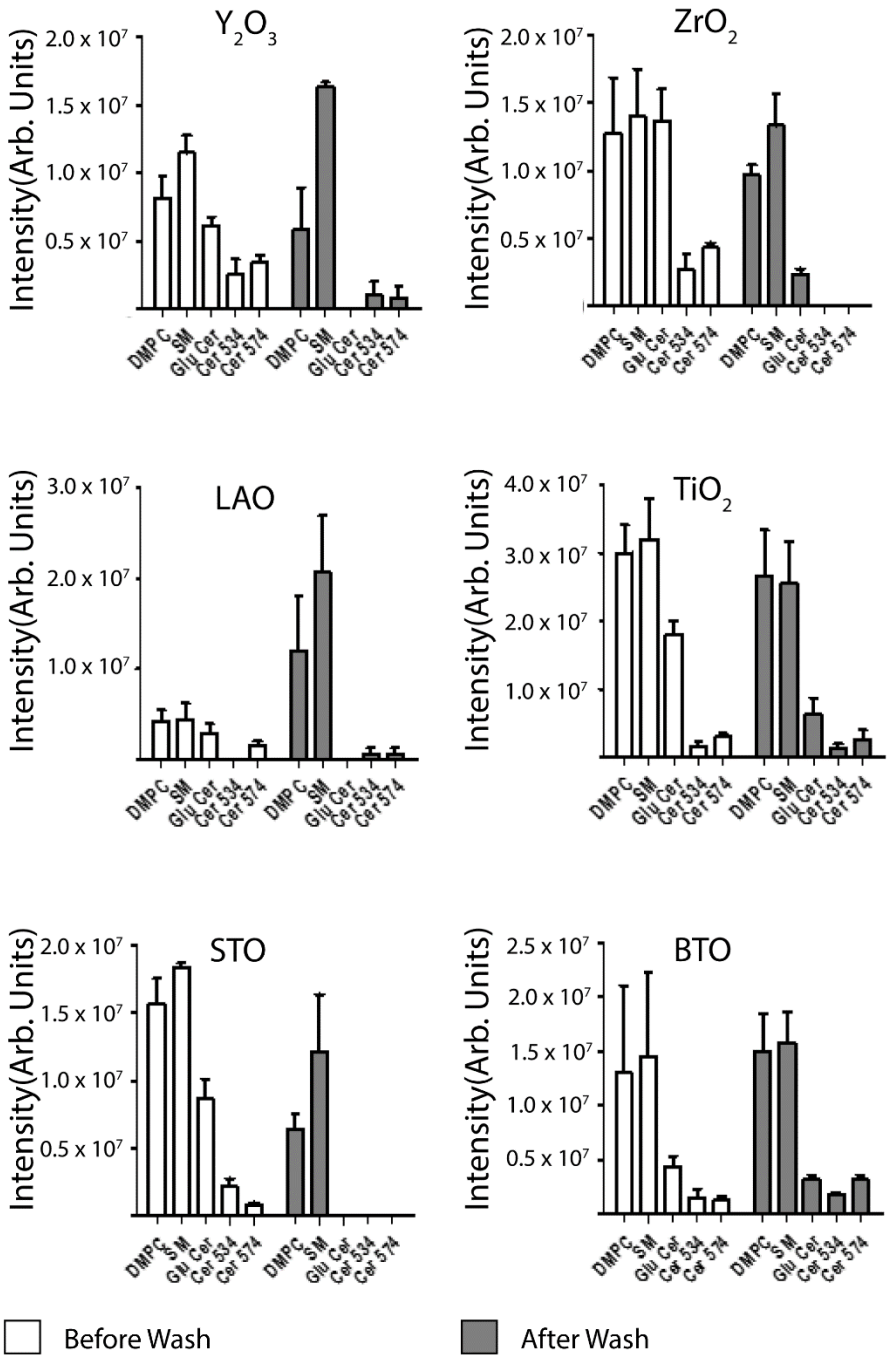

Figure 4.4 Comparison between 6 chosen transition metal oxides with respect to their selectivity of enrichment of phospholipids DMPC and SM. Ideally, after a wash of MeCN and 0.1% TFA, the nonphospholipid fractions GluCer, Cer 534, Cer 574 should get removed from the plate leaving only DMPC and SM.

First of all, the nature of the surfaces is such that the mixture of lipids tends to spread instead of staying in the marked out circles (from where the MALDI setup will read the signal). Secondly, the same is true for the ClCCA + 2,5 DHB matrix used to couple the energy of the laser to the compounds under investigation in order to ionize them. Consequently, the crystallization of the matrix is not uniform which in turn affects the readings obtained.

Due to the aforementioned reasons, the error between runs of the experiment was significant. It is therefore, important, to move the protocol in a direction which would make data more reproducible.

4.3.2 Phospholipid enrichment using µcolumns

MALDI is of course the method of choice when the most important parameter of the experiment in question is its ease and speed of operation. However, the more realistic scenario in which these metal oxide powders will get deployed in, is columns. Hence the next iteration of seeking to study phospholipid binding to metal oxides involved fabrication of µcolumns. The process of fabrication is described in detail in **section 4.5.3**. The experiment itself consists of a large number of steps, all of which have been set out in detail in the same section, **4.5.3**.

There are a few issues that need attention when fabricating these µcolumns. We are using a suspension of metal oxide powders made in acetone to pack the µcolumn with these metal oxide powders. Since the amount of powder that can be packed within a small µcolumn is extremely small, there is probably significant differences in the actual weight of powders successfully packed into

the µcolumn. Commonly available microbalances can't measure these weights reliably.

It is nearly impossible to fabricate working µcolumns with very fine powders. All the powders were commercially procured and they had large size dispersions. The SEM images of the powders are shown in **figure 4.5.** BTO, Sc_2O_3 and NiO powders had extremely small particles measuring few tens of nanometers. The particles pack so tightly together that it becomes impossible to push the liquid sample through them. The back pressure generated by the tight packing of these powders is so high that is most cases, applying a higher pressure to overcome it would lead to rupture of the column as such. Through repeated experiments we have found that for designing µcolumns with a packed bed of powders, the particle size has to be larger than 200 nm at the very least. The particle size of Y_2O_3 powders was about 200 nm and we managed to fabricate working µcolumns of the same with great difficulty.

We chose 4 oxides, STO, Y_2O_3, ZrO_2 and TiO_2 for testing relative efficiencies in selective capture of phospholipids from an artificial lipid mixture. The details of the lipid mixture can be looked up in **section 4.5.3**. Briefly, we used a mixture of 2 phospholipids (DMPC and SM) and two non-phospholipids (GluCer and Cer 17). Ideally the flowthrough component should have only GluCer and Cer 17. The elution component must have only DMPC and SM. We use an acidic buffer to load the lipid samples into the µcolumns thereby promoting phospholipid adhesion. Thereafter we use a basic buffer to elute the bound phospholipids. The results are shown in **figure 4.6.**

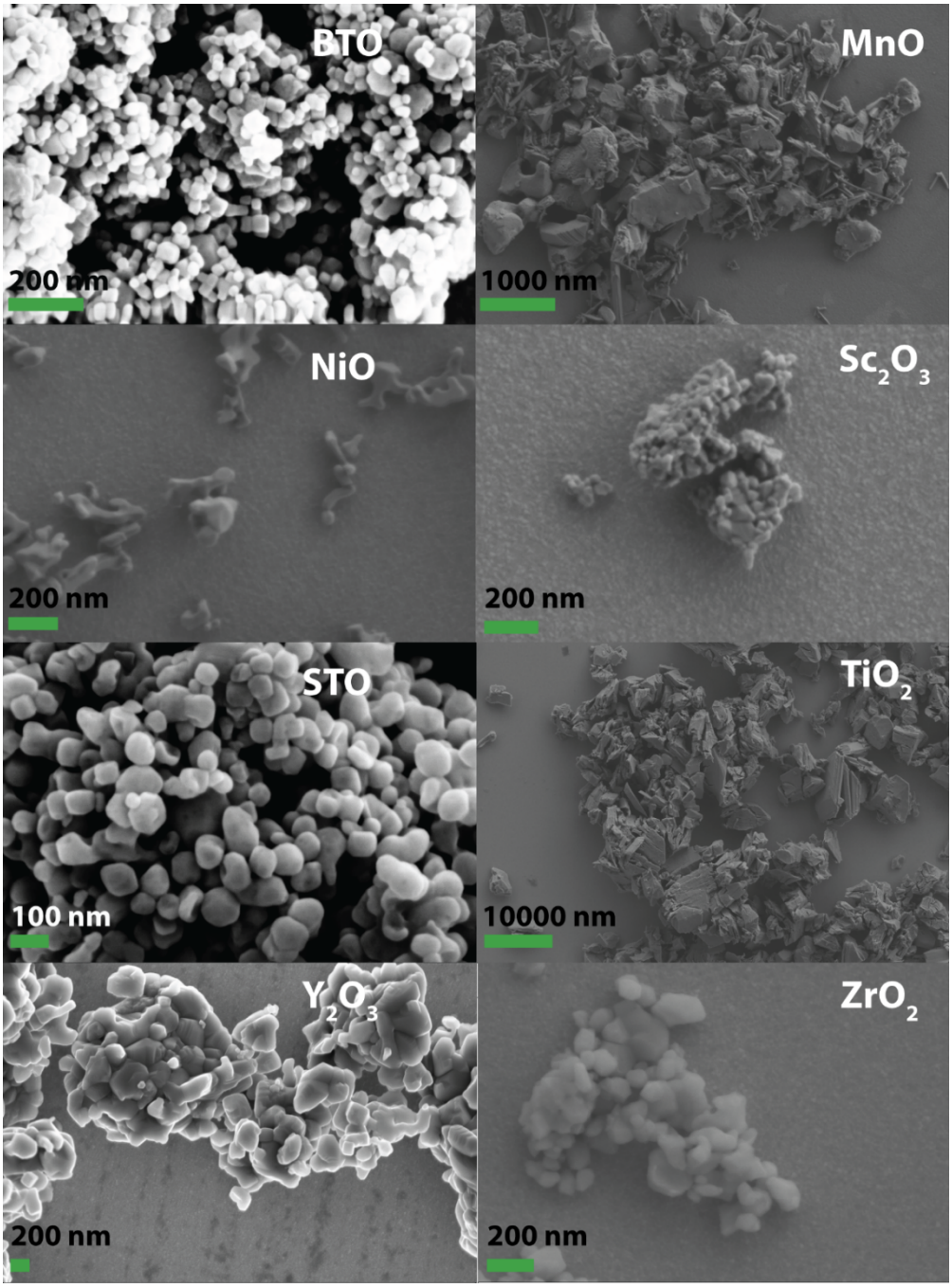

Figure 4.5 SEM images of powders showing the large difference in particle sizes. Scale bars are shown in green.

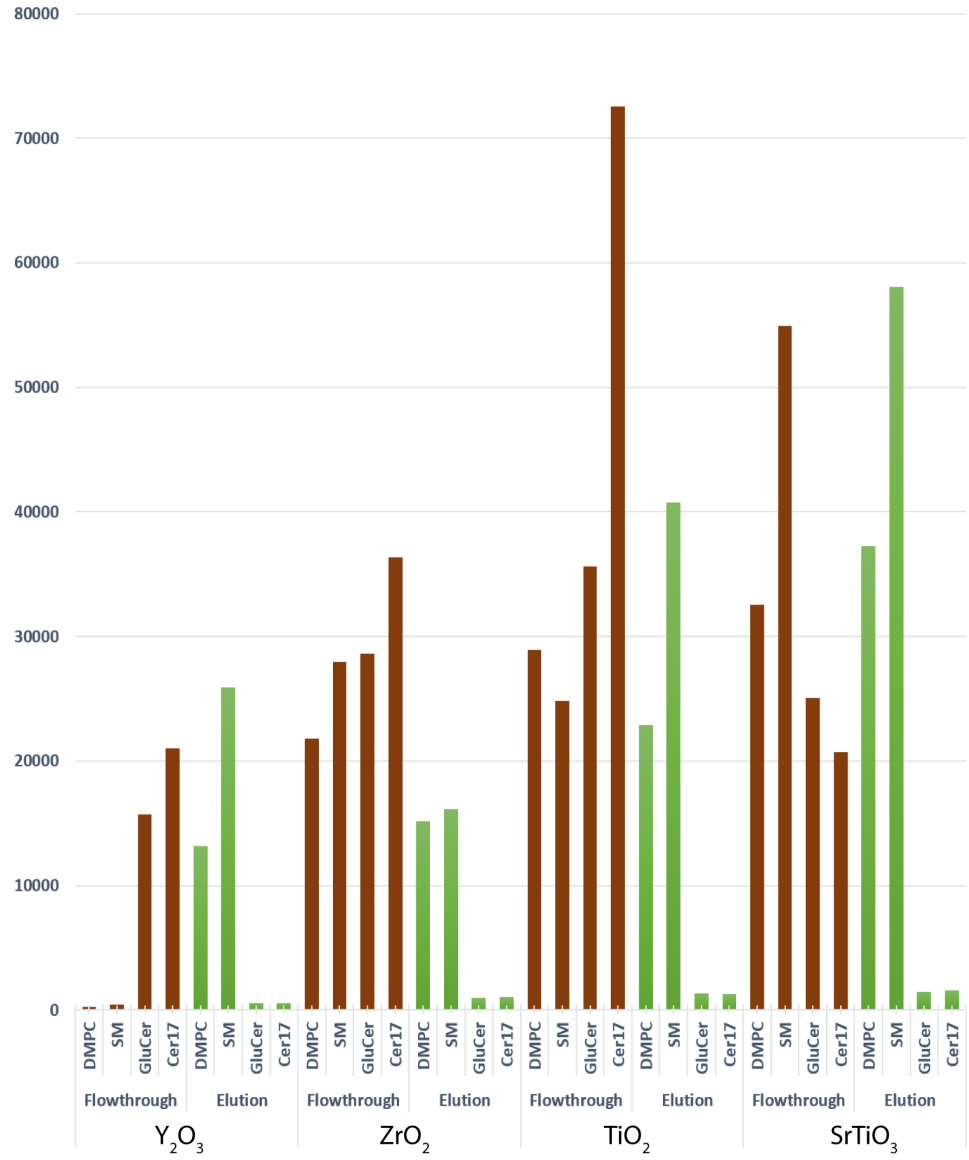

Figure 4.6 Comparison between 4 oxides with respect to selective phospholipid enrichment. (Brown denotes flowthrough component, which should ideally have only GluCer and Cer 17; green denotes the elution component which should have only DMPC and SM. Y Axis is in arbitrary signal strength units.

As we can readily see, Y_2O_3 seemed to be the cleanest and most effective SPE resin which was extremely selective in capturing the phospholipids from the mixture and eluting them under the flow of basic buffer through the µcolumn. All other columns showed phospholipids in flowthrough component. This is

known as “breakthrough” in the field of chromatography. “Breakthrough” happens when the maximum binding capacity of a column is exceeded.

It has to be pointed out that for the purposes of testing materials for SPE resins, we are using an artificial mixture of lipids in which phospholipids are present in a concentration about $1/10^{th}$ of non-phospholipids. In actual lipid extracts, phospholipids are the dominant entity. The idea is to demonstrate that these SPE resins made from metal oxide powders can actually selectively capture phospholipids even when they are in a mixture where the major component is the non-phosholipid fraction.

Additionally, there are two factors which are not controlled in this setup

1. **Flow rate through the column** – This translates into the actual time the lipid species spend in contact with the metal oxide powders. Since manual pressure is used through a syringe and the powders vary a lot in their particle size, the flow rate of the liquid mixture through the packed bed of the column is different in each case.
2. **Surface area in contact with lipid species** – Owing to large differences in particle size and shapes of metal oxide powders, the actual surface area which is in contact with and can be used for enrichment of phospholipids is different.

4.3.3 Phospholipid enrichment using batch processing

After identifying the major problem in fabricating and working with µcolumns packed with fine powders, we decided to test the various powders in a scheme which did not involve µcolumns. This approach is called batch processing. The details about the design of the experiment can be found in the **section 4.5.4**. Through this approach, we have managed to ensure that the phospholipids spend the same amount of time in contact with the metal oxide powders. We also devised a parameter α which represents the ability of a particular metal oxide to act as a SPE resin. The details about the evaluation of α is schematically shown in **figure 4.7**.

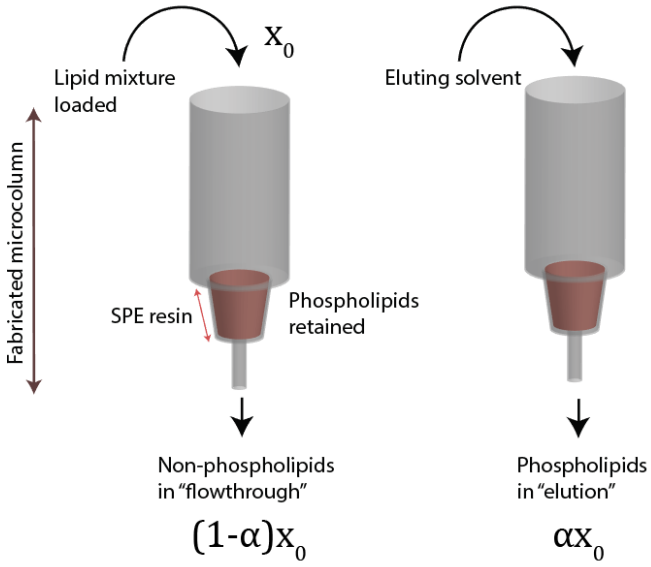

$$D = \frac{Elution}{Flowthrough}$$

$$D = \frac{\alpha x_0}{(1-\alpha)x_0}$$

$$\alpha = \frac{D}{D+1}$$

Figure 4.7 Evaluation of α used to compare between various metal oxides. x_0 is the number of molecules in the original mixture. αx_0 denotes the number of molecules captured by the column. $(1-\alpha)x_0$ molecules are not able to find capture sites on the SPE resin and are present in the flowthrough. D is obtained by dividing peak intensities of flowthrough and elution as obtained through ESI-MS. α will be 1 for a perfect SPE and 0 for a material which has no affinity for phospholipids.

The parameter α was evaluated for the phospholipid DMPC from a mixture of DMPC, SM, Glu Cer and Cer. When the experiment was performed for transition metal oxides from the 3d period, the broad trend could be studied. **Figure 4.8** represents the variation of α in different oxides.

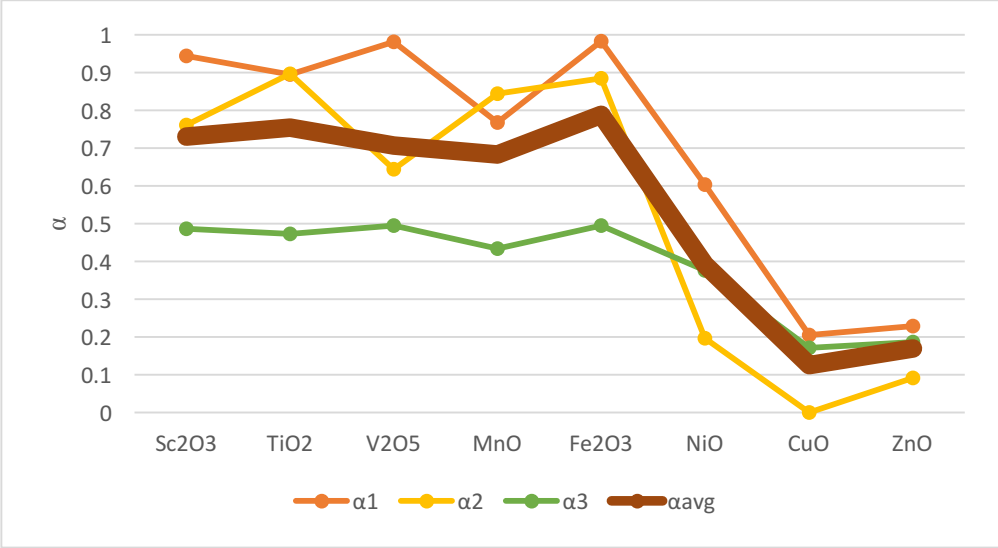

Figure 4.8 α as obtained for all stable 3d transition metal oxides

We can observe that α is around 0.7 for Sc_2O_3, V_2O_5, TiO_2, MnO and 0.8 for Fe_2O_3. NiO has an α of 0.4 while CuO and ZnO have 0.15 and 0.2 respectively. Hence it becomes immediately clear that for fabricating columns for phospholipid enrichment, usage of NiO, CuO or ZnO is futile.

Again, for the purposes of testing, we are using an artificial standard mixture where the non-phospholipid fraction is present in a ten-fold higher concentration compared to the phospholipid fraction. We want to be able to show that metal oxides can indeed work even in conditions biased heavily against selective capture of phospholipids.

Interestingly, we noted that Sc_2O_3, V_2O_5, TiO_2, MnO and Fe_2O_3 are all d^0 systems while NiO is d^8, CuO is d^9 and ZnO is d^{10}. Therefore, d^0 systems prefer the adhesion of phospholipids and the adhesion is dramatically less for oxides where the d orbitals are filled with electrons. We can, hence, claim that with respect to choice of material for lipid fraction enrichment, one must try and

choose metal oxides which have a large number of empty (if not completely empty) d orbitals.

Cr_2O_3 and CoO were not included in this study despite belonging to the 3d group because of their hygroscopic nature.

However, as seen from the plot, the spread in as-obtained α values about the mean was very significant. The standard deviation hovered around 30% of the mean value in most cases. Although moving to this scheme of testing SPE resins from the previous μcolumn based approach enabled us to control the time spent by lipid species in contact with the powder, there were still two crucial factors causing a sizeable spread across numerous runs of the same experiment.

1. **Large number of manual steps** – this introduces user dependent artefacts and increases the possibility of errors
2. **No control over surface area of particles** – again, as with the μcolumn approach, the actual surface area of the particles acting as SPE resin for phospholipids is different for various oxides and also amongst different runs of the same oxide.

4.3.4 Surface Plasmon Resonance for quantifying phospholipid adhesion

Due to the lack of control over certain parameters as shown above, we decided to fabricate special chips which would enable us to measure accurately the amount of phospholipid molecules stuck to a thin film of metal oxide. The

process of fabricating these chips has been described in detail in the **section 4.5.5**. There are a number of issues which need to be carefully addressed in the fabrication of these chips. These have been discussed in detail in **section 2.5.4.**

The objective behind moving to SPR setup for measuring phospholipid adhesion to metal oxide surfaces was the higher degree of control over experimental parameters and the possibility of minimizing errors inherent in manual steps.

1. Flow was controlled through a peristaltic pump having same fluid flow rate for every metal oxide chip
2. Surface area of SPE resin in contact with the phospholipid is the same for all samples

Now when these two parameters have been brought under our control, we are in a position to compare the various metal oxides through the surface plasmon resonance technique. Actual data obtained on a chip with a 3 nm film of TiO_2 is shown in **figure 4.9** for the purpose of illustration of the concept. We can visualize every event in real time because of the nature of the experiment, unlike all other previous approaches where only the initial and final condition of the sample are known through readouts from the mass spectrometry step.

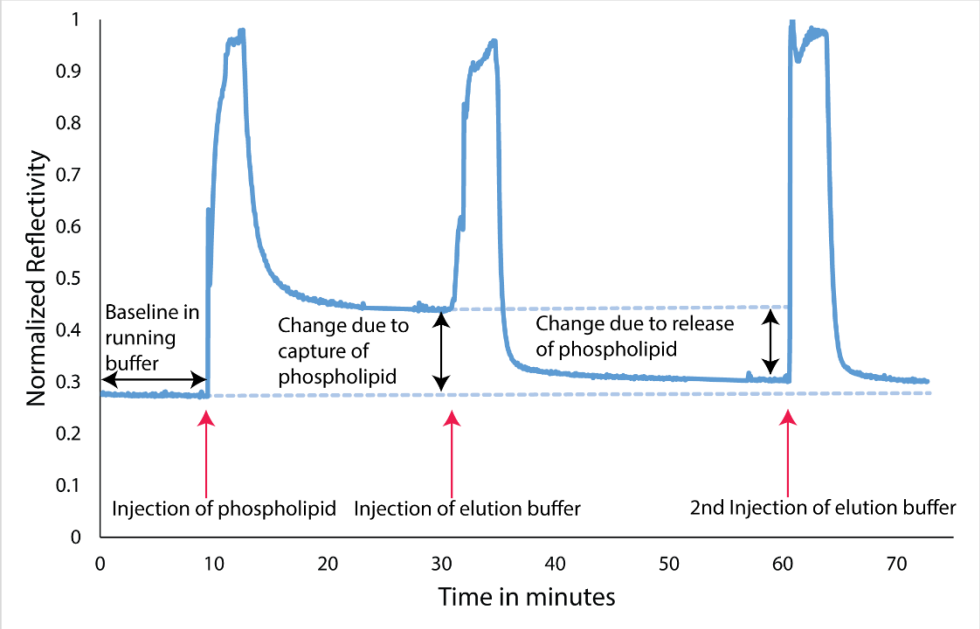

Figure 4.9 The capture and release of the phospholipid DMPC from a 3 nm film of TiO2 observed through surface plasmon resonance. Various events have been marked on the plot

In **figure 4.10**, we show the shift of the resonance angle. The shift of the angle to the right on the binding of phospholipid and thereafter to the left on the unbinding is clearly seen. WINSPALL software package is used to fit the curves acquired experimentally. Using data from these simulated curves, the precise mass captured on the surface of the thin film is estimated. Data is shown for a film of TiO_2.

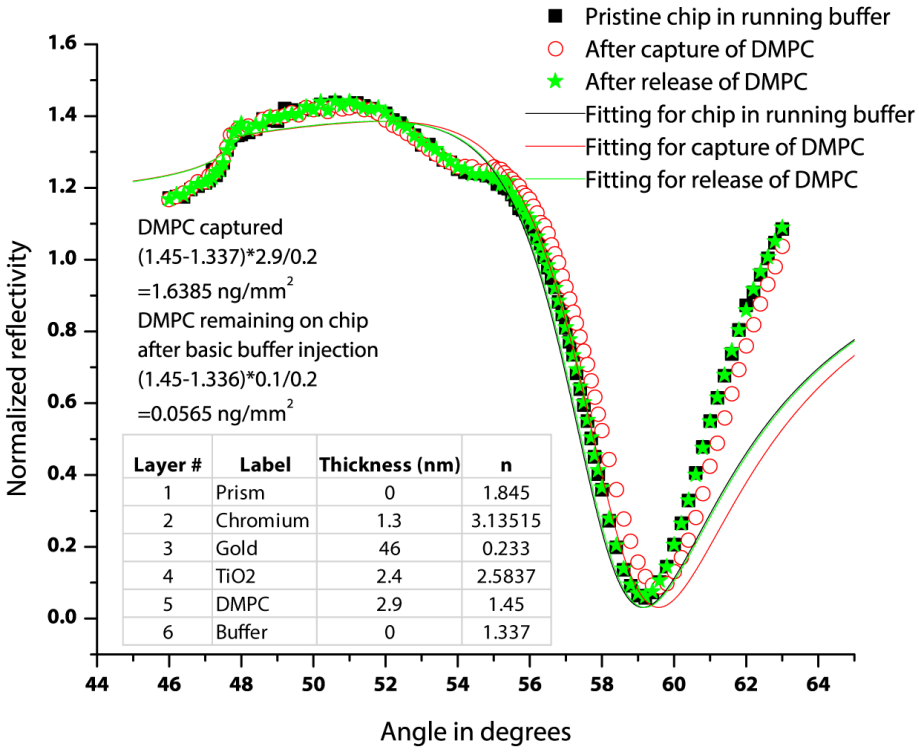

Figure 4.10 Angular spectrum showing shifts in resonant dips upon binding and unbinding DMPC. The actual and fitted data is shown. The estimation of mass on the TiO2 surface is derived and displayed in the inset. n is refractive index. Details of calculation can be found in section 4.5.5.

The extreme sensitivity of the SPR technique was found to be very useful not only in detecting phospholipid binding to the oxide surfaces but also in detecting etching away of the metal oxides themselves under the acidic buffer used to promote the capture of DMPC. When acids etch away at metal oxides, they form salts. The presence of salts are very detrimental to the system health of modern day sophisticated and precise mass spectrometry setups. The other serious problem is that salts cause ionization suppression [35, 36] and hence will lead to erroneous results. It is impossible to monitor the loss of metal oxides from µcolumns as salts because the change in mass is minuscule. However, with the SPR approach, the process can be easily detected. We show an example in

figure 4.11 where the film of CuO is being etched by the 0.1% TFA acidic buffer used to inject DMPC.

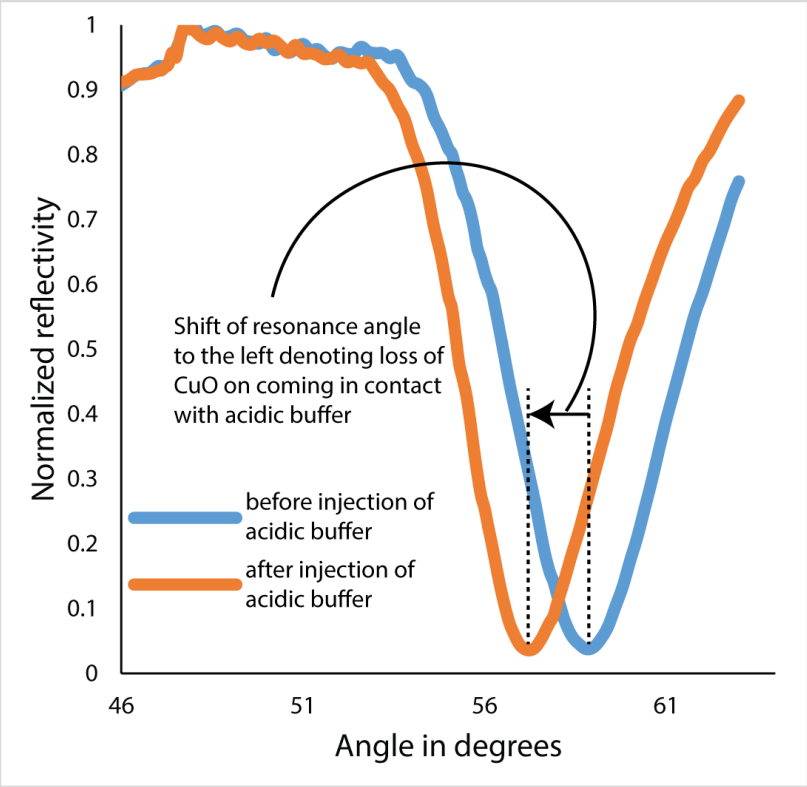

Figure 4.11 Angular spectrum showing the etching of CuO film when it comes in contact with the 0.1% TFA (acidic buffer) used to inject the phospholipid DMPC into the setup.

We found that Sc_2O_3, V_2O_5, CuO and ZnO, having considerable basic character, will form salts and get etched out. Hence we obtained mean phospholipid capturing capacity for TiO_2, Fe_2O_3 and NiO. In line with our discussion in **section 4.2.3.4**, we have collated all the information in the **table 4.2.**

Table 4.2 Selection of a SPE resin amongst 3d oxides evaluating all of them on parameters discussed in the motivation section 4.2.3.4. (Costs taken from Sigma-Aldrich, Singapore website)

Label	Environmentally stable	Forms salts easily in contact with acidic buffer	Phospholipid captured (ng/mm^2)	Cost in SGD (for 5g of 99.999% purity)
Sc_2O_3	Yes	Yes	N.A.	
TiO_2	Yes	No	1.6415±0.2344	182.50
V_2O_5	Yes	Yes	N.A.	
Cr_2O_3	No	N.A.	N.A.	
MnO	Yes	Yes	N.A.	
Fe_2O_3	Yes	No	1.6520±0.4652	158.50
CoO	No	N.A.	N.A.	
NiO	Yes	No	0.6650±0.3820	109.00
CuO	Yes	Yes	N.A.	
ZnO	Yes	Yes	N.A.	

Hence, from the data we find that both TiO_2 and Fe_2O_3 can be very good choices for being SPE resins in sample preparation for lipidomics. Let us consider our best performer Fe_2O_3. We injected 20 µl of 1mg/ml lipid sample. Hence, we have injected 20 µg. 1.65 ng is captured per sq. mm. The area in contact is about 10 mm^2. Therefore we have captured 16.5 ng which is 0.0825%. However, we have to remember this is a flat surface.

Let us put these numbers into perspective. Assuming we have powder of Fe_2O_3 with particle radius of 100 nm, 1 mm^2 is the combined available surface area of

about 8 x 10^6 particles. Just 1 mg of Fe_2O_3 powder of the same particle radius would contain about 5 x 10^{14} particles – a very attractive proposition indeed!

We then tested the effect of the headgroup on the adhesion of phospholipids to a TiO_2 film. The results are shown in **figure 4.12.** Unlike the previous set of SPR experiments, this experiment was performed on a commercial GE Biacore SPR setup. Reflectivity changes are represented in response units (RU) in commercial SPR systems. Upon looking at adhesion of 4 phospholipids (each with a different number of phosphate groups) to the TiO_2 film, we found that PI and PIP, with 1 and 2 phosphate groups respectively, adhere in almost similar quantities to the surface. However, PIP_2 with 3 phosphate groups and PIP_3 with 4 phosphate groups have almost 20 and 40 times the adhesion respectively. Same concentrations of all lipids were used. We postulate that the high adhesion shown by PIP_2 and PIP_3 is a cumulative effect of two factors. Since phospholipids bind to TiO_2 through the phosphate group, more phosphate groups on a phospholipid molecule would mean more affinity for TiO_2. Moreover, as the affinity is higher, the molecules would probably arrange into such assemblies which shadow less of the TiO_2, leaving more of the film exposed for capturing more phospholipid molecules. We can speculate that for PI and PIP, the lipid molecule lies flat on the surface, in the process causing a shadowing of a significant area of TiO_2 by the carbon backbone of the molecule. However for PIP_2 and PIP_3, Only the inositol rings remain on the surface, pinned to the film by the phosphate groups. The hydrocarbon tail shoots out and away from the surface, casting no shadow and making more TiO_2 area available for further binding events.

It was also found that the basic buffer used to unbind PI and PIP, could not elute PIP_2 and PIP_3 because of their strong adhesion to TiO_2. This points to the possibility of developing a sequential elution protocol, where basic buffers of increasing strength are used to sequentially elute phospholipids beginning with ones which have low adhesion and ending in ones which have highest adhesion.

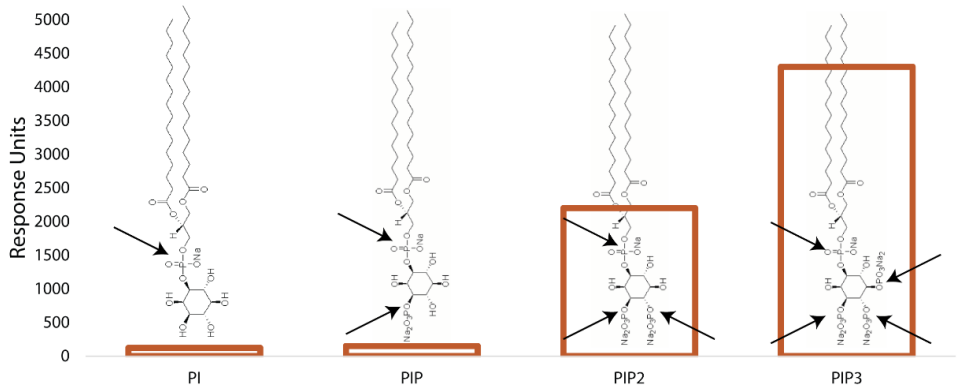

Figure 4.12 Differences in adhesion based on number of phosphate groups. Phosphate groups have been marked with black arrow.

4.3.5 Planar columns on MALDI plates for on target enrichment

We also explored the possibility of performing what is known in modern chromatography as "on target enrichment" [37] using metal oxides. A schematic illustration of the experiment is given in **figure 4.13**. An 80 mm x 1 mm thin film (250 nm) of TiO_2 was deposited using the PLD technique on a commercially procured AbSciex MALDI target plate. The details can be found in the **section 4.5.6**. It was found that phospholipids (LPC, PC and SM) migrate over a distance of about 3 cm from the point of being spotted. Non-phospholipids that were spotted in the same mixture could not be found. The results from the MALDI scan at 3 cm away from original spot is shown in **figure**

4.14. Scans for other spots can be found in the **appendix section A-2.** They show very narrow distribution where the phospholipids localize on the strip.

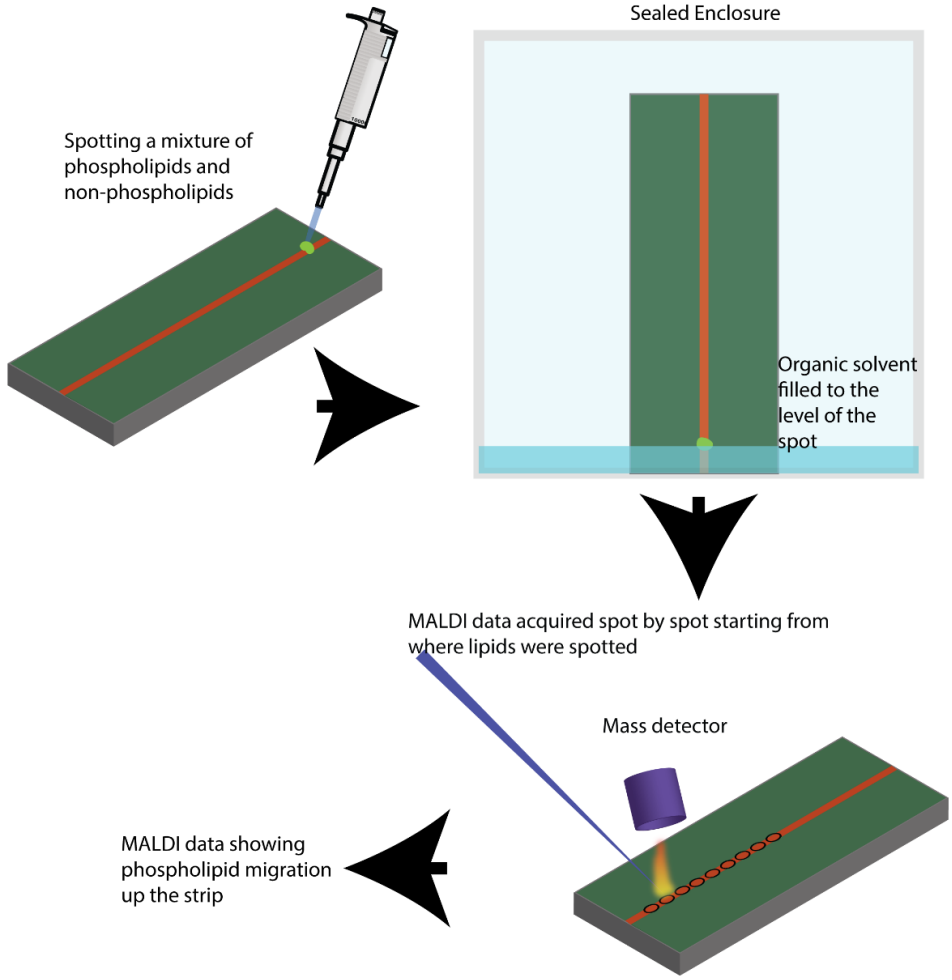

Figure 4.13 Schematic illustration of the design of the experiment showing how the data is acquired. Green colour denotes stainless steel. Orange denoted the deposited film of TiO_2.

Thin layer chromatography (TLC), described in section 2.8.1 is eerily similar with one crucial difference. The mixture to be separated moves up along the paper or the material meant to act as the separating medium by capillary action. Capillary action is easily explained in porous materials like paper and chalk. In our case, neither the MALDI target plat, nor the deposited thin film is porous. Hence we can't explain capillary action as the driving force of this separation.

We hypothesize from the insights gained from **sections 4.3.1-4.3.4** that this distance will change based on the oxide used. Hence, the migration distance is tunable by choice of material. Additionally, since adhesion to metal oxides is highly dependent on the number of phosphate groups, it might be possible that phospholipids with same number of phosphate groups will migrate to the same distance. We found that LPC, PC and SM, all of which have one phosphate group migrated the same distance. We hypothesize, this kind of planar columns of metal oxides can sort phospholipids by number of phosphate groups on a MALDI plate based on the migration distance.

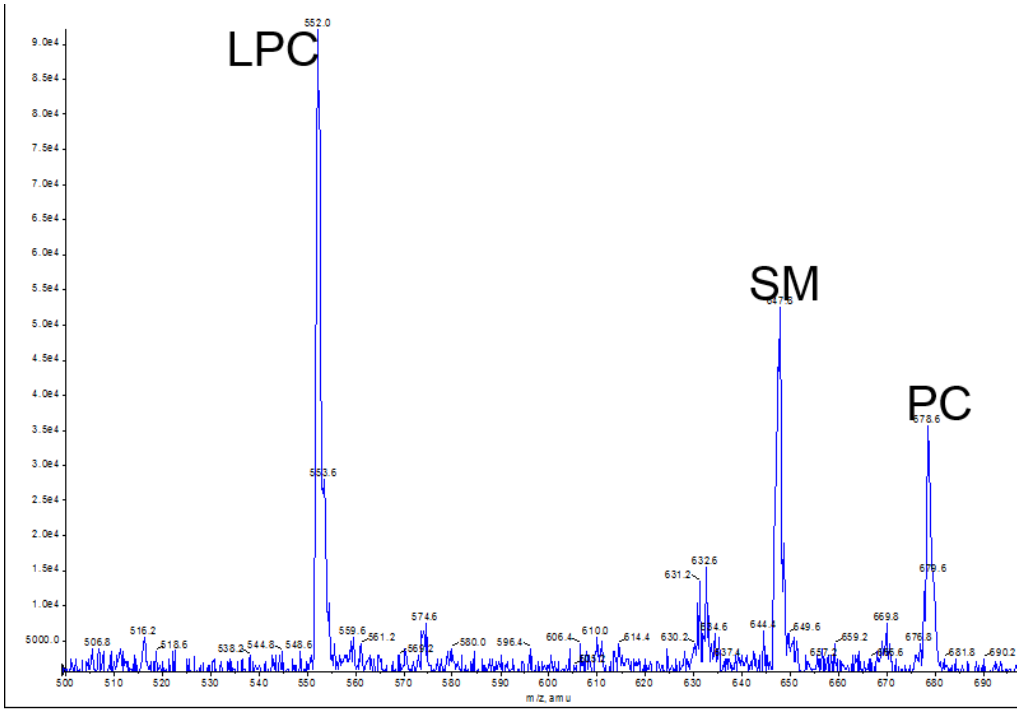

Figure 4.14 MALDI-MS data at a point 3 cm away from the spotting point. Only phospholipids LPC, SM and PC were found. Non-phospholipids were not found on the strip.

4.4 Conclusion

We have demonstrated that metal oxides can indeed act as efficient SPE resins in sample preparation for lipidomics. It will not be an overstatement to state that these SPE resins can also be applied to phosphopeptide enrichment. The SPR based technique to accurately quantify phospholipid adhesion has made it possible to compare between various suitable metal oxides and obtain reproducible data dependent only upon the chemistry of interaction. This method can also be used to test the effect of the headgroup upon its affinity for metal oxide surfaces. A summarizing table containing a simple comparison of the various protocols used to measure phospholipid adhesion

Table 4.3 Comparison of various methods of evaluating phospholipid adhesion to SPE resins

Name of method	Control over contact area	Control over contact time	Detection of resin etching	Precise determination of lipid species captured	Compatible with existing mass spectrometry workflow
MALDI	Yes	No	No	No	Yes
µcolumn	No	No	No	No	Yes
Batch processing	No	Yes	No	No	Yes
SPR	Yes	Yes	Yes	Yes	No

We have also shown the possibility of applying the knowledge gained through this experiments towards designing separation devices in two formats - µcolumns and planar columns for on target enrichment.

In the next chapter, we will study proteins, a class of biomolecules much larger and complex than lipids. Having used the SPR technique to study lipid interactions with fabricated surfaces, we apply an advanced form of SPR towards quantifying protein interactions with inorganic surfaces.

4.5 Experimental details

4.5.1 Fabrication of modified MALDI plates

Metal oxide thin films were deposited on the commercially obtained MALDI plates from AbSciex. A Neocera 4 inch PLD (Pulsed laser deposition) system was used for this purpose. The standard MALDI plate is 12 cm x 8 cm in size. Hence it was cut into 3 equal pieces 4 cm x 8 cm each. After the cut was made, the plates were cleaned by sonicating them for 10 minutes in acetone, methanol and DI water successively and in that order. A 248 nm KrF excimer laser was used to deposit films of TiO_2, ZrO_2, Y_2O_3, $LaAlO_3$ (LAO), $SrTiO_3$ (STO), $BaTiO_3$ (BTO). Identical conditions for used for the growth of all the oxides: room temperature, oxygen pressure 3.00 mTorr, laser frequency 10 Hz, 40000 shots. Film thicknesses were in the range of 240 to 290 nm.

4.5.2 Lipid adhesion studies with modified MALDI plates

The following lipids were procured commercially from Avanti Polar Lipids (Alabaster, AL, USA)

1. 1,2-dimyristoyl-sn-glycero-3-phosphocholine (DMPC)
2. N-lauroyl-D-erythro-sphingosylphosphorylcholine (SM)
3. D-glucosyl-ß-1,1'-N-octanoyl-D-erythro-sphingosine (GluCer)
4. N-octanoyl-D-erythro-sphingosine (Cer 534)
5. N-heptadecanoyl-D-erythro-sphingosine (Cer 574)

The steps are outlined below.

- Make up a standard mixture of 1mg/mL of each lipids in methanol consisting of DMPC, SM, GluCer, Cer 534 and Cer 574

- Dilute the standard mixture to 50µg/mL with Methanol:H_2O 70:30
- Spot 0.5µL of the standard mixture in 3 replicates and dry
- Wash with 200µL of MeCN+0.1%TFA (trifluoroacetic acid) on the spots thrice
- Dry the spots and spot 0.5µL of the CLCCA (4-Chloro-α-cyanocinnamic acid) +2,5DHB (Dihydroxybenzoic Acid) matrix onto the spots and dry
- For control, 0.5µL of the standard mixture in 3 replicates were spot and dry, followed by 0.5µL of the CLCCA +2,5DHB matrix onto the spots and dry. These are the spots without wash.

4.5.3 Lipid adhesion studies with µcolumn approach

The detailed procedure for the µcolumn setup is given below

- Make up a standard mixture of 1mg/mL of each lipids in methanol consisting of DMPC, SM, GluCer, Cer
- Dilute the standard mixture to 50µg/mL with Methanol:H_2O 70:30
- Suspend 30 mg of metal oxide powder in 1 ml of acetone. Sonicate for 5 minutes. Centrifuge the suspension for 14000 RPM for 10 minutes. Discard the supernatant and pipette in 1 ml of fresh acetone. Repeat the process three times. Finally pipette in 1 ml of acetone and sonicate for 5 minutes. This becomes the suspension used to pack metal oxide powders in the µcolumn.
- Take a 10µL pipette tip and block the narrow end of it using a stamped out piece of 3M Empore C8 disk.
- Take 100µL of the suspension and inject it into the pipette tip. Use a syringe to push out the excess acetone. This is the modified µcolumn.
- Equilibrate the µColumn with 20µL of loading buffer (Ethanol + 0.1% TFA) for 5 times

- Load 3µL of stardard mixture (50µg/mL) with 17µL of loading buffer. Push the syringe and collect this as flow through
- Wash the µColumn with 20µL of loading buffer for 5 times and collect this in the same tube as flow through
- Elute the bound lipids with 20µL of elution buffer [Methanol:chloroform:TEA (Triethylamine) (45:45:10)] for 6 times and collect these as elute
- Dry the samples in Speed Vac for 30 minutes
- Resuspend the dried samples in 10µL of methanol:chloroform (1:1)
- Analyse the samples in Flash Quant

4.5.4 Lipid adhesion studies in batch processing approach

The procedure is described below

- Prepare a 1 ml standard mixture of lipids by mixing lipid standards of DMPC, SM, GluCer and Cer 17. The final concentrations of these four lipids will be 0.05 mg/ml, 0.05 mg/ml, 0.4 mg/ml and 0.4 mg/ml respectively.
- Suspend 30 mg of metal oxide powder in 1 ml of ethanol. Sonicate for 5 minutes. Centrifuge the suspension for 14000 RPM for 10 minutes. Discard the supernatant and pipette in 1 ml of fresh ethanol. Repeat the process three times. Finally pipette in 1 ml of ethanol and sonicate for 5 minutes. This becomes the stock suspension.
- Take 60 µL of stock suspension, centrifuge at 14000 RPM for 10 minutes and discard the ethanol. Pipette in 200 µL 0.1% TFA solution in ethanol and sonicate.
- Add 1 µL of standard mixture and shake for 5 minutes.

- Centrifuge at 14000 RPM for 10 minutes and collect the supernatant. Label it “flowthrough.”
- Add 200 µL of 0.1% TFA and shake for 5 minutes. Centrifuge at 14000 RPM for 10 minutes and collect supernatant. Add it to the flowthrough collected from previous step. Repeat twice.
- Add 200 µL of basic elution buffer [Methanol:chloroform:TEA (Triethylamine) (45:45:10)]. Shake for 5 minutes. Centrifuge at 14000 RPM for 10 minutes and collect the supernatant. Label it “elution.”
- Add 200 µL of basic elution buffer [Methanol:chloroform:TEA (Triethylamine) (45:45:10)] and shake for 5 minutes. Centrifuge at 14000 RPM for 10 minutes and collect supernatant. Add it to the elution collected from previous step. Repeat twice.
- Dry in speed vac for 30 mins and resuspend in in 60% water, 40% acetonitrile, 10mM ammonium formate.
- Analyse samples in ESI-MS.

4.5.5 Surface plasmon resonance

The chips were fabricated using the PLD technique. The growth conditions were 300°C temperature, oxygen pressure 3.00 mTorr, laser frequency 1 Hz. The uniformity of the film over the 10 mm x 10 mm area and the elemental composition was checked and the thicknesses were calibrated using RBS. Finally, 3 nm thin films of oxides were deposited on the gold chip.

The running buffer was 10% ethanol. The acidic buffer was 0.1% TFA in 70% ethanol. DMPC was dissolved in the acidic buffer to a concentration of 0.2 mg/ml. The basic eluting buffer is 0.1 N NH_4OH in 70% ethanol. DMPC was injected in the following condition: 160 µl of 0.1% TFA in 70% ethanol was added to 40 µl of 1 mg/ml DMPC. The flow rate was 1 µl/s or 60 µl/min. At

this high flow rate, the interaction is not limited by mass transfer. The injection time for both DMPC and the basic eluting buffer is 180 secs.

After the data is obtained, WINSPALL software package is used to fit the curves in order to find the change in refractive index ($\Delta n = n_{\text{after binding}} - n_{\text{before binding}}$) and the thickness (d) of the captured layer of phospholipids. The mass on the surface of an oxide thin film is calculated by the following formula.

$$Total\ mass = \Delta n \times \frac{d}{\frac{\partial n}{\partial C}}$$

Δn and d are obtained from the fitting curve. The quantity $\frac{\partial n}{\partial C}$ is change in refractive index per unit change in concentration and is taken to be 0.2 for all proteins, lipids and polymer systems.

4.5.6 On target enrichment

The MALDI target plate is modified by depositing a thin film of TiO_2 as shown in the figure below. The plate is cleaned by sonicating for 10 minutes in acetone, methanol and DI water successively and in that order. A 248 nm KrF excimer laser was used to deposit the films of TiO_2. A schematic is shown in the **figure 4.15.** The conditions for the deposition are: 300°C temperature, oxygen pressure 3.00 mTorr, laser frequency 10 Hz, 40000 shots.

The procedure for the experiment is given below

- Spot 0.5 μL of lipid standards (mixture of LPC, SM, PC, GluCer and Cer) at a chosen point on the strip.
- Dry the sample
- Place it in a glass beaker with an air tight lid
- Pipette in enough of elution buffer [MeOH:$CHCl_3$:TEA (45:45:10)] so that the solvent just touches the spot

- Put lid on and leave overnight
- Remove sample from container and let it dry
- Spot CLCCA +2,5DHB matrix over the strip
- Analyse in Flash Quant

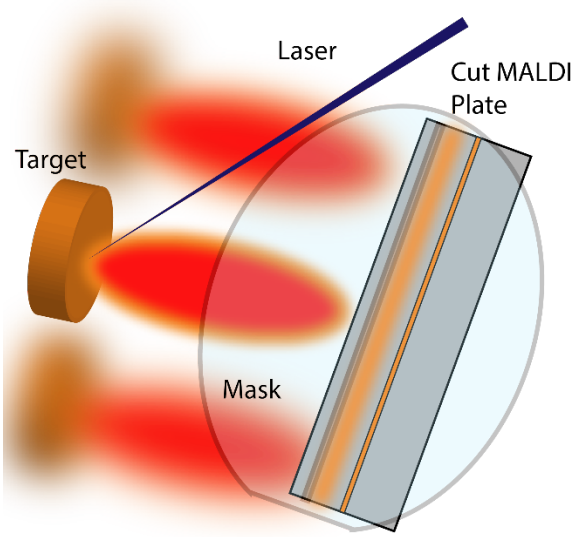

Figure 4.15 Schematic of fabrication of the planar TiO2 columns for on target enrichment

4.6 References

1. Rozen, S., et al., *Metabolomic analysis and signatures in motor neuron disease.* Metabolomics, 2005. **1**(2): p. 101-108.
2. Paige, L.A., et al., *A preliminary metabolomic analysis of older adults with and without depression.* International journal of geriatric psychiatry, 2007. **22**(5): p. 418-423.
3. Holmes, E., et al., *Metabolic profiling of CSF: evidence that early intervention may impact on disease progression and outcome in schizophrenia.* PLoS Med, 2006. **3**(8): p. e327.
4. Kaddurah-Daouk, R., *Metabolic profiling of patients with schizophrenia.* PLoS Med, 2006. **3**(8): p. e363.
5. Kaddurah-Daouk, R., et al., *Metabolomic mapping of atypical antipsychotic effects in schizophrenia.* Molecular psychiatry, 2007. **12**(10): p. 934-945.
6. Han, X., et al., *Substantial sulfatide deficiency and ceramide elevation in very early Alzheimer's disease: potential role in disease pathogenesis.* Journal of neurochemistry, 2002. **82**(4): p. 809-818.
7. Brindle, J.T., et al., *Rapid and noninvasive diagnosis of the presence and severity of coronary heart disease using 1H-NMR-based metabonomics.* Nature medicine, 2002. **8**(12): p. 1439-1445.
8. Sabatine, M.S., et al., *Metabolomic identification of novel biomarkers of myocardial ischemia.* Circulation, 2005. **112**(25): p. 3868-3875.
9. Brindle, J.T., et al., *Application of chemometrics to 1 H NMR spectroscopic data to investigate a relationship between human serum metabolic profiles and hypertension.* Analyst, 2003. **128**(1): p. 32-36.
10. Dunne, V.G., et al., *Metabolites from cerebrospinal fluid in aneurysmal subarachnoid haemorrhage correlate with vasospasm and clinical outcome: a pattern-recognition 1H NMR study.* NMR in Biomedicine, 2005. **18**(1): p. 24-33.
11. Kenny, L.C., et al., *Novel biomarkers for pre-eclampsia detected using metabolomics and machine learning.* Metabolomics, 2005. **1**(3): p. 227-234.
12. Van der Greef, J., et al., *The art and practice of systems biology in medicine: mapping patterns of relationships.* Journal of proteome research, 2007. **6**(4): p. 1540-1559.
13. Wang, C., et al., *Plasma phospholipid metabolic profiling and biomarkers of type 2 diabetes mellitus based on high-performance liquid chromatography/electrospray mass spectrometry and multivariate statistical analysis.* Analytical chemistry, 2005. **77**(13): p. 4108-4116.
14. Yuan, K., et al., *A GC-based metabonomics investigation of type 2 diabetes by organic acids metabolic profile.* Journal of Chromatography B, 2007. **850**(1): p. 236-240.
15. Yang, J., et al., *Diagnosis of liver cancer using HPLC-based metabonomics avoiding false-positive result from hepatitis and hepatocirrhosis diseases.* Journal of Chromatography B, 2004. **813**(1): p. 59-65.

16. Odunsi, K., et al., *Detection of epithelial ovarian cancer using 1H-NMR-based metabonomics.* International journal of cancer, 2005. **113**(5): p. 782-788.
17. Fan, X., J. Bai, and P. Shen. *Diagnosis of breast cancer using HPLC metabonomics fingerprints coupled with computational methods*. in *Conference proceedings:... Annual International Conference of the IEEE Engineering in Medicine and Biology Society. IEEE Engineering in Medicine and Biology Society. Annual Conference*. 2004.
18. Underwood, B.R., et al., *Huntington disease patients and transgenic mice have similar pro-catabolic serum metabolite profiles.* Brain, 2006. **129**(4): p. 877-886.
19. Fisher-Wilson, J., *Long-suffering lipids gain respect: Technical advances and enhanced understanding of lipid biology fuel a trend toward lipidomics.* The Scientist, 2003. **17**: p. 5.
20. Lagarde, M., et al., *Lipidomics is emerging.* Biochimica et biophysica acta, 2003. **1634**(3): p. 61.
21. Duzgunes, N., et al., *Proton-induced fusion of oleic acid-phosphatidylethanolamine liposomes.* Biochemistry, 1985. **24**(13): p. 3091-3098.
22. Pernet, F., C.J. Pelletier, and J. Milley, *Comparison of three solid-phase extraction methods for fatty acid analysis of lipid fractions in tissues of marine bivalves.* Journal of Chromatography A, 2006. **1137**(2): p. 127-137.
23. Avila, V.L., et al., *Cleanup of environmental sample extracts using Florisil solid-phase extraction cartridges.* Journal of chromatographic science, 1989. **27**(5): p. 209-215.
24. Wei, W., et al., *Elimination of the interference from nitrate ions on oxalic acid in RP-HPLC by solid-phase extraction with nanosized hydroxyapatite.* Journal of Liquid Chromatography & Related Technologies, 2008. **32**(1): p. 106-124.
25. Gerdes, J.C., et al., *Kit comprising solid phase matrix made of aluminum oxide, titanium oxide (Ti2O3) and/or modified zirconium dioxide (ZrO2) for identifying and extracting viral nucleotide sequences*. 2006, Google Patents.
26. Leitner, A., *Phosphopeptide enrichment using metal oxide affinity chromatography.* TrAC Trends in Analytical Chemistry, 2010. **29**(2): p. 177-185.
27. Lemeer, S., et al., *Online Automated in Vivo Zebrafish Phosphoproteomics: From Large-Scale Analysis Down to a Single Embryo.* Journal of Proteome Research, 2008. **7**(4): p. 1555-1564.
28. Mohammed, S., et al., *Chip-Based Enrichment and NanoLC− MS/MS Analysis of Phosphopeptides from Whole Lysates.* Journal of proteome research, 2008. **7**(4): p. 1565-1571.
29. Bruce, S.J., et al., *Investigation of human blood plasma sample preparation for performing metabolomics using ultrahigh performance liquid chromatography/mass spectrometry.* Analytical Chemistry, 2009. **81**(9): p. 3285-3296.
30. Moco, S., et al., *Metabolomics technologies and metabolite identification.* TrAC Trends in Analytical Chemistry, 2007. **26**(9): p. 855-866.

31. Teahan, O., et al., *Impact of analytical bias in metabonomic studies of human blood serum and plasma.* Analytical chemistry, 2006. **78**(13): p. 4307-4318.
32. Ikeguchi, Y. and H. Nakamura, *Selective Enrichment of Phospholipids by Titania.* Analytical Sciences, 2000. **16**(5): p. 541-543.
33. Calvano, C., O. Jensen, and C. Zambonin, *Selective extraction of phospholipids from dairy products by micro-solid phase extraction based on titanium dioxide microcolumns followed by MALDI-TOF-MS analysis.* Analytical and Bioanalytical Chemistry, 2009. **394**(5): p. 1453-1461.
34. Shen, Q., et al., *Lipidomic study of olive fruit and oil using TiO 2 nanoparticle based matrix solid-phase dispersion and MALDI-TOF/MS.* Food Research International, 2013. **54**(2): p. 2054-2061.
35. Polson, C., et al., *Optimization of protein precipitation based upon effectiveness of protein removal and ionization effect in liquid chromatography–tandem mass spectrometry.* Journal of Chromatography B, 2003. **785**(2): p. 263-275.
36. Vuckovic, D. and J. Pawliszyn, *Systematic Evaluation of Solid-Phase Microextraction Coatings for Untargeted Metabolomic Profiling of Biological Fluids by Liquid Chromatography− Mass Spectrometry.* Analytical chemistry, 2011. **83**(6): p. 1944-1954.
37. Eriksson, A., et al., *Mesoporous TiO2-Based Experimental Layout for On-Target Enrichment and Separation of Multi-and Monophosphorylated Peptides Prior to Analysis with Matrix-Assisted Laser Desorption-Ionization Mass Spectrometry.* Analytical chemistry, 2011. **83**(3): p. 761-766.

5 Quantifying interactions between serum proteins and gold nanoparticles

5.1 Abstract

Understanding the interactions of serum proteins to surfaces are of paramount importance to the domain of nano-drug delivery systems. At the nano-bio interface, human plasma differentially interacts with engineered nanomaterials through the creation of protein coronas, which in turn become primary determinants of both the pharmacokinetics and pharmacodynamics of the circulating nanoparticles. Here, for the first time, the specific binding kinetics of the four major corona forming proteins (human serum albumin, fibrinogen, ApoA1, and polyclonal IgG) are determined for gold nanoparticles (AuNPs). Using a multiplexed surface plasmonic assay, highly reproducible measurements of on rate (k_{on}), off rate (k_{off}), and dissociation constant (K_D), in addition to relative amounts of protein binding, were obtained. Dramatic differences in k_{on} for individual components were shown as primary determinants of protein affinities, with k_{on} ranging over nearly two orders of magnitude for the proteins studied, while k_{off} remained within a factor of two for the set. The effect of polyethylene glycol (PEG) modification on plasma component binding was also studied and the effect of PEG length on human serum interaction was characterized through systematic screening of PEG molecular weight (2K – 30K). The effect of nanoparticle modification on particle targeting was also characterized through study of a hybrid AuNP system.

5.2 Introduction

5.2.1 Overview

In the last chapter, we looked at how we could use the SPR technique could be used to accurately quantify phospholipid-metal oxide interactions. A more complex group of biomolecules, perhaps the most important, are proteins.

The “nano-bio” interface has been a domain of high interest in recent years. As nanoparticles find increasing use in both diagnostic and therapeutic roles, the interface between engineered materials and complex human biology is experiencing an expanded focus due to its critical implications for nanomedicine and nanotoxicity.[1-6] Upon gaining access to the circulation, nanoparticles undergo an association with plasma components, forming a non-covalent protein corona around their surface. It is now known that this protein corona is dynamic in nature and that its identity changes over time.[7, 8] The more abundant proteins bind to the exposed surface of the NP upon contact. Thereafter there is a dynamic competition between the species already present on the surface and additional components which have slower association rates, but ultimately higher affinity for the surface.[9, 10] It is also well understood that the chemical nature, charge, shape and size of the NPs all play significant roles in the formation of the corona.[11, 12]

5.2.2 Existing methods used to study corona formation and their limitations

The formation of the biomolecular corona plays a critical role in the fate of the NP complex.[13, 14] Hence, a platform to characterize the formation, evolution and kinetics of corona on various nanomaterials becomes crucial for applications such as *in vitro* diagnostic sensors, *in vivo* diagnostic probes or drug delivery technologies.[15] A commonly used method to study the protein corona formed around NPs is the enzymatic digestion of bound protein followed by polyacrylamide gel electrophoresis and/or mass spectroscopy.[16-20] While this method gives insight to the distribution of bound entities, it is not without limitations, i.e., taking significant manual effort with a large number of sequential experimental steps and typically 8-12 days[16] for a complete workflow. Dynamic Light Scattering (DLS),[21] Differential Centrifugal Sedimentation (DCS)[21, 22] and Size Exclusion Chromatography (SEC)[23] are additional, useful techniques that characterize the diffusional radius of nanoparticles and their bound coronas, however kinetic analyses are largely precluded due to technical limitations. As DLS is limited to colloidally stable NPs with a narrow size distribution (typically larger than 10nm) and often has difficulty resolving unbound from bound corona components, Fluorescence Correlation Spectroscopy (FCS)[24, 25] has since emerged as an alternative to DLS, but it requires NPs to be first modified with a fluorescent tag.[26] The affinity of proteins for the NPs may not be the same as their fluorescently labelled forms. Moreover, FCS is sensitive to the fluorescence of protein-NP complexes only if the autofluorescence from unbound proteins can be neglected.

An additional drawback with DLS and FCS is their inability to provide meaningful data for anisotropic shapes.[17] Furthermore, if the change in hydrodynamic radius of the protein-NP complex after adsorption is not significantly large, neither DLS nor FCS can feasibly resolve the change.[27] Hence the methods are usually used to investigate small NPs (but much larger than proteins themselves). There is a need for a method which can return kinetic data from real-time interactions, be sufficiently adaptable to work for a variety of sizes, shapes and chemical compositions and enable high-throughput data collection with high precision within reasonable time frames.

5.2.3 Need for a new method and previously reported work

Surface plasmon resonance (SPR) is a technique that uses disruptions to surface plasmons, i.e. delocalized electrons on, typically, a gold surface, to study binding reactions with time resolved high fidelity measurements. Cedervall et al[23] used SPR to observe dilute plasma modification of a biopolymeric NP, noting wide differences in disassociation rates as a function of hydrophobic content of the particle. A more recent study examined the effects of protein components on a SPR surface as they effected liposome absorption [28]. Although both studies demonstrated the utility of SPR in time resolved NP recordings, neither study was able to report affinity constants or kinetic determinants of NP modification by individual plasma components.

In this study, we have chosen AuNPs as our model system because of their ease of synthesis, characterization and relevance/use in targeted delivery. We have immobilized native AuNPs on the surface without additional functionalization,

thus enabling the study of serum proteins with the native surface of the AuNPs. Beyond studying the interactions of chosen serum proteins with native AuNPs, we used our protocol to study both PEG modification effects on blood components and hybrid targeted AuNPs interactions with serum.

To better understand the kinetic determinants of plasma component affinities to AuNPs, in addition to their relative adhesion efficiencies, we developed a multiplexed SPR assay using a commercially available (BioRad XPR36 SPR platform) reaction surface, thus enabling the extensive control measurements needed for subtraction of non-specific and background binding. Through a layer-by-layer modification strategy, we could monitor construction of modified AuNP's and then analyze them to obtain kinetic rate constants and relative adhesion amounts for specific plasma components, with experimental runs lasting no more than 3 hours.

5.3 Results and discussion

5.3.1 Immobilization of gold NPs

The gold surface of the GLC^{TM} chip from BioRad is supplied with a modified alginate polymer which provides a net negative charge and active sites for ligand immobilization. The alginate polymer layer also prevents non-specific binding to the chip surface – a common artefact in SPR experiments. Sulfo-NHS (N-hydroxysulfosuccinimide) enables control and modification of carbodiimide crosslinking reactions involving activation of carboxylates (—

COOH) for conjugation with primary amines (—NH_2). Derivatives are synthesized by mixing sulfo-NHS with a carboxyl-containing molecule and a dehydrating agent which in our case is 1-ethyl-3-(3-dimethylaminopropyl) carbodiimide (EDAC). Hence, the linker amino-EG6-undecanethiol hydrochloride, is immobilized onto the chip through amide coupling. The corresponding change in SPR signal can be seen from time 0 to 600 seconds in the sensorgram showed in **figure 5.1A**. The –SH end of the linker is now free and the AuNPs are immobilized on the surface of the chip through these free –SH groups. It is possible to monitor the immobilization in real time as seen from t = 950 s to 1700 s in figure 1A. The distribution and density of immobilized AuNPs was assessed directly using SEM as seen in **figure 5.1B**, allowing us to correlate SPR response with the final density of AuNP coating.

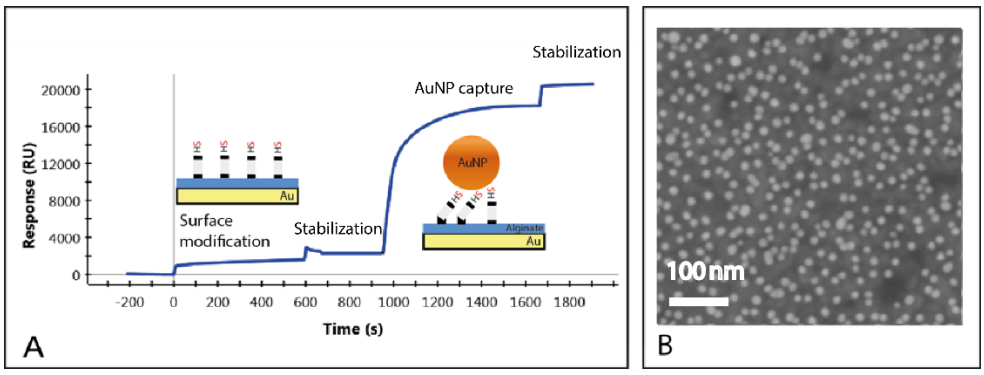

Figure 5.1 (A) SPR sensorgram of surface modification using a hetero-bifunctional linker and subsequently, the immobilization of AuNPs. **(B)** SEM image of the sensor surface after AuNP injection

Gold NPs used in this study are citrate-capped. The citrate capping provides long term stability against charge imbalance induced aggregation. Citrate weakly associates with the nanoparticle surface and is readily replaced by thiols.

Hence there is no effect of citrate capping on the capture by the chemical linker. One advantage of being able to observe the systematic deposition and modification of nanoparticles in preparation of a downstream experiment is to ensure regularity of the substrate, i.e. differences in reactivity of linkage chemistries, particle formulations, etc. can be seen as aberrant profiles in the assembly stage, as visualized by real time SPR. Hence the method allows for step checks to enhance reproducibility across multiple runs. We would also like to point out the platform nature of our protocol. By changing the linker molecule, it is potentially possible to immobilize additional classes of NP through diverse attachment chemistries and study its interactions, thereafter, with relevant proteins. We also would like to state that the size of the nanoparticle is 17 nm and its peak SPR wavelength is about 520 nm. The laser used in our study has a wavelength of 632.8 nm and hence there is no plasmonic coupling. At this size of the nanoparticle, there is absolutely no effect of gold on the evanescent wave per se. Hence, the immobilized gold NP could very well be any other NP.

Upon analyzing the SEM image shown in f**igure 5.2A**, we find that there are 1584 AuNPs captured in an area of 1987712 nm^2 (1696 nm X 1172 nm).

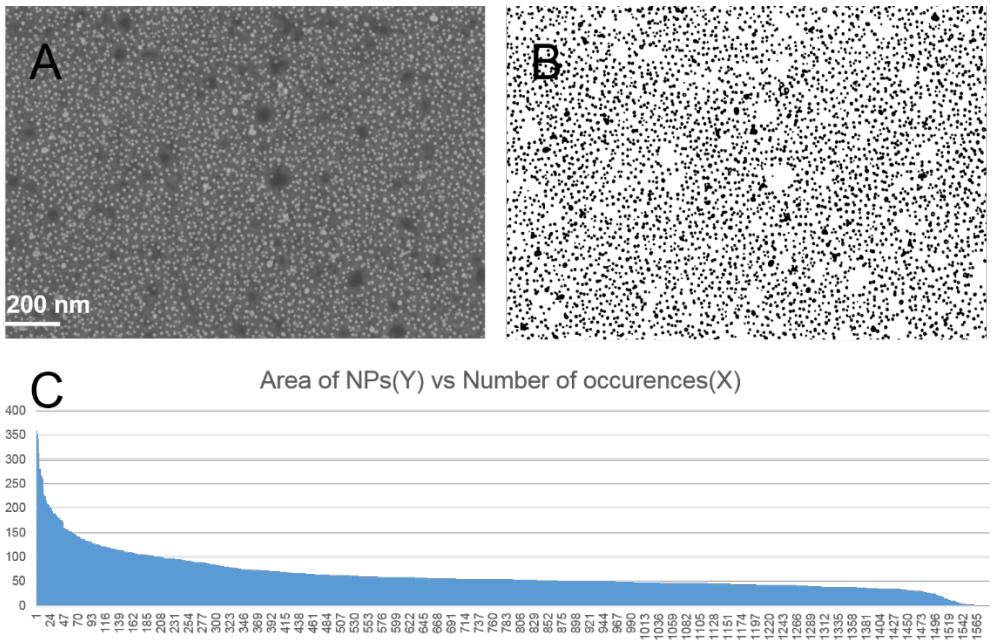

Figure 5.2 (A) SEM image of the chip surface after immobilization of AuNP. **(B)** The same image, processed with ImageJ to enable counting of AuNPs. **(C)** Distribution of particles on the surface. It can be seen that there is almost no agglomeration and the AuNPs are well dispersed.

5.3.2 Studying interactions of AuNPs with proteins

One of the major advantages of multiplexing data acquisition using SPR is reproducibility. Owing to the availability of 6 x 6 microfluidic channels leading into 36 interaction spots that can be monitored simultaneously, it is possible to obtain 36 sensorgrams representing 36 interactions in a single experimental run. We designed our experiments to have unambiguous co-temporal controls to compare the experimental data to. These are set out in detail in the caption of **figure 5.3** where a schematic representation has also been provided.

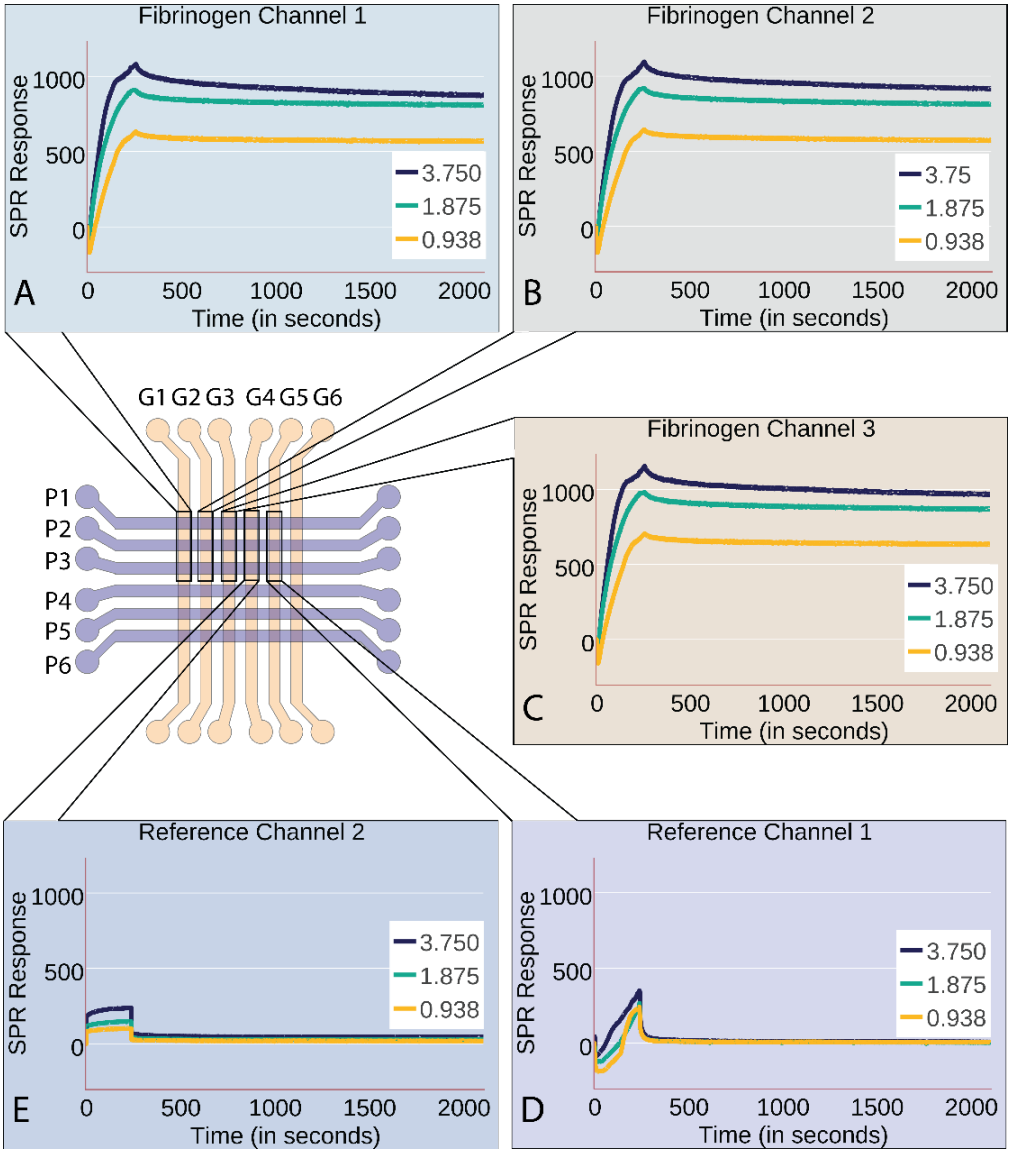

Figure 5.3 The microfluidic channel setup allowing multiplexed data collection is shown. AuNPs are immobilized in 3 channels G1, G2 and G3 using EDC/S-NHS coupling as described. Two control channels (G4 and G5) are employed. G4 channel is modified with all the linker chemistry used to capture AuNPs (but AuNPs are not injected). G5 channel is in as received condition (alginate layer with inactive –COOH groups). Fibrinogen in three concentrations (3.750 µM, 1.775 µM and 0.938 µM) is injected along channels P1, P2 and P3 respectively. The three colored lines (blue, green, yellow) in each panel correspond to 3 different concentrations of fibrinogen used in the experiment (legend in white box in each panel) **(A), (B)** and **(C)** Sensorgrams showing the interaction of fibrinogen with bare AuNPs available in channels G1, G2 and G3. **(D)** Sensorgram resulting from the interaction of fibrinogen with the chemically active lane without the AuNPs. **(E)** Sensorgram showing the interaction of fibrinogen with the unmodified surface (alginate polymer layer).

The four most common serum proteins found in nanoparticle coronas: human serum albumin (HSA), fibrinogen, immunoglobulin G (IgG) and apolipoprotein A1 (ApoA1), were selected for analysis.[29-31] After the AuNPs were immobilized and stabilized on the chip, 3 different concentrations of the 4 chosen proteins were flushed into the chip to observe the interactions. The association rate constant (i.e., k_{on} or on-rate), the dissociation rate constant (i.e., k_{off} or off-rate) and the equilibrium dissociation constant (K_D) were determined through first order kinetic curve fitting (**Table 5.1**)

Table 5.1 Kinetic rate constants and equilibrium dissociation constants for four chosen serum proteins as calculated from fitting curves to the experimentally obtained SPR responses

Label	k_{on} [$M^{-1}s^{-1}$]	k_{off} [s^{-1}]	K_D [µM]
HSA	466.860 ± 252.10	0.00184 ± 0.00033	04.93 ± 2.41
Fibrinogen	3857.330 ± 1031.08	0.00205 ± 0.00043	00.53 ± 0.08
I_gG	232.47 ± 24.19	0.00233 ± 0.00068	10.13 ± 3.28
ApoA1	18634.00 ± 9590.50	0.00163 ± 0.00007	00.12 ± 0.07

The fibrinogen primary data are shown in **figure 5.3A-C**. Sensograms for the three remaining proteins can be found in **appendix section A-3**. The SPR surface has a very thin coating of alginate hydrogel to separate the gold surface from the tethered nanoparticle of interest. To demonstrate lack of interaction of the gold surface with the AuNP's, we employed a negative control lane wherein AuNP is flowed above the surface without activated linker chemistry. No interaction was observed in this setting. This is likely due to the separating effect of the thin layer of alginate hydrogel on the surface of the chip. Alginate

typically forms a hydrogel with greater than 98% water content, creating a near native surface for AuNP attachment and minimizing surface adsorption (experiments with corona components and no AuNP also showed no interaction). Thus, although SPR has generally been an accepted methodology for component - specific kinetic studies of many types, there may exist differences with AuNP's experiencing full diffusional freedom, i.e. the corona kinetics of freely dissolved particles or colloidal suspensions.

ApoA1 has the lowest K_D of 0.12 ± 0.07 μM, implying that it binds most strongly to the surface of the AuNP. Fibrinogen follows with a K_D of 0.53 ± 0.08 μM. The affinity of HSA affinity for the surface of AuNP is about 10-fold lower than that of fibrinogen, bearing a K_D of 4.93 ± 2.41 μM. IgG is the component with least affinity (amongst the four chosen serum components) bearing a K_D of 10.13 ± 3.28 μM, implying it is about half as active as HSA with regard to adsorption onto the AuNP surface. Tsai et al [32] have reported K_D values for interaction of BSA with AuNPs using Langmuir adsorption models on data obtained through electrospray-differential mobility analysis (1.96 μM), fluorescence assay (1.61 μM) and attenuated total reflectance Fourier transform infrared spectroscopy (0.6 μM). As can be seen, the values of K_D for HSA-AuNP adsorption as obtained through SPR are within the same order of magnitude as BSA-AuNP adsorption, previously demonstrated through 3 different methods. To the best of our knowledge, kinetic and formal affinity constant data for the other major components interacting with AuNPs have not been previously reported.

We observed remarkable differences in k_{on} as obtained for the four proteins, while k_{off} values were comparable. ApoA1 (highest affinity) binds to the AuNP

surface with an association constant almost 100 times higher than IgG (lowest affinity). Overall, on-rates were found to play by far the largest role in the determination of component specific particle affinity for AuNPs.

Studies of absolute distributions of known plasma components are rare, the most relevant prior study may be Mahmoudi et al, [33] which described corona component binding to gold nanorods. This study used normalized spectral counts on LCMS (Liquid chromatography – mass spectrometry) to assign a relative binding amount of HSA and ApoA1 of 5.4 and 14.95, or a ratio of 1:2.8. Comparing values calculated using our kinetic measurements and known plasma concentrations of HSA and ApoA1, we arrive at a very similar ratio of 1:3 **(Table 5.2)**, consistent with the ability to approximate relative contributions to corona formation based on individualized kinetic and affinity measurements.

Table 5.2 Estimated surface coverage of individual proteins in protein corona

Label	K_D (µM)	$K_A = 1/K_D$	Physiological concentration (µM)	K_A[Protein]
HSA	4.93	0.20284	630	127.789
Fibrinogen	0.53	1.886792	7.8	14.71698
I_gG	10.13	0.098717	83	8.193485
ApoA1	0.12	8.333333	44	366.6667

One significant limitation of the SPR approach is that component-specific kinetic data can only be extracted from sensorgrams using purified reagents. In the setting of complex biofluids, serum, plasma, urine, etc., aggregate rates of

modification can be observed, however measurement of component-specific rate constants in this setting is generally not possible.

There are also limitations to kinetic analysis as performed through SPR. Largely due to mass transport limitations, it is difficult to measure k_{on} values faster than about 10^6 M^{-1} s^{-1} accurately.[34] This upper limit is dependent on the size of the analyte. In case of analytes with high molecular mass, faster k_{on} values can be measured. This is because the larger signal produced by a large analyte allows the experiment to be performed at lower ligand densities, and lower ligand densities require lower rates of mass transport. For instance, a higher k_{on} of 10^7 M^{-1} s^{-1} was measured by SPR for the interaction between HIV Tat protein with integrin $\alpha_v\beta_3$.[35] In case of k_{off}, values slower than 10^{-5} s^{-1} can be difficult to accurately measure, mainly due to issues with instrument drift over long periods of time.[34, 36]

5.3.3 Effect of PEGylation observed through SPR

To evaluate the effect of PEG modification on plasma component binding, we used our multiplexed SPR protocol to establish saturating modification of thiolated PEG onto the AuNP based on the real-time SPR signal. Once surface saturation of PEG was achieved, we were able to demonstrate differential effects on plasma components and PEG length-specific effects on NP modification by serum. Modification of injectable therapeutics with PEG is well known to affect circulation half-life and decrease protein binding.[37, 38] However, more specific effects on individual plasma components is less clear.

After immobilizing AuNPs on the chip surface, PEG-2000 was injected. To address the possibility that thiol groups on PEG-2000 may displace the immobilized AuNPs from the assay chip, we verified retention of the AuNPs through SEM images after the experiment was completed. We observed that PEGylation was effective at preventing adhesion of all four serum proteins (**figure 5.4**). The level of signal originating from adhesion of proteins was normalized to the level of signal change observed when the AuNPs were immobilized on the surface. It is seen that PEGylation is about 99% effective in blocking HSA (**figure 5.4A**) while PEGylation is about 94% effective against fibrinogen (**figure 5.4B**). The adsorption of IgG was reduced by about 93% (**figure 5.4C**). PEGylation was found to be very effective against ApoA1 (**figure 5.4D**) adsorption as well, showing a 98% decrease

It is important to note the significance of adsorption of proteins on NPs functionalized with antifouling agents (in this case PEG). Even though the amount of adsorption is small, if the adsorbing protein triggers cell surface receptors, the uptake machinery of the cell may be activated. In turn, this would lead to internalization of the NP by the reticuloendothelial system (RES) and thereby reduce circulation time. Further, the adsorption of other complement proteins such as C1q, MBL, ficolin and C3b, even at trace amount, would be sufficient to trigger an undesirable complement activation.

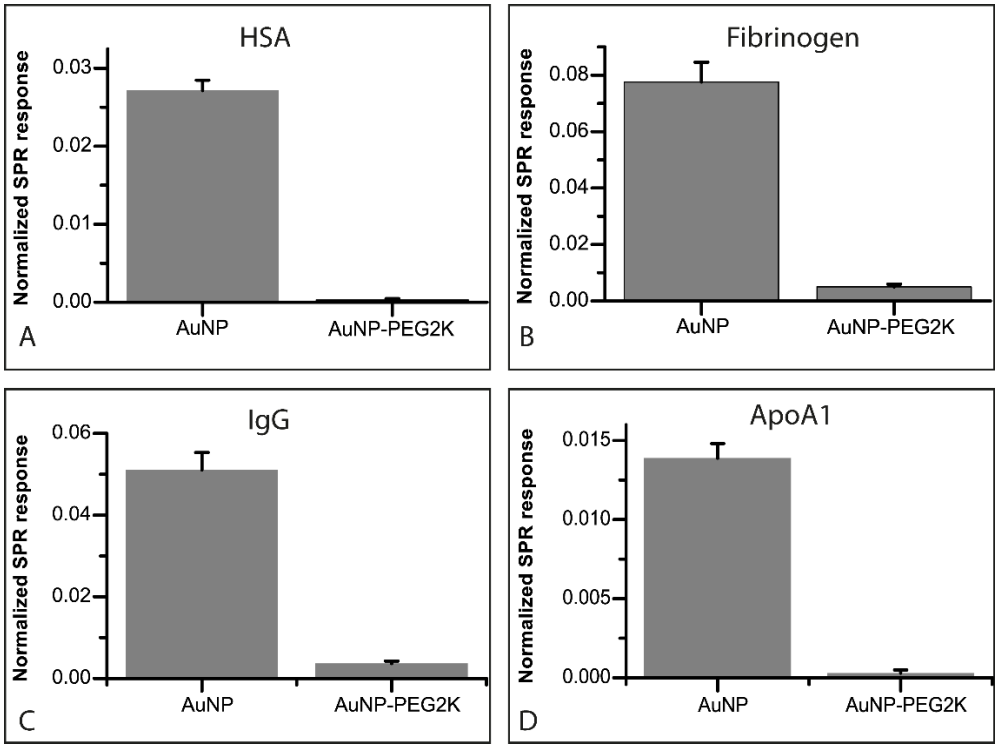

Figure 5.4 Normalized SPR response for interaction of individual serum proteins [**(A)** HSA, **(B)** Fibrinogen, **(C)** IgG, **(D)** ApoA1] with AuNPs modified with PEG2K compared to unmodified AuNPs. The absolute response obtained due to adsorption of proteins to modified and unmodified AuNPs is divided by the absolute response caused by the immobilization of AuNPs on the sensor surface. This normalization, hence, takes care of the minor differences in number of AuNPs captured in each lane.

5.3.4 Effect of varying PEG chain length on resistance to corona

After having validated the effect of PEGylation on individual plasma components, we decided to investigate the effect of PEG chain length moieties on the resistance of the functionalized NP to corona formation. To accomplish this study, PEG molecules having average molecular weight (MW) of 2K, 5K, 10K, 20K and 30K were chosen. After duly immobilizing AuNPs on the chip surface as before, we injected the chosen PEG moieties, each in a separate lane, leaving a control lane with unmodified AuNPs. This lane would serve as a

control to compare our findings to. All absolute responses were normalized to the SPR response resulting from the capture of AuNPs in the designated lanes, to allow for cross comparability. To avoid problems due to probable differential affinities of varying PEG chains to the gold surface, every sample of PEG was injected thrice with an aim to saturate the surface of the gold with PEG. This enabled us to get as close to complete coverage of surface as possible so that artefacts due to partial coverage of exposed surface could be minimized.

The nanomedicine community has long been dealing with the "PEG dilemma."[39] Due to the presence of its long apolar chains, PEG has been shown to reduce protein adsorption. However in recent years, PEGylation has also been shown to strongly inhibit cellular uptake and limit the binding with intended protein targets thereby reducing the potential of drug delivery significantly. Hence, the emerging trend seems to revolve around optimization – such that the functionalization is made to retard protein adsorption but not so much that it limits its ability to be trafficked into cells and deliver its cargo.

Here, we found that PEG 2K, PEG 5K and PEG 10K are very similar in their resistance to corona formation allowing only 14%, 10% and 15% adsorption, respectively, as compared with an unmodified surface (**figure 5.5**). PEG 20K and 30K were the least effective anti-fouling moieties of the group allowing 31% and 40% respectively. Hence PEG 2K, 5K and 10K are about 3-4 times more effective than the longer chained ones. Our data is thus consistent with prior reports indicating that shorter PEG chains pack more tightly to the surface of an exposed NP thereby creating a more efficient shield against non-specific protein adsorption on the surface. [40]

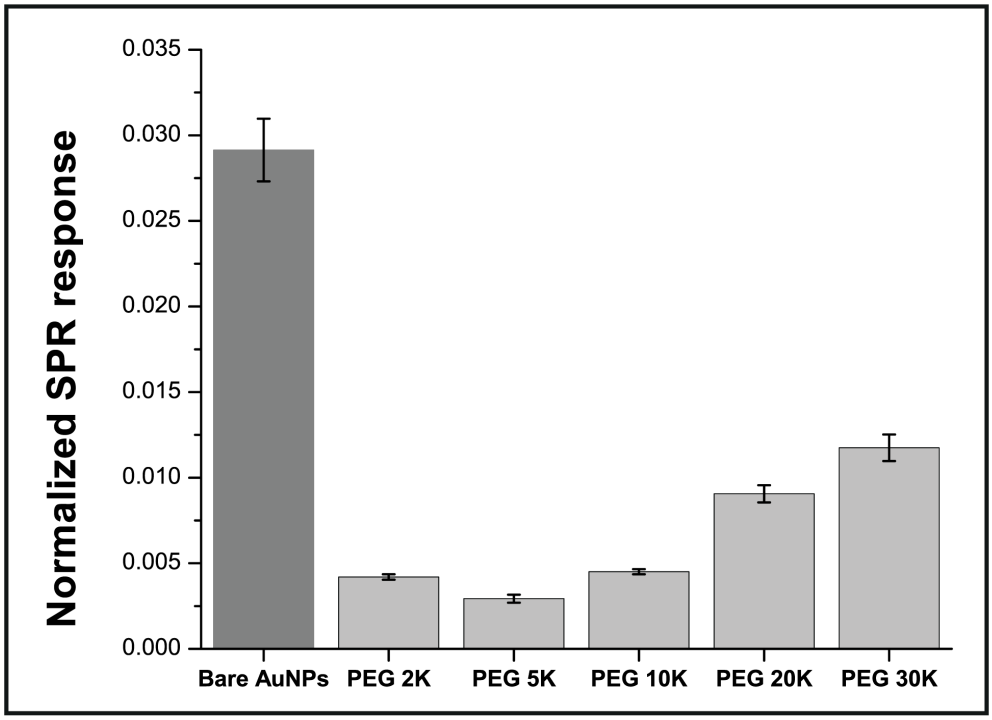

Figure 5.5 Normalized SPR response for interaction of 20% (W/V) human serum (diluted with PBS buffer) with AuNPs modified with PEG2K, PEG5K, PEG10K, PEG20K and PEG30K compared to unmodified AuNPs. With the exception of PEG 2K and PEG 5K, all sets of data were statistically different from all other sets.(p-value <<0.05)

As the PEG chain length increases, the PEG molecules are understood to adopt a "mushroom" conformation with reduced packing density that allow proteins to bind to available exposed areas on the NP surface.[41] It has been previously suggested that protein adsorption to PEG grafted surfaces is very sensitive to chain density effects and less so to chain length.[40, 42] Although our data is consistent with this hypothesis, further experiments will need to be performed to accurately characterize steric effects of linear and branched PEG molecules. Likewise, there are conflicting reports in literature regarding the effect of the chain length on adsorption. Gref *et. al*. [43] have reported that when polylactic acid (PLA) NPs were functionalized with varying lengths of PEG, the most amount of protein is found adsorbed to PEG 2K. PEG 5K, 10K, 15K and 20K

are all similar in their resistance to adsorption and they adsorb about 40% of protein that is adsorbed by PEG 2K. On the other hand, a more recent report by Pozzi *et. al*. [44] claims that when varying chain lengths of PEG are used to functionalize multicomponent cationic liposomes, PEG 1K adsorbs the most amount of proteins while PEG 2K and PEG 5K both adsorb about 50% of PEG 1K.

We would also like to mention here that in a control experiment designed to determine whether PEG binds to the chip surface. We injected AuNPs in 4 lanes and had an empty lane with all the required chemical linkers to capture the AuNPs, but didn't inject the AuNPs. We found, in the absence of the captured AuNPs, there is no interaction between PEG and the chemically active surface of the SPR chip. The data has been provided in the appendix section **A-4**.

5.3.5 Observation of hybrid modifications effect on NP targeting design

NP technologies engineered for therapeutic applications are often multifunctional, containing materials that target to the site of disease, optimize plasma half-life and provide therapeutic or imaging modalities. When the complexity of NP design is tested *in vivo*, interactions beyond the four major plasma components may become important. In particular, for particles that are functionalized with a specific targeting moiety, the cumulative effects of antifouling modifications may relate directly to binding capacity. Consequently, we synthesized a model NP system (named 'hybrid' in **figure 5.6**) to have a corona retarding moiety – the commonly used SH-PEG2K and a target binding

moiety – SH-PEG5K-Biotin (the target being streptavidin). The two controls that were used in this experiment were AuNPs functionalized with only SH-PEG2K and AuNPs functionalized with only SH-PEG5K-biotin (referred to as biotin). It is logical to conclude, in the hybrid configuration, the biotin end of the –SH-PEG5K-Biotin molecule will be accessible above the packing layer of –SH-PEG2K (since PEG5K is longer than PEG2K). **Figure 5.6A** shows the sensorgram from the interaction of 20% human serum with the functionalized AuNPs. The inset shows the schematic illustration of the interaction. To be able to compare the performance of the NP systems with respect to its resistance to biomolecular fouling and its ability to bind its intended target streptavidin, on each type of NP system, we have normalized the absolute SPR responses resulting from serum interaction and streptavidin binding to the level of gold initially captured in the lane. Compared to unmodified AuNP, all the lanes showed a drastic drop. PEG is well known to resist protein adsorption and hence the surface of the AuNP functionalized with PEG 2K shows 18% of the adsorption signal observed in the bare gold surface AuNPs. Likewise, PEG linked biotin shows about 17% adsorption when compared with unfunctionalized surface. The hybrid system, dramatically, shows only 3% adsorption of when compared with bare AuNP. We hypothesize this might be caused by a favorable interplay between the shielding accorded by the PEG 2K moiety and the PEG 5K section of the PEG5K-biotin moiety. The exact affinity of this hybrid system for serum proteins may perhaps be tailored by playing upon the ratio between SH-PEG and SH-PEG-biotin moieties.

In NP formulations, addition of new components almost always involves a trade-off with other functionalities. We thus studied the trade-off of biotin

streptavidin binding in the setting of additional PEG modification, in the highly controlled setting of multiplexed SPR. **Figure 5.6B** shows the sensorgram for the interaction of streptavidin with these modified AuNPs (schematic in inset). As expected, the unmodified AuNP showed almost no non-specific adsorption of streptavidin (3%). The AuNP with PEG alone showed no response because there was no biotin present. However, when we examined the biotin and hybrid systems, we were able to determine the precise trade-off in terms of streptavidin binding with 26% of streptavidin bound when compared with the original biotin-only particle. That the interaction is truly between biotin-streptavidin is evident from the extremely low off-rate and lack of interaction seen in control lanes. It should also be stated that since the surface of the AuNP in the case of the hybrid is shared by –SH-PEG2K and –SH-PEG5K-biotin, the number of available biotin groups for binding streptavidin will be much lesser than the case where the AuNP is modified with –SH-PEG5K-biotin alone. Hence a part of the reduced response can be attributed to a lesser number of target-binding ligands in the lane.

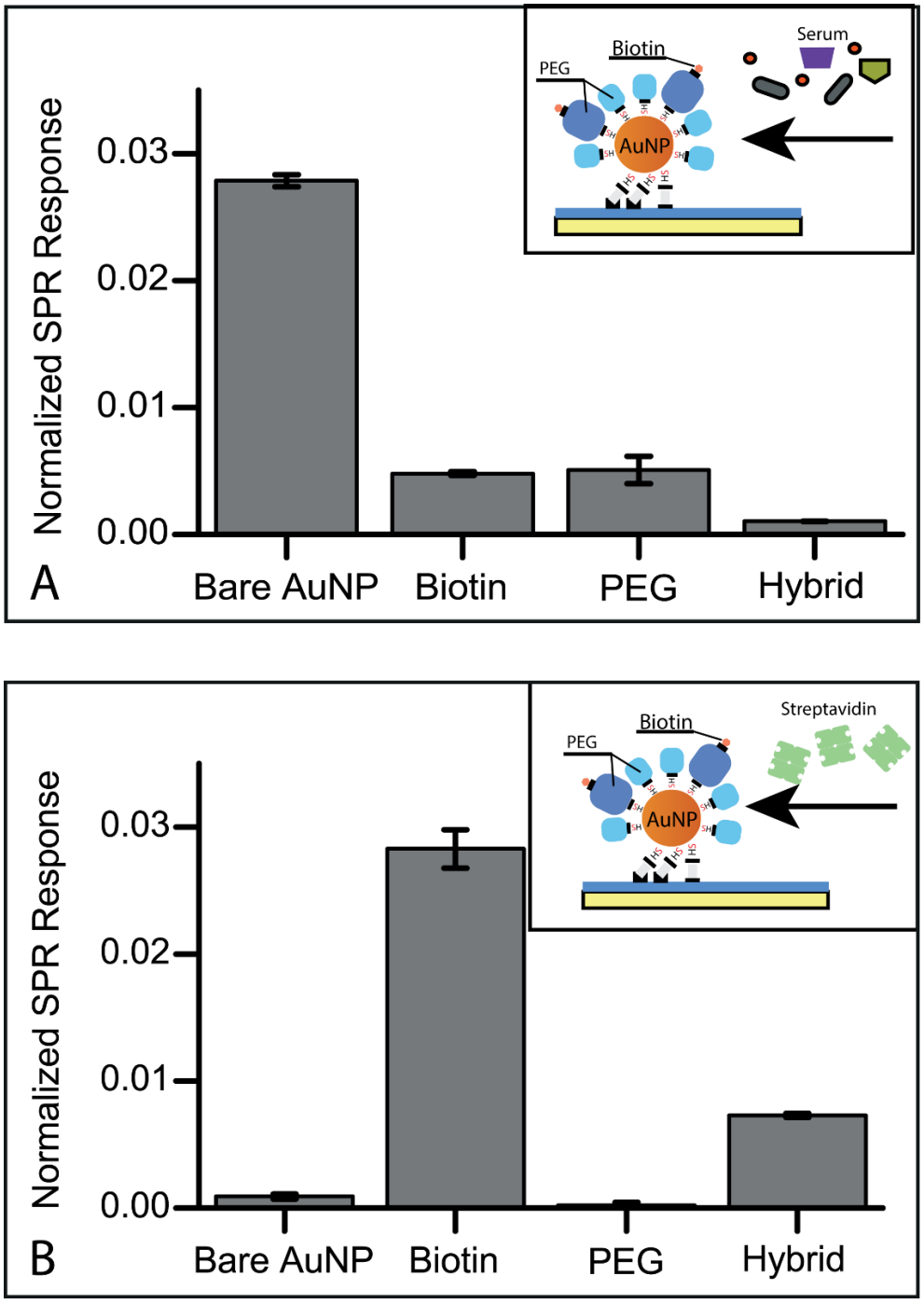

Figure 5.6 (A) Normalized SPR response for interaction of 20% human serum with AuNPs modified with PEG5K-biotin (referred to as "Biotin"), PEG2K and 1:1 mixture of Biotin:PEG2K (referred to as "Hybrid") compared to unmodified AuNPs. The inset illustrates the schematic of the experiment **(B)** Normalized SPR response showing the ability of AuNPs with previously described functionalizations to bind intended target streptavidin. The inset illustrates the schematic of the experiment. (p-value <<0.05)

5.4 Conclusion

We have established a robust protocol which can be used to study interactions of NPs with biomolecular entities of interest. Using multiplexed SPR measurements, including extensive controls, we were able to accurately determine kinetic measurements of plasma component interactions with AuNPs, including wide variation in association constants for individual plasma components, and conduct comparative studies of corona formation. A comparison with the existing techniques has been provided in the table **5.3**.

Table 5.3 Comparison of methods used to study corona formation on nanoparticles

Name of method	Pros	Cons	Error in measurement
DLS, DCS, SEC	1. Quick 2. Nanomaterial independent	1. Can't handle anisotropic shapes 2. Many restrictions on relative size of protein and nanoparticle	High
SDS-PAGE/MS	1. Nanomaterial independent 2. Comprehensive identification of all bound serum proteins	1. Very slow(8-10 days) 2. Large number of manual steps 3. Possibility of user bias	Medium

Multiplexed SPR	1. Nanomaterial independent 2. Can handle anisotropic shapes 3. Real time kinetic parameters of interaction 4. Fully automated – no user bias 5. Can be used to screen drug delivery formulations ex-vivo	1. Size of nanomaterial must be below 100 nm.	Low

In principle, the same protocol could be applied to a wide variety of NP materials and formulations as only a single point of attachment is required for the SPR surface and many NPs lie within the theoretical plasmonic sensing range of 100 nm. Although, in principle, the techniques and analysis of tethered polymeric NP's should be very similar to the AuNP's in this study, key differences in operational efficiency will be known only upon additional experimentation. Because test-particles are assembled on-chip, the ability to show saturation kinetics helps to ensure stabilized surface occupancy of modifying agents. The ability to perform multiple assays alongside proper controls using the same reagents on the same chip is of particular value given the multicomponent nature of nanoparticle designs and demonstrates the strength of multiplexed SPR.

5.5 Experimental details

5.5.1 Synthesis of AuNPs

The NPs were synthesized using the method of G Frens et al.[45] 100 mL of 1 mM hydrochloroauric acid ($HAuCl_4$) was heated until it boiled. 15 mL of 38.8 mM trisodium citrate was added to the solution while being vigorously stirred. After being boiled for 15 minutes, the solution changed color from pale yellow to purple before finally becoming a deep red NP colloid. The citrate-capped NP colloid was washed twice through centrifugation at 10 000 rpm for 15 min and diluted 10X for subsequent experiments. The zeta potential and hydrodynamic diameter (DH) of the NPs were measured at 25°C using a Zetasizer (Nano ZS, Malvern, UK), and the morphology characterized using transmission electron microscopy (TEM) (JEM-1220, JEOL Ltd., Japan). The concentration of the NPs was determined by optical absorption. The synthesized NPs were kept at 4 °C until further experiments.

5.5.2 Immobilization of AuNPs onto the chip surface

A Bio-Rad ProteOn XPR36 instrument (Haifa, Israel) was used in this study. The GLC type sensor chip consists of a glass prism coated with gold and an alginate layer with a low capacity for ligand conjugation. A detailed introduction of experimental protocol for ligand-analyte interactions can be found in literature.[46] The system was first equilibrated with PBS-T buffer (20 mM Na-phosphate, 150 mM NaCl, and 0.05 % Tween 20, pH 7.4). The

channels of the chip were activated for 5 minutes with a mixture of EDC (0.2 M) and sulfo-NHS (0.05 M), followed by 10 min injection of 1mM amino-EG6-undecanethiol (Dojindo Laboratories, Japan) and 5 minute injection of ethanolamine-HCl solution. Subsequently, AuNPs were injected onto the modified sensor lane for 6 minutes with a flow rate of 30µL/min. The chip is then flushed PBS-T for 30 minutes to monitor the dissociation of AuNP from the surface.

5.5.3 Studying interactions of serum components with immobilized AuNPs

Using aforementioned methods, 17nm AuNPs were captured on the SPR chip surface and stabilized for 30 minutes. Human serum Albumin (HSA), Human Fibrinogen and Human immunoglobulin G (IgG) and Human Apolipoprotein A1 (ApoA1) were dissolved in PBS and injected into the AuNP modified sensor surface. The injection time was 4 minutes at a flow rate of 100µl/min, followed by a dissociation step of 30 minutes. It has to be noted that the direction of injection of the proteins is orthogonal to the direction in which the AuNPs are injected. Please refer figure 2 for the layout of the chip. This means that in a single protein lane, we can obtain n interaction sensorgrams ($1 \leq n \leq 6$, depending on how many lanes have been populated with AuNPs)

5.5.4 Obtaining kinetic parameters from curve fitting and calculating surface coverage

The data obtained from the experiments was exported to and analyzed with Origin software package.

For the dissociation phase,

$$R_d = R_{d0} + A_1 e^{-k_{off} t} \quad (1)$$

where R_d is the response at any time t in the dissociation phase, R_{d0} is the response at the start of the as chosen dissociation phase, A is a constant, k_{off} is dissociation constant and t is time in seconds.

In the association phase,

$$R_a = A_2 - A_3 e^{-kt} \quad (2)$$

Where R_a is the response at any time in the association phase, A_2 and A_3 are constants and t is time in seconds. The parameter k will be used to determine k_{on}, by the formula given below

$$k_{on} C + k_{off} = k \quad (3)$$

where k_{off} is dissociation constant calculated from (1), k is the parameter obtained from (2) and C is concentration of protein in moles/liter.

Finally,

$$K_D = \frac{k_{off}}{k_{on}} \quad (4)$$

While fitting curves, care has to be taken to select such portions of the responses which are free from bulk refractive index changes. An example has been provided in **figure 5.7**

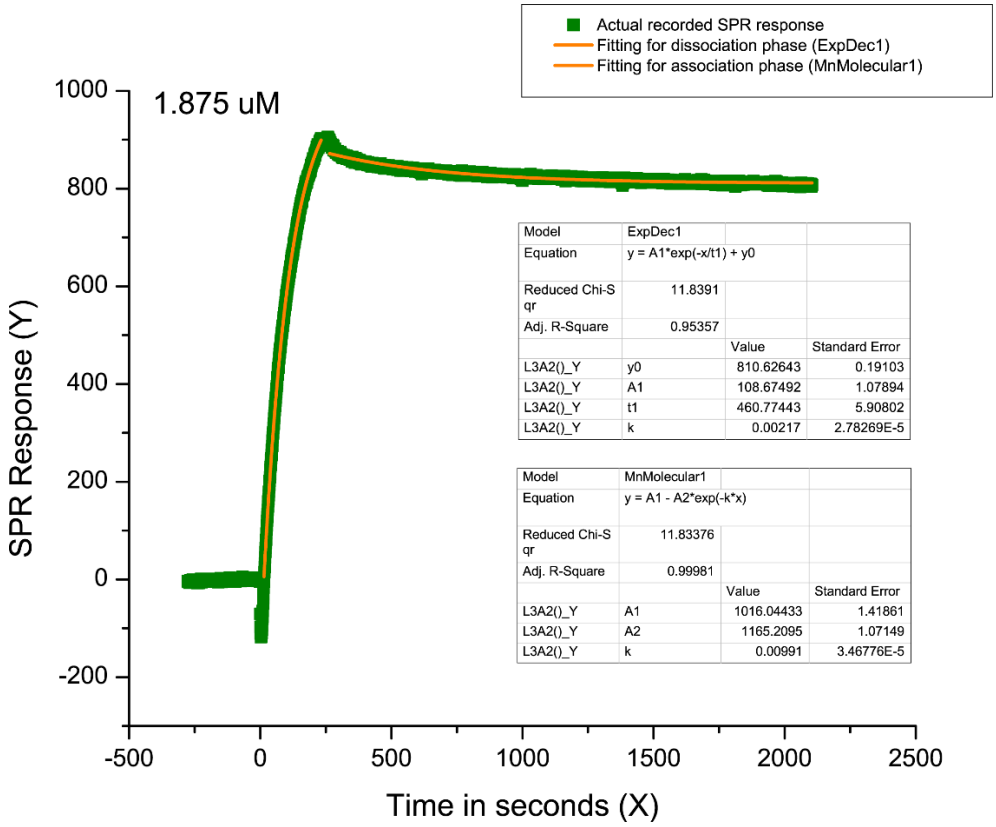

Figure 5.7 Example of curve fitting on Origin software package on experimentally collected data to obtain kinetic parameters

The interaction between the four proteins (A_1, A_2, A_3, A_4) and the AuNPs (B) can be described by the following process,

$$A_1 + B \underset{k_{d2}}{\overset{k_{a1}}{\rightleftharpoons}} A_1B$$

$$A_2 + B \underset{k_{d2}}{\overset{k_{a2}}{\rightleftharpoons}} A_2B$$

$$A_3 + B \underset{k_{d3}}{\overset{k_{a3}}{\rightleftharpoons}} A_3B$$

$$A_4 + B \underset{k_{d4}}{\overset{k_{a4}}{\rightleftharpoons}} A_4B$$

Assuming the mass transport is much faster than the surface reaction and the binding kinetics is interaction controlled, we can write the binding rate as

$$\frac{d[AB]}{dt} = k_a[A][B] - k_d[AB], \quad (5)$$

Where [A] represent the concentrations of A1, A2, A3, A4. And [B] is the concentration/surface of available AuNPs. As the concentration [A] is much higher than [B], i.e., [A]>>[B], the concentration of [*B*] is the function of time *t*, which is the difference between the concentration of maximal available concentration of B and the current complex concentration,

$$[B] = [B_{\max}] - [A_1B] - [A_2B] - [A_3B] - [A_4B]. \quad (6)$$

Upon dynamic equilibrium, the net effect of the association and dissociation process is zero, i.e.

$$\frac{d[A_1B]}{dt} = k_a[A_1][B] - k_d[A_1B] = 0 \quad (7)$$

$$\frac{d[A_2B]}{dt} = k_a[A_2][B] - k_d[A_2B] = 0 \quad (8)$$

$$\frac{d[A_3B]}{dt} = k_a[A_3][B] - k_d[A_3B] = 0 \quad (9)$$

$$\frac{d[A_4B]}{dt} = k_a[A_4][B] - k_d[A_4B] = 0 \quad (10)$$

As all of the reactions occur simultaneously, we can assume the concentration/surface of available AuNPs [B] are the same for the equation 7 to 10. Thus the above equations can be expressed as,

$$[A_1B] = \frac{k_{a1}[A_1][B]}{k_{d1}} = K_{a1}[A_1][B] \quad (11)$$

$$[A_2B] = \frac{k_{a2}[A_2][B]}{k_{d2}} = K_{a2}[A_2][B] \quad (12)$$

$$[A_3B] = \frac{k_{a3}[A_3][B]}{k_{d3}} = K_{a3}[A_3][B] \quad (13)$$

$$[A_4B] = \frac{k_{a4}[A_4][B]}{k_{d4}} = K_{a4}[A_4][B] \quad (14)$$

Where, $K_a=k_a/k_d$. Thus the ratio of each protein adsorbed on the surface AuNPs can be expressed as,

$$[A_1B]:[A_2B]:[A_3B]:[A_4B] = K_{a1}[A_1]:K_{a2}[A_2]:K_{a3}[A_3]:K_{a4}[A_4] \quad (15)$$

5.5.5 Studying interactions of serum components with PEGylated AuNPs

17nm AuNPs were captured on the SPR chip surface (as described in 5.5.2) and stabilized for 30mins. Thiolated PEG-2000 (Lysanbio, AL, USA) was dissolved in water to a concentration of 100mM and was injected onto the AuNPs modified SPR sensor surface. The injection time was 2 minutes followed by a stabilization step of 10mins. For protein injection, all four chosen serum components HSA, fibrinogen, IgG and ApoA1 were dissolved in PBS, as in the previous section. Then the sensor chip was rotated by 90°and the four proteins were injected on to the sensor surface at a flow rate of 100µL/min.

5.5.6 Studying effect of PEG chain length on corona formation

17nm AuNPs were captured on the SPR chip surface (as described above) and stabilized for 30mins. Thiolated PEG-2000, PEG-5000, PEG-10000, PEG-20000 and PEG30000 (Lysanbio, AL, USA) were dissolved in water, each separately, to a concentration of 100mM each and were injected onto the AuNPs modified SPR sensor surface. The injection time was 2 minutes followed by a stabilization step of 10mins. 20% diluted human serum was injected after the chip was rotated through 90°. The interaction between serum and PEGylated AuNPs was made to occur for 2 minutes after which the injection of serum was stopped and lanes were flushed with PBST to observe the dissociation phase.

5.5.7 Studying the interaction of serum and streptavidin with model hybrid NP systems

In this experiment, we first make the following solutions: a) 200µM of SH-PEG-Biotin (M.W.5000), denoted as biotin in figure 5, b) 200µM of SH-PEG-Biotin (M.W. 5000) and 100µM SH-PEG (M.W. 2000), denoted as Hybrid in figure 5, c) 100µM of SH-PEG (M.W.2000), denoted as PEG in figure 2.6.

Using previously mentioned methods, 17nm AuNPs were captured on the SPR chip surface and stabilized for 30 minutes. A hybrid layer of surface functionalization material is formed on the AuNPs by co-injection of 100µM of thiolated PEG-2000 (Lysanbio, US) and 200µM of thiolated PEG-biotin (Thermos Scientific), both dissolved in water. Using the same protocol, two other lanes were modified using 100µM of thiolated PEG-2000 and 200µM of

thiolated PEG-biotin, respectively. Human serum (Sigma-Aldrich, MO, USA) was diluted to 20% using PBS and injected onto the SPR Sensor. Streptavidin (Sigma-Aldrich, MO, USA) was dissolved in PBS buffer and injected onto the SPR sensor at a concentration of 100µM. The injection times for both analytes were 2 minutes at a flow rate of 100µl/min and sensor responses were recorded at 100 seconds after injection period. The sensor's inter-spots, which are the native surface of the sensor, were used as reference and all signals were subtracted from the reference signal.

5.6 References

1. Brewer, S.H., et al., *Probing BSA binding to citrate-coated gold nanoparticles and surfaces.* Langmuir, 2005. **21**: p. 9303-9307.
2. Brown, D.M., et al., *Interaction between nanoparticles and cytokine proteins: impact on protein and particle functionality.* Nanotechnology, 2010. **21**: p. 215104.
3. Bajaj, A., et al., *Stability, toxicity and differential cellular uptake of protein passivated-Fe3O4 nanoparticles.* J. Mater. Chem., 2009. **19**: p. 6328-6331.
4. Boraschi, D., L. Costantino, and P. Italiani, *Interaction of nanoparticles with immunocompetent cells: nanosafety considerations.* Nanomedicine, 2011. **7**: p. 121-131.
5. Cedervall, T., *Understanding the nanoparticle-protein corona using methods to quantify exchange rates and affinities of proteins for nanoparticles.* Proc. Natl Acad. Sci. USA, 2007. **104**: p. 2050-2055.
6. Fadeel, B. and A.E. Garcia-Bennett, *Better safe than sorry: understanding the toxicological properties of inorganic nanoparticles manufactured for biomedical applications.* Adv. Drug Deliv. Rev., 2010. **62**: p. 362-374.
7. Casals, E., et al., *Time evolution of the nanoparticle protein corona.* ACS Nano, 2010. **4**: p. 3623-3632.
8. Dell'Orco, D., et al., *Modeling the time evolution of the nanoparticle-protein corona in a body fluid.* PLoS ONE, 2010. **5**: p. e10949.
9. Gasser, M., *The adsorption of biomolecules to multi-walled carbon nanotubes is influenced by both pulmonary surfactant lipids and surface chemistry.* J. Nanobiotechnol., 2010. **8**: p. 31.
10. Cifuentes-Rius, A., et al., *Optimizing the properties of the protein corona surrounding nanoparticles for tuning payload release.* ACS nano, 2013. **7**(11): p. 10066-10074.
11. Deng, Z.J., *Differential plasma protein binding to metal oxide nanoparticles.* Nanotechnology, 2009. **20**: p. 455101.
12. Kah, J.C.Y., et al., *Protein Coronas on Gold Nanorods Passivated with Amphiphilic Ligands Affect Cytotoxicity and Cellular Response to Penicillin/Streptomycin.* ACS nano, 2014. **8**(5): p. 4608-4620.
13. Georgieva, J.V., *Surface characteristics of nanoparticles determine their intracellular fate in and processing by human blood-brain barrier endothelial cells in vitro.* Mol. Ther., 2011. **19**: p. 318-325.
14. Ghosh, P., *Intracellular delivery of a membrane-impermeable enzyme in active form using functionalized gold nanoparticles.* J. Am. Chem. Soc., 2010. **132**: p. 2642-2645.
15. Iversen, T.G., T. Skotland, and K. Sandvig, *Endocytosis and intracellular transport of nanoparticles: present knowledge and need for future studies.* Nano Today, 2011. **6**: p. 176-185.
16. Docter, D., et al., *Quantitative profiling of the protein coronas that form around nanoparticles.* Nat. Protocols, 2014. **9**(9): p. 2030-2044.
17. Mahmoudi, M., et al., *Temperature: The "Ignored" Factor at the NanoBio Interface.* ACS Nano, 2013. **7**(8): p. 6555-6562.

18. Jedlovszky-Hajdú, A., et al., *Surface Coatings Shape the Protein Corona of SPIONs with Relevance to Their Application in Vivo.* Langmuir, 2012. **28**(42): p. 14983-14991.
19. Lesniak, A., et al., *Effects of the Presence or Absence of a Protein Corona on Silica Nanoparticle Uptake and Impact on Cells.* ACS Nano, 2012. **6**(7): p. 5845-5857.
20. Tenzer, S., et al., *Nanoparticle Size Is a Critical Physicochemical Determinant of the Human Blood Plasma Corona: A Comprehensive Quantitative Proteomic Analysis.* ACS Nano, 2011. **5**(9): p. 7155-7167.
21. Monopoli, M.P., et al., *Physical−Chemical Aspects of Protein Corona: Relevance to in Vitro and in Vivo Biological Impacts of Nanoparticles.* Journal of the American Chemical Society, 2011. **133**(8): p. 2525-2534.
22. Walczyk, D., et al., *What the Cell "Sees" in Bionanoscience.* Journal of the American Chemical Society, 2010. **132**(16): p. 5761-5768.
23. Cedervall, T., et al., *Understanding the nanoparticle–protein corona using methods to quantify exchange rates and affinities of proteins for nanoparticles.* Proceedings of the National Academy of Sciences, 2007. **104**(7): p. 2050-2055.
24. Liedl, T., et al., *Fluorescent Nanocrystals as Colloidal Probes in Complex Fluids Measured by Fluorescence Correlation Spectroscopy.* Small, 2005. **1**(10): p. 997-1003.
25. Nienhaus, G.U., P. Maffre, and K. Nienhaus, *Chapter Four - Studying the Protein Corona on Nanoparticles by FCS*, in *Methods in Enzymology*, Y.T. Sergey, Editor. 2013, Academic Press. p. 115-137.
26. Zhang, F., et al., *Polymer-Coated Nanoparticles: A Universal Tool for Biolabelling Experiments.* Small, 2011. **7**(22): p. 3113-3127.
27. Cho, E.J., et al., *Nanoparticle Characterization: State of the Art, Challenges, and Emerging Technologies.* Molecular Pharmaceutics, 2013. **10**(6): p. 2093-2110.
28. Canovi, M., et al., *Applications of Surface Plasmon Resonance (SPR) for the Characterization of Nanoparticles Developed for Biomedical Purposes.* Sensors (Basel, Switzerland), 2012. **12**(12): p. 16420-16432.
29. Aggarwal, P., et al., *Nanoparticle interaction with plasma proteins as it relates to particle biodistribution, biocompatibility and therapeutic efficacy.* Advanced drug delivery reviews, 2009. **61**(6): p. 428-437.
30. Karmali, P.P. and D. Simberg, *Interactions of nanoparticles with plasma proteins: implication on clearance and toxicity of drug delivery systems.* Expert opinion on drug delivery, 2011. **8**(3): p. 343-357.
31. Göppert, T. and R. Müller, *Adsorption kinetics of plasma proteins on solid lipid nanoparticles for drug targeting.* International journal of pharmaceutics, 2005. **302**(1): p. 172-186.
32. Tsai, D.-H., et al., *Adsorption and conformation of serum albumin protein on gold nanoparticles investigated using dimensional measurements and in situ spectroscopic methods.* Langmuir, 2011. **27**(6): p. 2464-2477.
33. Mahmoudi, M., et al., *Variation of protein corona composition of gold nanoparticles following plasmonic heating.* Nano letters, 2013. **14**(1): p. 6-12.

34. Núñez, S., J. Venhorst, and C.G. Kruse, *Target–drug interactions: first principles and their application to drug discovery.* Drug discovery today, 2012. **17**(1): p. 10-22.
35. Urbinati, C., et al., *αvβ3-integrin-dependent activation of focal adhesion kinase mediates NF-κB activation and motogenic activity by HIV-1 Tat in endothelial cells.* Journal of cell science, 2005. **118**(17): p. 3949-3958.
36. Chu, R., D. Reczek, and W. Brondyk, *Capture-stabilize approach for membrane protein SPR assays.* Scientific reports, 2014. **4**.
37. Otsuka, H., Y. Nagasaki, and K. Kataoka, *PEGylated nanoparticles for biological and pharmaceutical applications.* Adv. Drug Deliv. Rev., 2003. **55**: p. 403-419.
38. Kim, H.R., *Analysis of plasma protein adsorption onto PEGylated nanoparticles by complementary methods: 2-DE, CE and protein lab-on-chip system.* Electrophoresis, 2007. **28**: p. 2252-2261.
39. Hatakeyama, H., H. Akita, and H. Harashima, *The Polyethyleneglycol Dilemma: Advantage and Disadvantage of PEGylation of Liposomes for Systemic Genes and Nucleic Acids Delivery to Tumors.* Biological and Pharmaceutical Bulletin, 2013. **36**(6): p. 892-899.
40. Jeon, S.I., et al., *Protein—surface interactions in the presence of polyethylene oxide: I. Simplified theory.* Journal of Colloid and Interface Science, 1991. **142**(1): p. 149-158.
41. Kah, J.C.Y., et al., *Critical parameters in the pegylation of gold nanoshells for biomedical applications: an in vitro macrophage study.* Journal of drug targeting, 2009. **17**(3): p. 181-193.
42. McPherson, T., et al., *Prevention of Protein Adsorption by Tethered Poly(ethylene oxide) Layers: Experiments and Single-Chain Mean-Field Analysis.* Langmuir, 1998. **14**(1): p. 176-186.
43. Gref, R., et al., *'Stealth' corona-core nanoparticles surface modified by polyethylene glycol (PEG): influences of the corona (PEG chain length and surface density) and of the core composition on phagocytic uptake and plasma protein adsorption.* Colloids and Surfaces B: Biointerfaces, 2000. **18**(3–4): p. 301-313.
44. Pozzi, D., et al., *Effect of polyethyleneglycol (PEG) chain length on the bio-nano-interactions between PEGylated lipid nanoparticles and biological fluids: from nanostructure to uptake in cancer cells.* Nanoscale, 2014. **6**(5): p. 2782-2792.
45. Frens, G., *Controlled nucleation for the regulation of the particle size in monodisperse gold suspensions.* Nature, 1972(241): p. 20-22.
46. Nahshol, O., et al., *Parallel kinetic analysis and affinity determination of hundreds of monoclonal antibodies using the ProteOn XPR36.* Analytical biochemistry, 2008. **383**(1): p. 52-60.

6 Conclusion

No work in science is beyond improvement. On our part, we believe we have demonstrated techniques to make measurements possible where they were none previously and accurate where they were inaccurate and error-prone. But, just as we have stated earlier, there is always more work to be done and some improvement to be made.

The technique for ascertaining the hydrophilicity/hydrophobicity of a solid surface has been the contact angle of water method for a very long time. Through advancements in precision syringes, motors with very precise pitch and optics, the technique has, of course become more accurate over the years. However, with sciences being more intent towards traversing down the length scales from macro to micro to nano, this well-proven technique has been faced with a seemingly unsurmountable problem. Unless we generate extremely small droplets in the nano or picolitre regime, the resultant data acquired will have inherent artefacts resulting from the averaging of various chemical heterogeneities on the surface. Herein, lies our breakthrough. The use of force-distance curves to quantify hydrophilicity of surfaces is a simple technique which can be very useful for obtaining local surface energies from extremely small areas on surfaces. Since the tip of an AFM cantilever is usually around 5-10 nm in diameter, we would in fact be able to probe such small areas without the need for expensive equipment which generate nano/picolitre droplets for extremely complicated nano/picolitre level contact angle measurements. The technique of deriving hydrophilicity from the interaction of the AFM tip from the native water layer on the surface is also affected by the material used to

fabricate the tip. Hence, the logical next step is to acquire F-D curves over the same samples with different tips made of standard materials used by the AFM probe manufacturers. When this data is available, it will become possible to generate universal curves for each tip which can be referred to readily to find the probable local surface energy and contact angle for a particular unknown sample being explored with a known tip.

The impact of the study of interactions between phospholipids and metal oxides is perhaps the most immediate. In general, through our own endeavors, we have found that it is difficult to control all the parameters which influence interaction of metal oxides and lipid species. Reports in literature do talk about successes in selectively enriching non-phospholipid fractions of lipidomes by trapping phospholipids. However, no attempt has been made to understand and control the various parameters which exert their own influences. Primary among them is the actual contact area of metal oxides available for phospholipid capture. There is a very interesting conundrum here. Ideally, one would need to have smallest possible particles to maximize the available surface area. However, as the particles become smaller, they pack closer and closer thereby generating very high backpressures in the column. High backpressures also slow down liquid flow through the column which changes the amount of time phospholipids spend in contact with the resins. This contributes to experimental error. Through rigorous experimentation, we have found the lower limit of particle size, beyond which the fabrication of a working μcolumn is impossible. The pressure required to push liquids through such μcolumn is enough to completely rupture the μcolumn as such. The surface plasmon resonance based technique for studying phospholipid adhesion to oxide surfaces has been a novel

approach to the field of solid phase extraction resin design. By bringing contact area and flow rate under experimental control, we have been able to precisely quantify the amount of phospholipids that adhere to the oxide surfaces meant to act as solid phase extraction resins. Another off-shoot of this approach is the easy way to know if a particular oxide etches away under the conditions used to bind phospholipids. Under the binding conditions generally used, we found 5 oxides that form salts which are detrimental to the health of mass spectrometry systems apart from causing suppression of ionization of lipid species. From our data, we have outlined 3 oxides which can be used for the purpose of phospholipid capture. All of them are from the 3d period. It would be interesting to see if the same trend is maintained in the 4d or 5d period. Since rare earth oxides are also d^0 systems, efforts can also be directed towards studying their interaction with phospholipids. However, unless a significant increase in performance is obtained, it might not be financially profitable to use 4d oxides or rare earth oxides since they are generally more expensive than the best performing 3d counterparts. Knowledge of phospholipid-metal oxide interactions will ultimately help in the fabrication of fraction enrichment devices in a variety of formats which are completely compatible with the workflow which has been around for more than two decades.

The multiplexed surface plasmon resonance based technique for studying serum proteins interacting with nanoparticles is an exciting addition to the tools being widely used today. Though nano-bio interfaces have been a hot area of scientific investigation over the last 7-8 years, the existing tools have limitations. Simple techniques like DCS, FCS, DLS and Zeta potential evaluation are fast in terms of their turnaround time. However the data varies highly across experimental

runs and hence show high error bars. More comprehensive techniques like SDS-PAGE/MS are accurate but are very labor-intensive and the large number of steps involved in collecting meaningful data introduces the possibility of user-dependent artefacts. Besides, none of the existing techniques are able to furnish true kinetic parameters of serum interactions with engineered nanomaterials in real time. By identifying all these deficiencies of all techniques and imagining what a reasonable solution to fill in the gap would be, we have been able to establish a robust protocol which, we are sure, will be used by researchers in the field immediately. With our technique, we have been able to obtain kinetic parameters of interactions of proteins with engineered nanosystems. These are of critical importance to researchers involved in the design of nano drug delivery systems (NDDS). The modular nature of the protocol enables users to choose any engineered nanomaterial and a corresponding chemical linker to capture it on the sensing surface. Further work would be directed towards studying interactions of more clinically relevant nanomaterials, such as SiO_2, Fe_3O_4, carbon nanotubes, PolyLactic Acid, liposomes and others. Moreover, using this technique, one can test the efficiency of anti-biofouling measures employed to prevent alteration of identity of the NDDS while still being functional enough to identify its intended target and deliver the packed cargo. This translates into significant savings on time and money, when only the most promising candidates from this initial screening, which takes only few hours to finish, are taken forward to the next round of rigorous testing.

In conclusion, it isn't an overstatement to say, we have indeed been able to quantify interactions of biomolecules with inorganic surfaces. We would like to close this work with this beautiful quote from one of the most creative minds of

the 20th century which captures the spirit with which this work has been accomplished.

"Around here, however, we don't look backwards for very long. We keep moving forward, opening up new doors, and doing new things, because we're curious and curiosity keeps leading us down new paths."

Walter Elias "Walt" Disney

Disneyland Paris - The Family Guide (2007), opening page

Appendix

A-1 Density Functional Theory Calculations

Further from ***section 3.3.4***

The adsorption energy of molecular and dissociated water, *OH and *H on the $SrTiO_3$, VO_2 and Lu_2O_3 has been computed by means of density functional theory (DFT) as implemented in the VASP code.[1] A Hubbard U term has been included on V *d* states and Lu *f* states (U_{eff}(V) = 3.25 eV [2] and U_{eff}(Lu) = 5.4 eV,[3] respectively). We considered the (001) orientation of $SrTiO_3$, both SrO and TiO_2-terminated, and (022) of VO_2(M) as they are expected to be the exposed film surfaces following the experimental indications. Note that $SrTiO_3$ sample preparation should result in a TiO_2-terminated surface. The cubic bixbyite phase of Lu_2O_3 expose preferentially the (111) surface, which has a large surface unit cell (16 Lu atoms per layer) and contains Lu ions with different local environment. We have then also considered the (0001) surface of hexagonal Lu_2O_3 as a simplified model. This surface contains only fully coordinated Lu ions and has a lower surface energy compared to the cubic bixbyite (111) surface (by 0.26 J/m^2), suggesting that the latter could reconstruct in order to minimize the number of under-coordinated cations. We can then infer that the two models represent the two extreme limits of surface reactivity, exposing reactive low-coordinated sites (cubic (111) surface) and less reactive fully coordinated cations (hexagonal (0001) surface). The adsorbate's binding energies have been computed in the low coverage regime (1/4 ML, where 1 ML would correspond to one adsorbate for surface metal atom) to assess relative

stability of *OH vs. H_2O (both dissociated and molecular) on the oxide surfaces. In the case of cubic Lu_2O_3, this coverage has been obtained by placing four evenly distributed adsorbates per unit cell. The water binding energy is computed with respect to the gas phase H_2O at 0.035 bar, while the *OH and *H binding energies are computed at 1.23 V with respect to the standard hydrogen electrode,[4, 5] which corresponds to the H_2O/O_2 equilibrium approximated to the ambient condition. The Gibbs free energies of the clean and adsorbate-covered surface have been computed by adding the zero point energy as estimated by vibrational analysis. The adsorption free energy has been defined as: G_{ad} = G(*X) - G(*) - μ(X), where G(*X) and G(*) represent the Gibbs free energy for the species X adsorbed on the surface and the clean surface respectively and μ(X) is the chemical potential of X, defined as follow:

$$\mu_{H_2O(g)}(=\mu_{H_2O(l)}) = \mu^0_{H_2O(g)} + k_b \cdot \ln\left(\frac{p(H_2O)}{p^0(H_2O)}\right)$$

$$\mu_{H_2(g)} = \mu^0_{H_2(g)} - 2e\varphi + 2k_bT \cdot \ln(a_{H^+})$$

where ϕ is the effective applied potential and the terms

$$\mu^0_{H_2O(g)} = E^{DFT}_{H_2O(g)} + ZPE_{H_2O(g)} - TS^0_{H_2O(g)}(0.035bar)$$

and

$$\mu^0_{H_2(g)} = E^{DFT}_{H_2(g)} + ZPE_{H_2(g)} - TS^0_{H_2(g)}$$

have been determined from the computed DFT total energy (E), the zero point energy (ZPE) and the entropic translational, rotational and vibrational energy contributions at room temperature. The chemical potential of H and OH are then defined as: μ(H)=$^1/_2\,\mu_{H_2(g)}$ and μ(OH)=$\mu_{H_2O(g)} - {}^1/_2\,\mu_{H_2(g)}$.

The computed G_{ad} is reported in Figure S3 for the modeled surfaces of (022) termination of VO_2(M), (001) SrO and TiO_2 terminations of $SrTiO_3$ (both), and hexagonal (0001) and cubic bixbyite (111) terminations of Lu_2O_3. For water both molecular and dissociative adsorption are reported, when stable. Spontaneous water dissociation was found on SrO-terminated $SrTiO_3$ (001) surface, indicating that molecular water is not stable. Conversely, only molecular water is found on hexagonal Lu_2O_3 (0001) surface, as the dissociated molecule readily recombines. In the case of cubic Lu_2O_3 (111) surface the dissociated state corresponds to a mixed adsorption, with one molecular and three dissociated water molecules in the unit cell. Indeed on this surface the adsorption characteristics strongly depend on the specific adsorption sites and range from preferentially molecular at the fully coordinated Lu sites (G_{ad} = 0.33 eV at 1/16 ML coverage) to dissociative at more exposed (low coordinated) Lu sites (G_{ad} = -0.27 eV at 1/16 ML coverage).

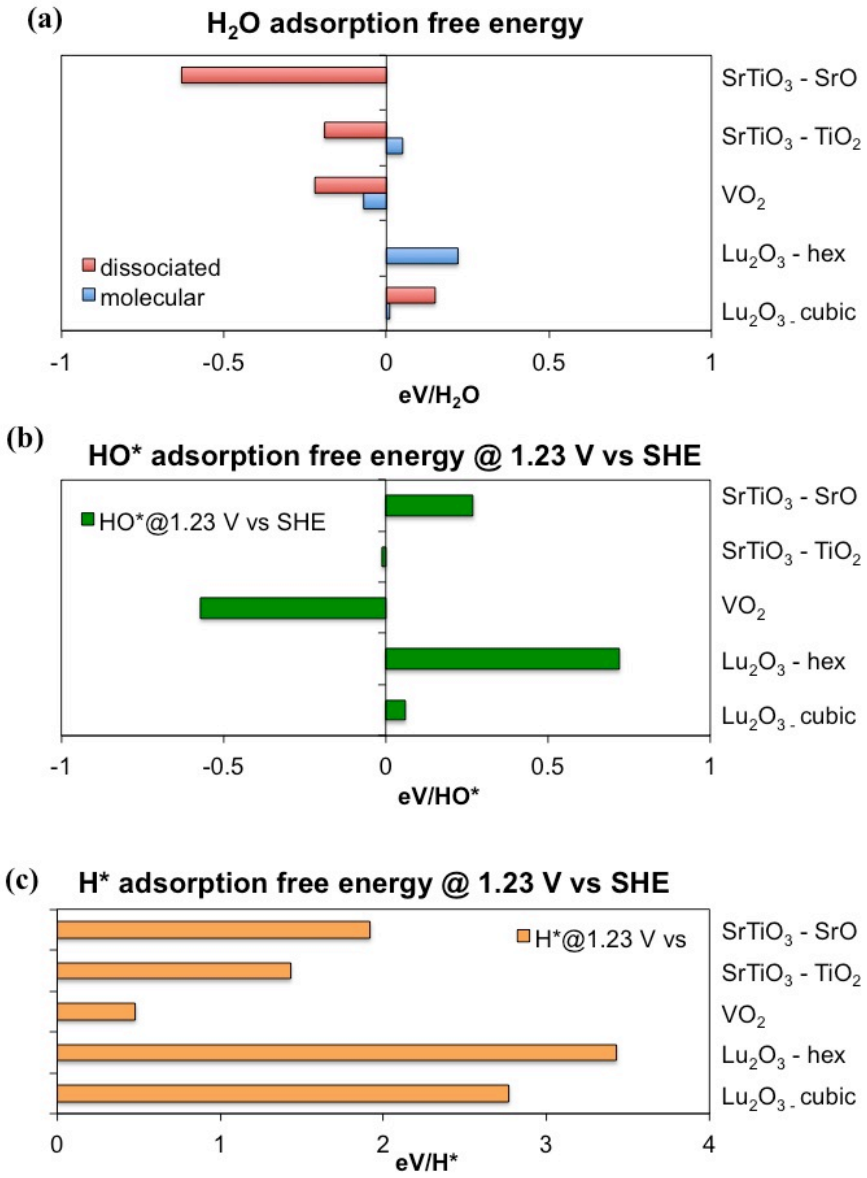

Figure 1: Computed adsorption free energies at 1.23 V with respect to the standard hydrogen electrode [4, 5] for (a) H_2O (molecular and dissociated), (b) *OH and (c) *H adsorbed on $SrTiO_3$ (001), VO_2(M) (022), hexagonal Lu_2O_3 (0001) and cubic bixbyite Lu_2O_3(111) surfaces computed at 1/4 ML coverage.

References

1. Kresse, G. and J. Furthmüller, *Efficient iterative schemes for ab initio total-energy calculations using a plane-wave basis set.* Physical Review B, 1996. **54**(16): p. 11169.
2. Wang, L., T. Maxisch, and G. Ceder, *Oxidation energies of transition metal oxides within the GGA+ U framework.* Physical Review B, 2006. **73**(19): p. 195107.
3. Jiang, H., et al., *Localized and Itinerant States in Lanthanide Oxides United by G W@ LDA+ U.* Physical review letters, 2009. **102**(12): p. 126403.
4. Norskov, J.K., et al., *Origin of the Overpotential for Oxygen Reduction at a Fuel-Cell Cathode.* The Journal of Physical Chemistry B, 2004. **108**(46): p. 17886-17892.
5. Rossmeisl, J., et al., *Electrolysis of water on oxide surfaces.* Journal of Electroanalytical Chemistry, 2007. **607**(1,Äì2): p. 83-89.

A-2 MALDI scans on TiO_2 strip used for on-target enrichment

Further from ***section 4.5.6***

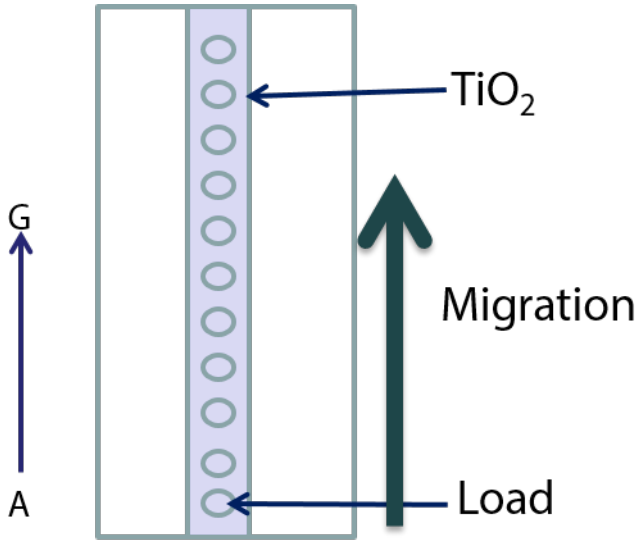

Figure 1: Schematic of plate layout showing how the MALDI-MS setup obtains scans of spots. A is the point where sample is spotted. Phospholipid migration happened up until F.

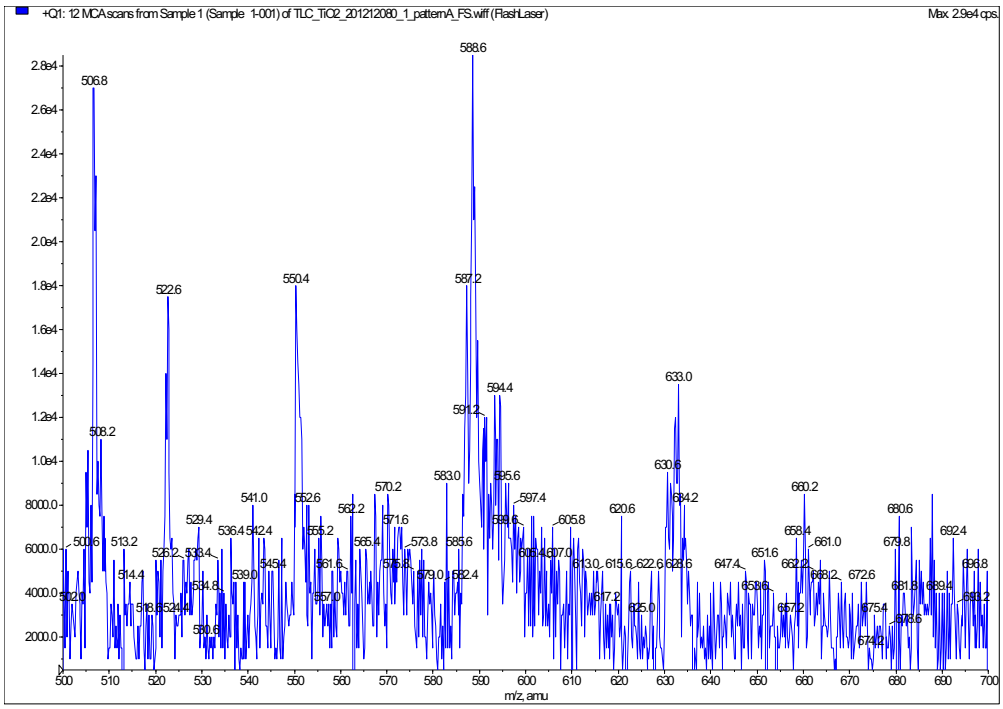

Position A

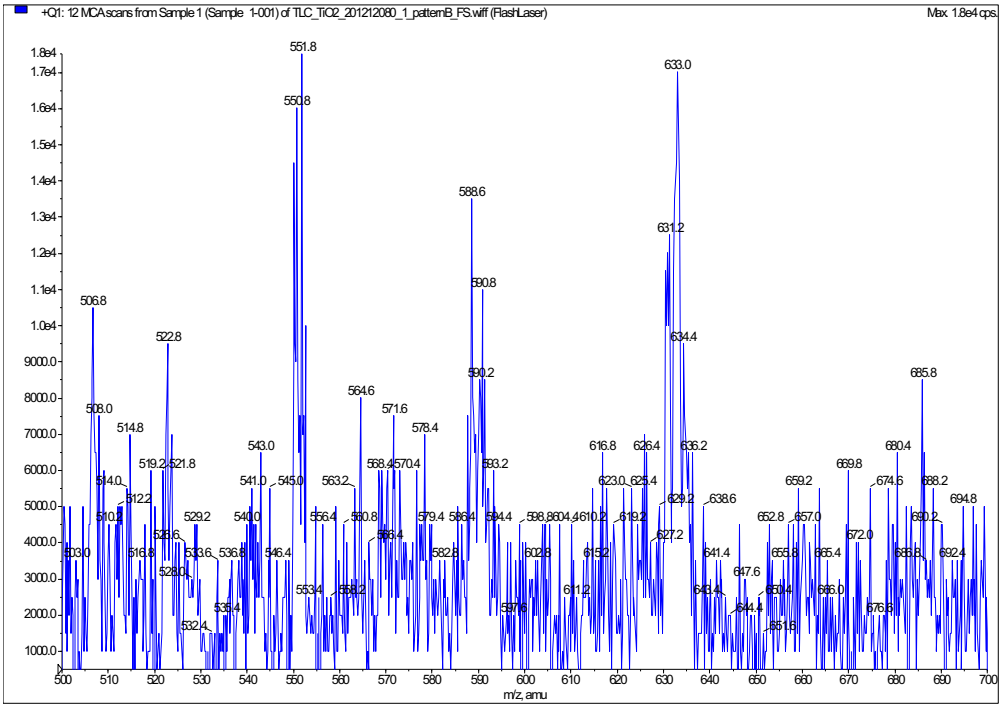

Position B

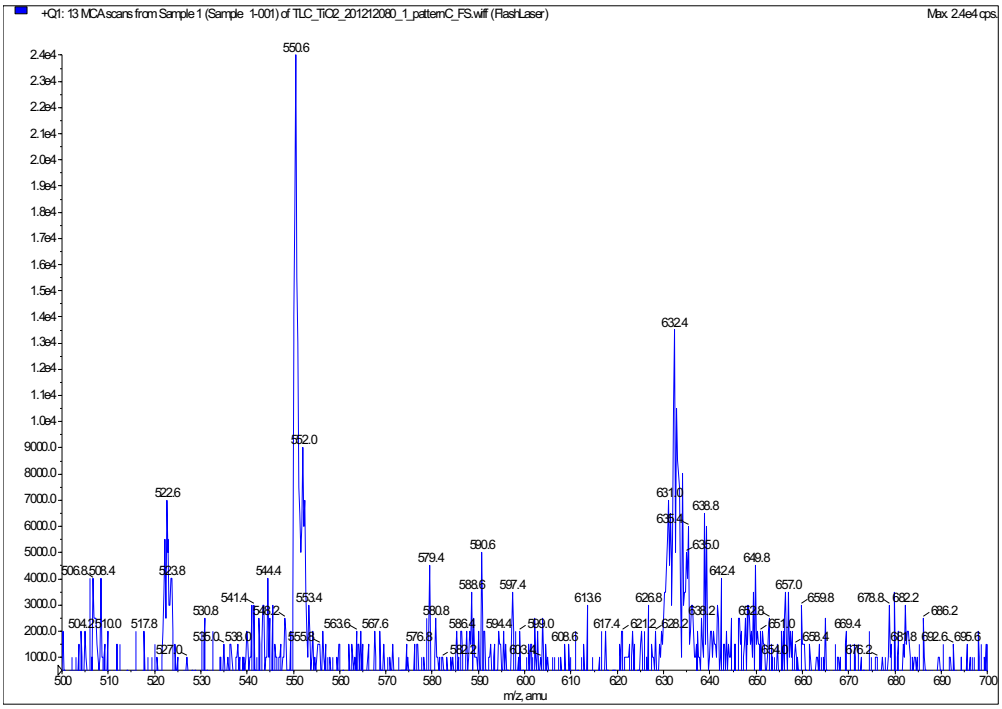

Position C

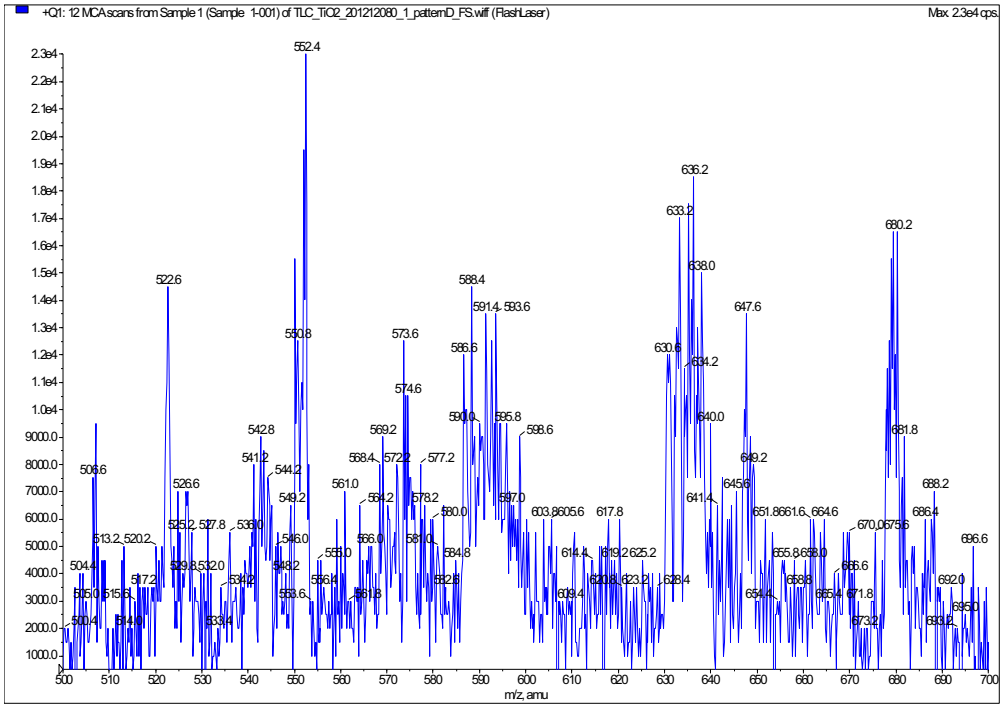

Position D

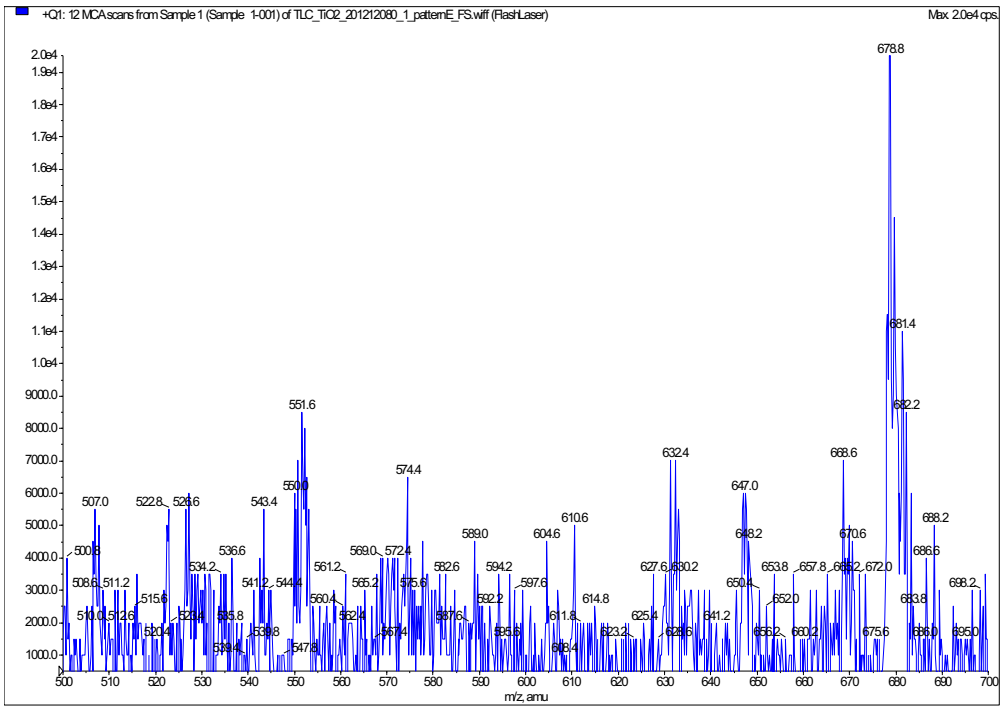

Position E

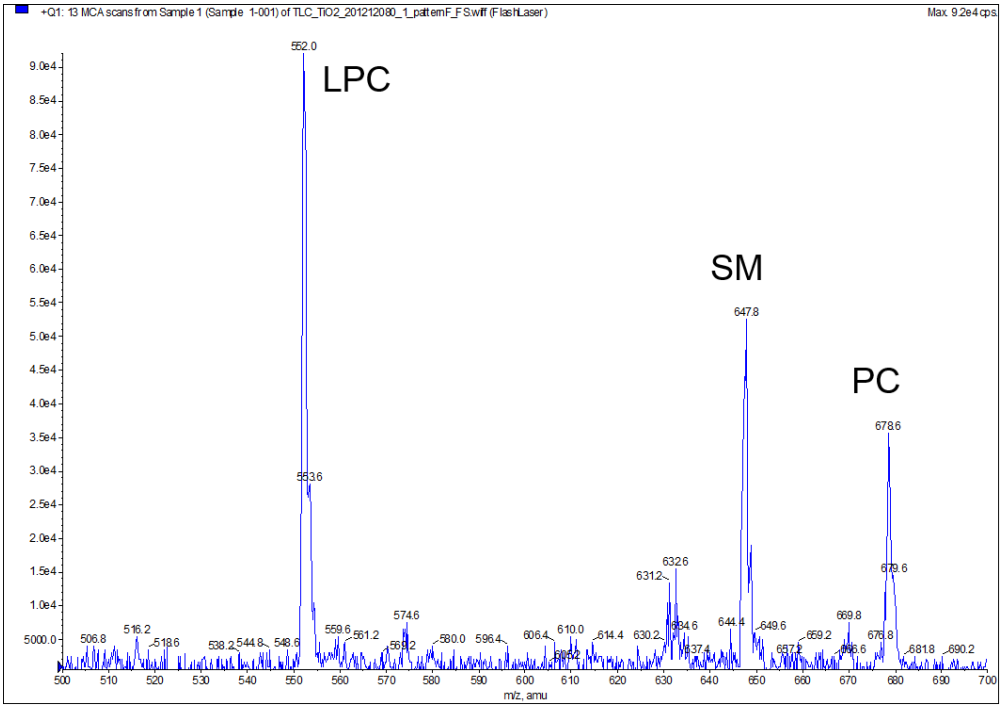

Position F (also shown in **figure 4.14** in the main text)

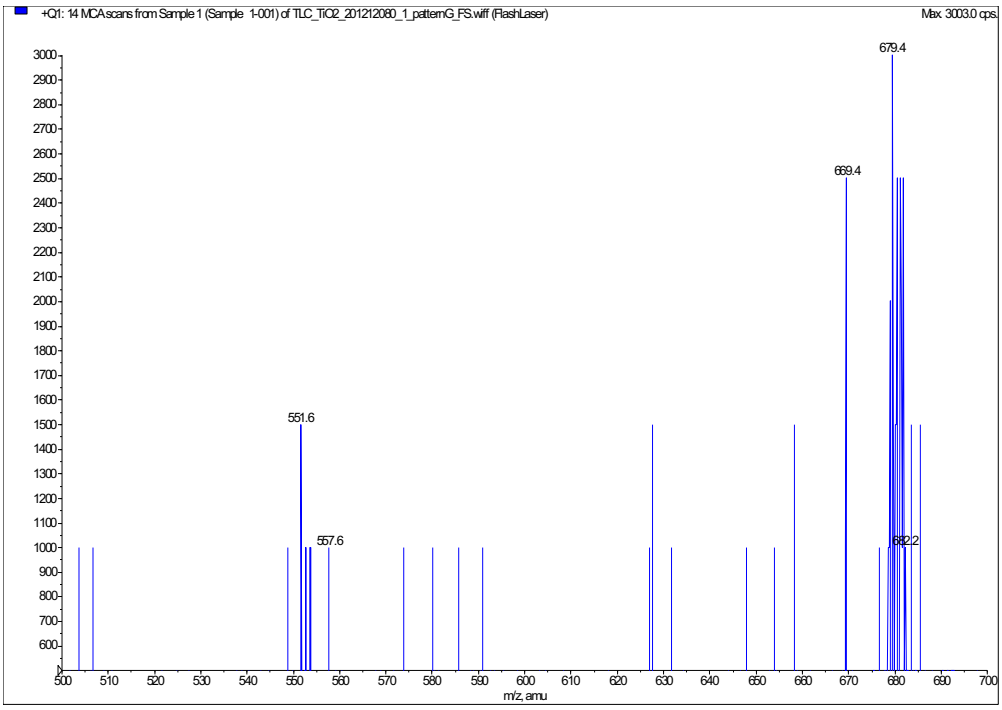

Position G

A-3 SPR sensorgrams for interactions of 3 serum proteins with gold nanoparticles

Further from ***section 5.3.2***

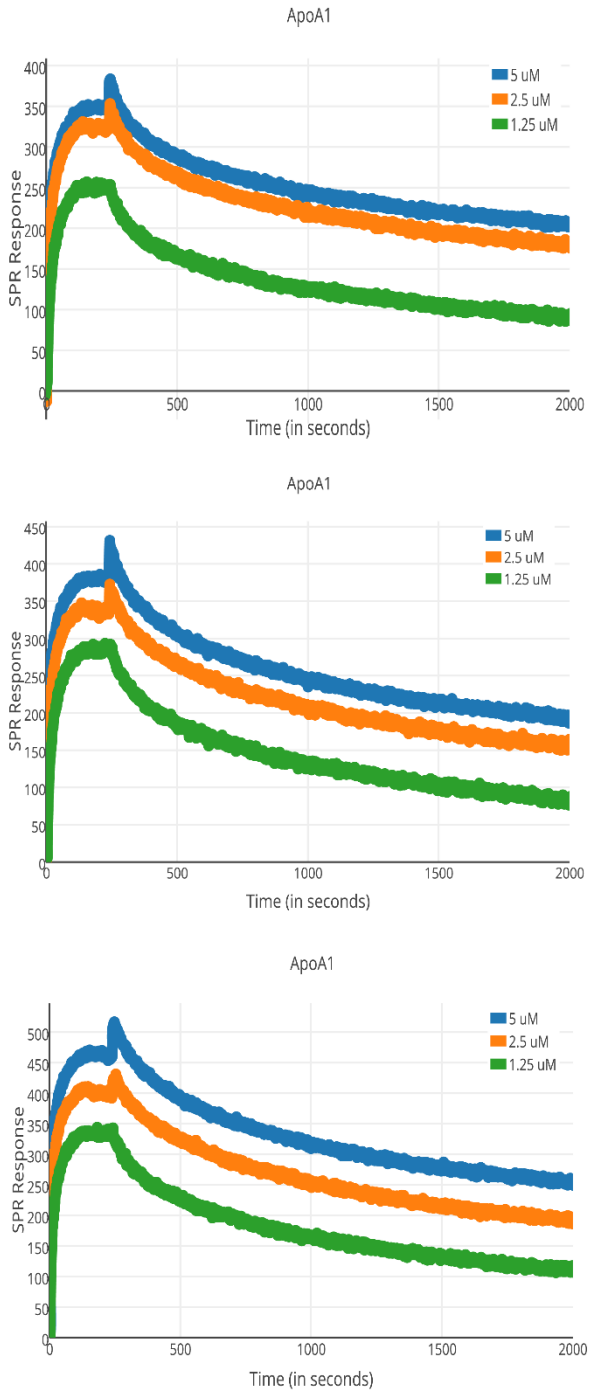

Figure 1: SPR Sensorgram for ApoA1 interacting with AuNPs. Different colours represent different concentrations. Concentrations shown in legend. 3 sets of data have been shown.

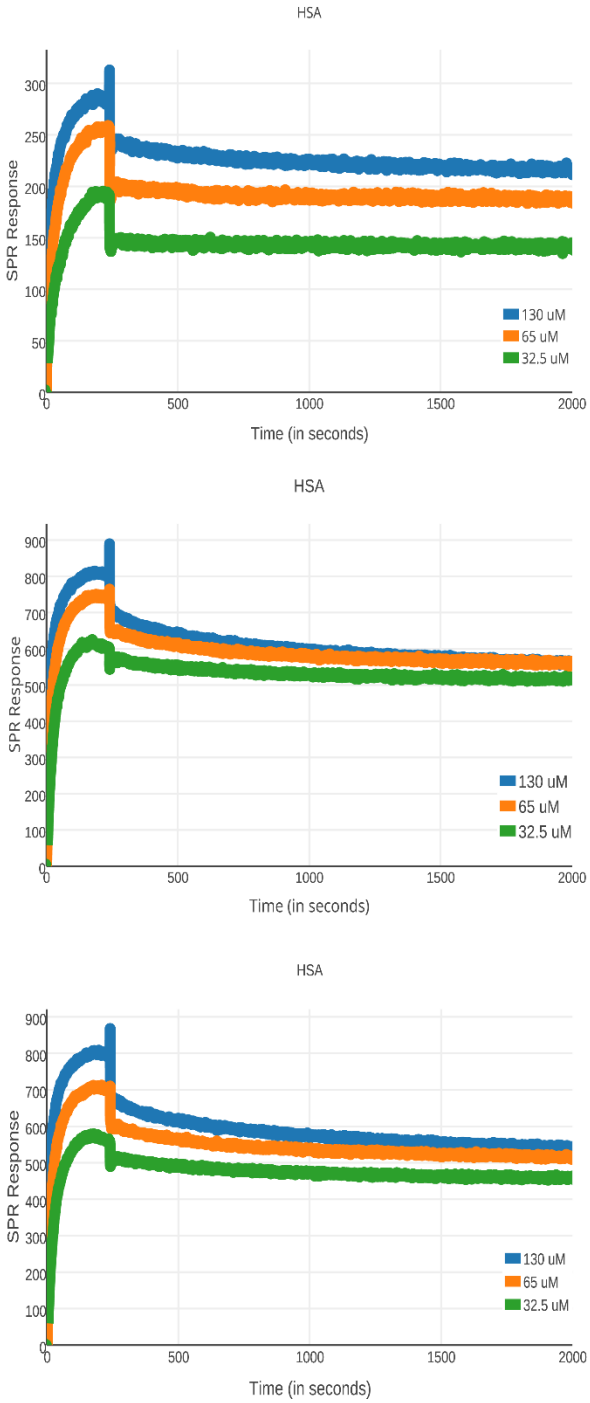

Figure 2: SPR Sensorgram for HSA interacting with AuNPs. Different colours represent different concentrations. Concentrations shown in legend. 3 sets of data have been shown.

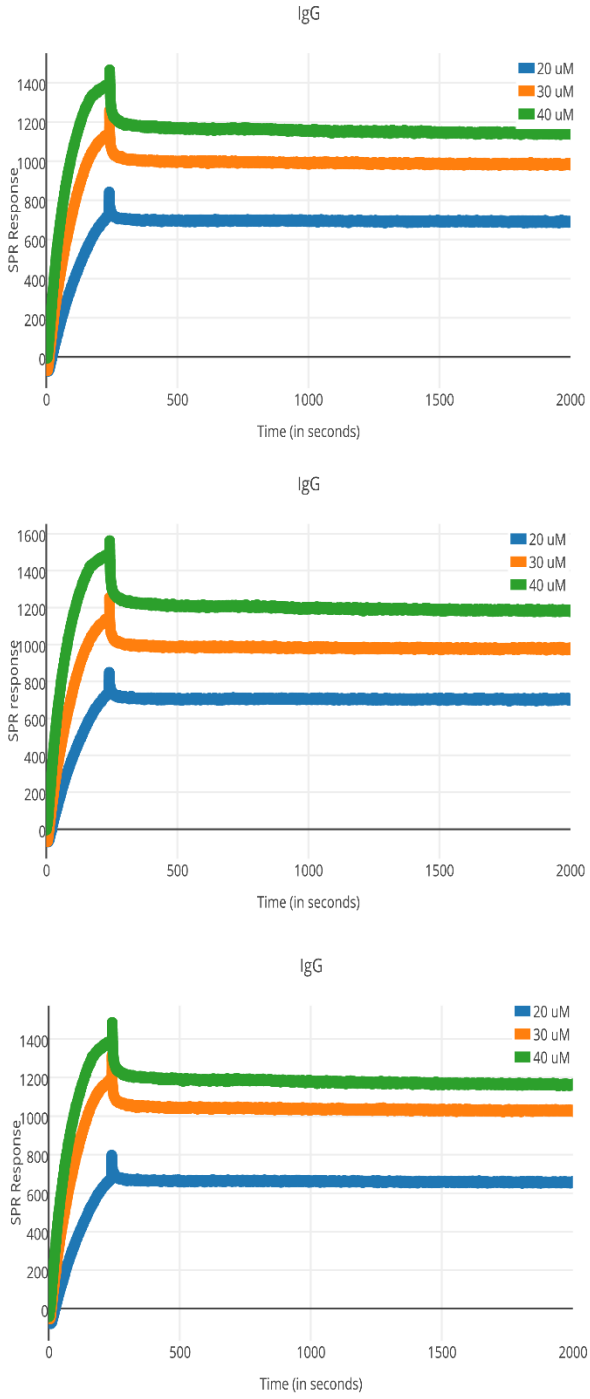

Figure 3: SPR Sensorgram for IgG interacting with AuNPs. Different colours represent different concentrations. Concentrations shown in legend. 3 sets of data have been shown.

A-4 SPR sensorgrams for interactions of PEG with chemically active chip surface

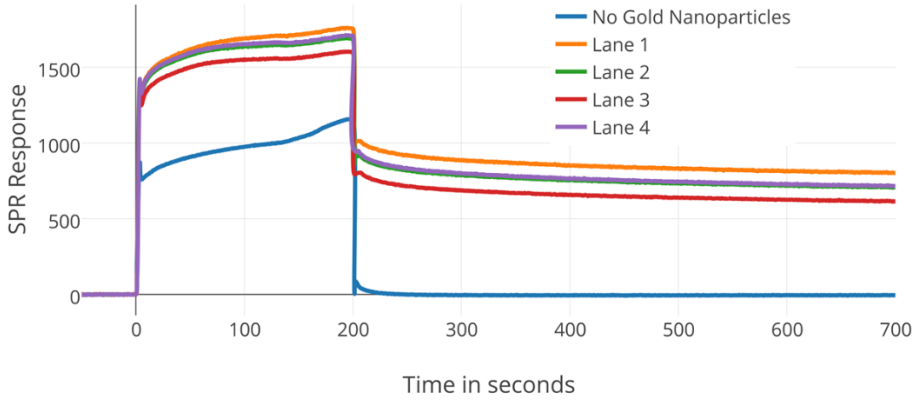

Figure 4: Control studies to show no interaction of PEG with the chemically active linker surface. Lanes 1, 2, 3 and 4 have gold nanoparticles and PEG is seen to adsorb onto the captured nanoparticles. When there are no captured gold nanoparticles, PEG doesn't adsorb at all onto the chip surface.